

Modelling of Diffusion-weighted MRI

Signals in Non-neural Tissue

Sisi Liang

A thesis submitted in fulfilment of
the requirements for the degree of
Doctor of Philosophy



College of Engineering and Science

Victoria University

Melbourne, Australia

January 3, 2017

Abstract

Purpose

The general aim of clinical diffusion-weighted MRI (DWI) is the inference of tissue structure properties, particularly pathology, from measurements of diffusion attenuation under conditions of varying diffusion times and b -values. Models of water diffusion in tissue have been proposed to serve this purpose. Diffusion models can be broadly split into two types, phenomenological and structural. Phenomenological models aim to provide reliable mathematical descriptions of DWI signals, but biophysical interpretation of their model parameters is limited. The recent trend is towards compartment models that are based on assumptions about tissue geometry. Compartment models have proven successful in brain imaging, where they predict the diffusion signal more accurately and provide estimates of specific neural tissue features, such as fiber orientation distribution and axon diameter. However, compartment models are generally lacking for non-neural tissue. This thesis investigates compartment models of diffusion in four types of non-neural tissue (prostate, breast, spheroids and lymph nodes).

Materials and Methods

Tissue samples were acquired after institutional ethics review committee approval and informed written consent from patients were obtained. Seven whole human prostates were imaged on 9.4T Bruker MRI system in formalin fixed condition. Three samples of human breast tissue specimens, two samples of human lymph nodes, and one sample of dog lymph nodes were collected, fixed in formalin, and imaged on 9.4T Bruker MRI system. Six spheroids were cultured from DLD-1 (human colorectal carcinoma) cell line using the liquid overlay method, fixed with 4% paraformaldehyde, and imaged in a 14T Bruker MRI scanner.

All diffusion-weighted measurements were performed using a pulsed gradient spin echo sequence. Eleven models, including different combinations of isotropic, anisotropic and

restricted components, were tested. Each model was fitted to the data using the Levenberg-Marquardt minimization algorithm in the open source Camino toolkit. Models were ranked using the Akaike information criterion (AIC), which compared models in terms of theoretical information.

Results

For DWI measurements acquired with multiple b values and multiple Δ/δ values in prostate tissue, compartment models incorporating both anisotropic and restricted components provided more information-rich descriptions of signals than single-component models and multi-component models that did not account for restricted diffusion.

One of the multi-component models, comprising both anisotropic and restricted components was then used for synthesizing DTI data in prostate tissue. Measured mean diffusivity (MD) and fractional anisotropy (FA) were calculated from DTI measurements. Predicted MD and FA were calculated from synthesized DTI data. The results demonstrated diffusion time dependence of MD and FA, which was accurately predicted by that multi-component restricted and anisotropic model.

The overall AIC ranking of eleven models in breast tissue (including gland lobule, interlobular stroma and fat) and lymph nodes showed that multi-component restricted models had higher information than single-component models and multi-component unrestricted models. In glandular breast tissue, multi-component models that accounted for both anisotropy and diffusion restriction ranked highest. The AIC ranking of three isotropic models in spheroids showed that the model including restricted component had the highest information.

Conclusion

Multi-component models incorporating a restricted component and an isotropic/anisotropic Gaussian component provided more information-rich descriptions of multi- Δ , multi- b DWI measurements in four types of non-neural tissue than single-component (ADC) model and multi-component unrestricted models. ADC model to

date has been the most widely used analysis for cancer assessment in clinical DWI studies. The low AIC ranking of ADC model suggested that the implementation of more sophisticated compartment models might improve performance in detection of non-neural tumour significantly.

Declaration

I, Sisi Liang, declare that the PhD Thesis entitled “Modelling of Diffusion-weighted MRI Signals in Non-neural Tissue” is no more than 100,000 words in length including quotes and exclusive of tables, figures, appendices, bibliography, references and footnotes. This thesis contains no material that has been submitted previously, in whole or in part, for the award of any other academic degree or diploma. Except where otherwise indicated, this thesis is my own work.

Signature

A black rectangular box redacting the signature of the author.

Date: January 3, 2017

Acknowledgements

First, I would like to express my sincere gratitude to my primary supervisor, Professor Peng Shi for giving me this opportunity to do my research project at Victoria University. He offered me the freedom to explore a new research area, think independently and seek solutions. Thanks for his guidance, advice, support and encouragement throughout my PhD study.

I would like to express my special appreciation and thanks to my associate supervisor, Dr Roger Bourne from University of Sydney for his generous guidance and fruitful discussion. I would also like to thank him for providing my research data and valuable feedback on my research results. I am thankful to my main collaborator, Dr Eleftheria Panagiotaki from UCL for teaching me how to run model fitting in Camino and sharing her expertise.

Many more collaborators helped me complete this study. I would like to thank Dr Paul Sved and Dr Geoffrey Watson from Royal Prince Alfred Hospital for providing prostate samples and prostate histology information respectively, and Dr Laurence Gluch from the Strathfield Breast Centre for providing breast samples. I am also thankful to Dr Andre Bongers from University of New South Wales for performing *ex vivo* imaging on 9.4T MRI system, and Dr Timothy Stait-Gardner from Western Sydney University for performing *ex vivo* imaging on 14T MRI system.

I would like to thank my PhD colleagues, Madiha Yunus for culturing spheroids and sharing her knowledge on cultured cells, Ned Charles for teaching me how to use high performance computing system, Aritrick Chatterjee for processing prostate samples, Narina Norddin for processing breast samples, and Mariaulpa Sahalan for processing lymph node samples. Thanks for all their support and advice.

Finally, I would like to express my deepest gratitude to my loving parents for allowing me to pursue my dream, believing in me, and encouraging me. Thanks for their endless love and support.

List of Publications and Awards

[1] Liang S, Panagiotaki E, Bongers A, Shi P, Sved P, Watson G, Bourne R. Information based ranking of ten compartment models of diffusion weighted signal attenuation in fixed prostate tissue. *NMR in Biomedicine* 2016;29(5):660-671.

[2] Bourne R, Liang S, Panagiotaki E, Bongers A, Sved P, Watson G. Measurement and modeling of diffusion time dependence of apparent diffusion coefficient and fractional anisotropy in prostate tissue ex vivo. It has been submitted to *Magnetic Resonance in Medicine*.

[3] Liang S, Norddin N, Panagiotaki E, Bongers A, Shi P, Gluch L, Bourne R. Comparison of multi-component restricted and anisotropic models of diffusion in glandular breast tissue, 24th Annual Meeting of International Society for magnetic resonance in medicine, Singapore. 2016. (Oral presentation)

[4] Liang S, Yunus M, Panagiotaki E, Kim B, Stait-Gardner T, Zubkov M, Hawkett B, Price W, Power C, Bourne R. Modeling of diffusion in cultured epithelial cell spheroids, 24th Annual Meeting of International Society for magnetic resonance in medicine, Singapore. 2016. (Poster presentation)

[5] Liang S, Panagiotaki E, Shi P, Bourne R. Comparison of seven compartment models of diffusion in prostate tissue, 23rd Annual Meeting of International Society for magnetic resonance in medicine, Toronto, Canada. 2015. (Poster presentation)

[6] The ISMRM Magna Cum Laude Merit Award for the work entitled 'Comparison of multi-component restricted and anisotropic models of diffusion in glandular breast tissue', 24th Annual Meeting of International Society for magnetic resonance in medicine, Singapore. 2016.

[7] The poster presentation award for the work entitled 'Modeling of diffusion in cultured epithelial cell spheroids', 24th Annual Meeting of International Society for magnetic resonance in medicine, Singapore. 2016.

[8] Victoria University Postgraduate Research Scholarship, Victoria University, Australia (2012-2016)

[9] Staff and HDR Student Research Conference Fund, Victoria University, Australia, 2015.

[10] Secomb Conference and Travel Fund, Victoria University, Australia, 2015.

Table of Contents

Abstract	i
Declaration	iv
Acknowledgements	v
List of Publications and Awards	vi
Table of Contents	viii
List of Figures	xii
List of Tables	xv
List of Abbreviations	xvi
Chapter 1 Introduction	1
1.1. Background and Motivation	1
1.2. Problem Statement	2
1.3. Research Aims	3
1.4. Thesis Structure	3
Chapter 2 Literature Review	5
2.1. Diffusion-weighted MRI (DWI)	5
2.1.1. Basics of Diffusion-weighted MRI	5
2.1.2. Pulsed Gradient Spin Echo	5
2.2. Diffusion in Biological Systems	8
2.2.1. Restricted Diffusion	9
2.2.2. Hindered Diffusion	12
2.2.3. Anisotropic Diffusion	13
2.3. Models of DWI Signal Attenuation	15
2.3.1. Phenomenological Models	15

2.3.2.	Compartment Models.....	18
2.4.	Prostate Tissue	23
2.4.1.	Anatomy and Histology.....	23
2.4.2.	Models of DWI in Prostate Tissue.....	26
2.5.	Breast Tissue.....	29
2.5.1.	Anatomy and Histology.....	29
2.5.2.	Models of DWI in Breast Tissue	31
2.6.	Cultured Cell Constructs	34
2.6.1.	3D culture system	34
2.6.2.	Models of DWI in Cell Constructs	35
2.7.	Lymph Node Tissue.....	36
2.7.1.	Anatomy and Histology.....	36
2.7.2.	Models of DWI in Lymph Node	39
2.8.	Summary.....	41
Chapter 3 Information Based Ranking of Models of Diffusion in Prostate Tissue.....		42
3.1.	Introduction.....	42
3.2.	Methods	43
3.2.1.	Tissue Handling and Histopathology.....	43
3.2.2.	MRI Acquisition.....	43
3.2.3.	Model Description	45
3.2.4.	Model Fitting Method.....	46
3.2.5.	Information Based Model Ranking	47
3.3.	Results	48
3.3.1.	AIC-based Model Ranking.....	49
3.3.2.	Synthesis and Fitting.....	53
3.3.3.	Parametric Maps.....	55
3.3.4.	Anisotropy.....	58
3.4.	Discussion	58
3.4.1.	Limitation.....	62
3.5.	Conclusions.....	63

Chapter 4 Predicting the Impact of Diffusion Time on Mean Diffusivity and Fractional Anisotropy in Fixed Prostate Tissue	64
4.1. Introduction.....	64
4.2. Methods	65
4.2.1. Tissue Handling.....	65
4.2.2. MRI Acquisition.....	65
4.2.3. Model Description	68
4.2.4. Model Fitting.....	68
4.3. Results	69
4.4. Discussion	77
4.4.1. Effect of diffusion time and noise on MD	78
4.4.2. Effect of diffusion time and noise on FA.....	79
4.4.3. Clinical insights.....	80
4.4.4. Limitations	81
4.5. Conclusions.....	82
Chapter 5 Applications to Other Tissues	83
5.1. Introduction.....	83
5.2. Methods	84
5.2.1. Tissue Handling and Histopathology.....	84
5.2.2. MRI Acquisition.....	84
5.2.3. Model Description	86
5.2.4. Model Fitting and Ranking	87
5.2.5. ROI selection	87
5.3. Results	88
5.3.1. Breast Tissue	88
5.3.2. Epithelial Cell Spheroids.....	94
5.3.3. Lymph Node Tissue	96
5.4. Discussion	97
5.4.1. Breast Tissue	98
5.4.2. Epithelial Cell Spheroids.....	99
5.4.3. Lymph Node Tissue	100

5.4.4. Limitations	101
5.5. Conclusions.....	102
Chapter 6 Conclusions	103
6.1. Non-neural Tissue.....	104
6.2. Advances in Knowledge.....	106
6.3. Future Work	108
References	110
Appendices.....	136
Appendix A Supporting Information for Chapter 3.....	136
Appendix B Supporting Information for Chapter 4.....	141
Appendix C Supporting Information for Chapter 5.....	142

List of Figures

Figure 2.1: A schematic representation of a PGSE sequence.....	6
Figure 2.2: Schematic representation of the phase evolution of the static and moving spins during the PGSE sequence.	7
Figure 2.3 A schematic diagram comparing free diffusion with restricted diffusion in a sphere of radius a at three different timescales.	10
Figure 2.4 The mean displacement vs the square root of diffusion time.....	11
Figure 2.5 Restricted and hindered diffusion in white matter.	13
Figure 2.6 Schematic diagrams for water motion in free water and two different mediums.....	14
Figure 2.7 The anatomy of the prostate.....	23
Figure 2.8 Coronal section of the prostate.....	24
Figure 2.9 Histology of the normal prostate gland.....	25
Figure 2.10 Morphologic spectrum of Gleason patterns.	25
Figure 2.11 Components of the breast.....	30
Figure 2.12 Fully developed breast lobular unit.....	31
Figure 2.13 Microenvironments inside a spheroid.....	35
Figure 2.14 Schematic diagram of a female being showing major locations of lymph nodes, thoracic duct, thymus, spleen and other lymph vessels.....	37
Figure 2.15 Structure of a lymph node.....	38
Figure 2.16 Histology of normal and malignant lymph nodes.....	39
Figure 3.1 Variation in AIC-based model rankings for four prostates.	50

Figure 3.2 Rank variations of individual models in four prostates.	51
Figure 3.3 Box and whisker plots of log(AIC).	52
Figure 3.4 Representative model fit data.	54
Figure 3.5 Zeppelin-sphere model parameter maps.	56
Figure 3.6 Two-way parameter histograms for the Zeppelin-sphere model.	57
Figure 3.7 MD and FA maps from Tensor-sphere, Zeppelin-sphere, and DTI models for Prostate 3.	58
Figure 4.1 Calculation of FA and MD.	69
Figure 4.2 Effect of diffusion time on mean voxel MD and FA at $b = 800, 1600,$ and 3000 s/mm^2	70
Figure 4.3 Scatter plots of measured MD and FA versus MD and FA predicted by the zeppelin-sphere model for $b = 800 \text{ s/mm}^2$	71
Figure 4.4 Zeppelin-sphere model parameter maps.	75
Figure 4.5 The fit of Zeppelin-sphere model to representative voxels from each prostate.	76
Figure 4.6 Scatter plots of measured FA versus Zeppelin FA at $b = 800 \text{ s/mm}^2$	77
Figure 5.1 Variation of model rankings in three breast samples.	89
Figure 5.2 Variation in rankings of individual models in three breasts.	90
Figure 5.3 Ball-sphere model parameter maps.	91
Figure 5.4 Variation of model rankings in gland ROIs.	92
Figure 5.5 Fits of eleven models.	93
Figure 5.6 A reference ($b = 0$) image of spheroids showing 24 selected voxels marked with *. Scale bar = $500 \mu\text{m}$	94

Figure 5.7 Variation of model rankings in spheroids.....	95
Figure 5.8 Variation of model rankings in lymph nodes.....	96
Figure A.1 Tensor-sphere model parameter maps.	138
Figure A.2 Ball-stick-sphere model parameter maps.	139
Figure A.3 One-way parameter histograms fro Zeppelin-sphere model.....	140
Figure B.1 Scatter plots of measured MD and FA versus MD and FA predicted by the zeppelin-sphere model for $b = 1600 \text{ s/mm}^2$	141
Figure C.1 Zeppelin-sphere model parameter maps.....	142

List of Tables

Table 2.1 Candidate compartment models for non-neural tissue	22
Table 3.1 DWI acquisition parameters	45
Table 3.2 Fitted models.....	46
Table 4.1 6-direction DTI acquisition parameters	66
Table 4.2 3-direction DWI acquisition parameters	67
Table 4.3 Correlation of measured MD and predicted MD ^a	72
Table 4.4 Correlation of measured FA and predicted FA ^a	74
Table 5.1 DWI acquisition parameters used for imaging breast tissue	85
Table 5.2 DWI acquisition parameters used for imaging spheroids and lymph nodes.....	86
Table 5.3 Sphere radius estimates from four models in breast tissue ^a	94
Table 5.4 Mean and standard deviation of Ball-sphere parameters in 24 voxels of spheroids.....	95
Table A.1 P-values from Mann-Whitney U-test.	136

List of Abbreviations

ADC	Apparent Diffusion Coefficient
AIC	Akaike Information Criterion
BI-RADS	Breast Imaging Reporting and Data System
CT	Computerized Tomography
CZ	Central Zone
DCE	Dynamic Contrast Enhanced
DT	Diffusion Tensor
DTI	Diffusion Tensor Imaging
DWI	Diffusion-weighted MRI
FA	Fractional Anisotropy
IVIM	Intravoxel Incoherent Motion
MD	Mean Diffusivity
mpMRI	Multiparametric MRI
PI-RADS	Prostate Imaging Reporting and Data System
PBS	Phosphate-Buffered Saline
PGSE	Pulsed Gradient Spin Echo
PZ	Peripheral Zone
RF	Radiofrequency
SNR	Signal-to-Noise Ratio
T2W	T ₂ weighted
TE	Echo Time
TZ	Transition Zone
VERDICT	Vascular, Extracellular and Restricted Diffusion for Cytometry in Tumours

Chapter 1 Introduction

1.1. Background and Motivation

MRI is an important tool in oncological assessment because of its excellent soft tissue contrast. Among MRI methods, diffusion-weighted MRI (DWI) is increasingly used as an imaging biomarker for the detection and characterization of cancer. For example, the most established clinical application of DWI is the high-sensitivity detection of cerebral ischemia [1-3]. In other organs such as prostate and breast, DWI is also found useful for tumour detection [4-7]. DWI measures water molecular motion within tissue due to thermal motion. Depending on protocol, DWI may also be sensitive to blood flow. Water motion is influenced by the tissue microstructure. Hence DWI has a unique ability to probe the underlying tissue structure. The general aim of clinical DWI is the inference of tissue structure properties, particularly pathology, from measurements of the attenuation of DWI signal under conditions of varying diffusion times and diffusion-weightings. Models of water diffusion in tissue have been proposed to serve this purpose. Diffusion models can be broadly split into two types, phenomenological and structural. Phenomenological models aim to provide a reliable mathematical description of DWI signals. Structural models are based on assumptions about tissue structure and are composed of one or multiple structural compartments. The most commonly used phenomenological model in both clinical and research environments is the apparent diffusion coefficient (ADC) model. The ADC model assumes a Gaussian water displacement probability that is manifested as monoexponential diffusion-weighted signal decay. The ADC model has proven extremely powerful in the detection of a variety of pathologies [8,9]. However, many tissues are known to exhibit non-monoexponential signal decay, suggesting the need for a better understanding to elucidate biophysical properties of water diffusion within the tissue. Other phenomenological models including biexponential [10-12], kurtosis [13,14] and stretched models [15] have been used to characterize this non-monoexponential behavior. The diffusion tensor model, which is equivalent to a three-dimensional ADC, has been introduced to accounts for diffusion anisotropy [16]. Although these advanced

phenomenological models provide a better fit to the data, biophysical interpretation of their model parameters is limited. The recent trend is towards compartment models, which aim to quantitatively relate microstructure features to DWI signals. Most studies have designed compartment models to estimate specific features of neural tissue such as axon radius in white matter [17-21] or neurite orientation distribution [22]. White matter compartment models have been compared in terms of theoretical information [23-25]. The best model for a given set of measurement data is the one that extracts the most information from the data. The assumption behind this comparison is that the model with higher information is more close to the unknown true system and thus has a better prediction of tissue microstructure. The true system refers to the underlying biophysical mechanism that produces diffusion contrast in tissue.

1.2. Problem Statement

The problem that motivates this work is that of using DWI measurements to obtain specific microstructure features, ideally diagnostic features, for non-neural tissue. There are three different, but not independent steps towards this goal. The first step is to define an imaging protocol that can acquire appropriate tissue structure information. The second step is to construct models that can relate specific tissue features to the DWI signal. The third step is to extract as much information as possible from the acquired data by selecting the model that contains highest information. This study focused on the second and the third steps. Compartment models are good candidates for this purpose. However, compartment models and rigorous comparison of compartment models are generally lacking for non-neural tissue. Most previous studies applied phenomenological models to non-neural tissues including prostate [10,26-30], breast [12,31-33] and lymph node [34-36]. Phenomenological models have been compared in terms of either cancer detection performance [30,37,38] or theoretical information [39,40].

A three-compartment model named VERDICT (Vascular, Extracellular, and Restricted Diffusion for Cytometry in Tumours), based on intracellular, vascular, extracellular-extravascular compartments, has recently been used to extract histological features of two colorectal cancer cell lines including cell size, cell density, and vascular volume fraction [41]. The VERDICT model successfully distinguished two cell lines while the

ADC and biexponential models failed to detect the difference. A subsequent study on the prostate in vivo demonstrated that the VERDICT model differentiated between benign and cancerous tissue more reliably than ADC and biexponential models [42]. Both studies used an extended imaging protocol (relative to standard clinical imaging protocols) to determine the best form of the VERDICT model. A recent study reported a clinically feasible protocol for prostate microstructure characterization with the VERDICT model [43]. These promising results highlight the advantages of compartment models. The development of more advanced models and DWI acquisitions may lead to new cancer imaging methods that improve performance in detection of non-neural tumor significantly.

1.3. Research Aims

The aims of this study are as follows:

1. Investigate theoretical information of single- and multi-compartment models of diffusion in fixed prostate tissue and identify which model extracts the most information from the measurement data. Eleven models, including different combinations of isotropic, anisotropic and restricted components, are tested.
2. Use the best model identified in Aim 1 to predict the impact of diffusion time on mean diffusivity (MD) and fractional anisotropy (FA) and compare this predicted impact with the impact assessed from the measurement data. This experiment provides a new way to use and validate compartment models.
3. Investigate compartment models of diffusion in breast tissue, lymph node tissue, and cultured cell constructs.

1.4. Thesis Structure

Chapter 2 presents a review of DWI, biophysics of water diffusion in tissue, tissue modeling, structural information on prostate tissue, breast tissue, lymph node tissue and spheroids, and modeling techniques currently used for these types of tissue.

Motivated by a successful application of the three-component VERDICT model in prostate tissue in vivo [42], Chapter 3 investigates the non-perfusion components of the VERDICT model in prostate tissue ex vivo by comparing theoretical information of eleven compartment models.

Chapter 4 evaluates the impact of diffusion time on MD and FA generated from both the measurement data and the synthesized data predicted by the best model identified in Chapter 3.

Chapter 5 applies compartment models to breast tissue, lymph node tissue, and spheroids.

Chapter 6 concludes the research and gives suggestions for future work.

Chapter 2 Literature Review

2.1. Diffusion-weighted MRI (DWI)

2.1.1. Basics of Diffusion-weighted MRI

DWI measures random thermal motion of water molecules within tissue. In the absence of any obstacles, water molecules are allowed to move freely. The motion of freely diffusing water molecules, which is referred to as either free diffusion or self-diffusion, follows a Gaussian distribution. The average squared displacement ($\langle r^2 \rangle$) of free water molecules over the given time in three dimensions is

$$\langle r^2 \rangle = 6Dt \quad [2.1]$$

where t is the time interval over which water molecules are allowed to diffuse, and D is the diffusion coefficient that is temperature dependent. For free water at body temperature (37 °C), the diffusion coefficient is about 3×10^{-3} mm²/s. The typical time t used for clinical DWI is around 40 - 80 ms, corresponding to mean displacements on the order of 10 μm in free water. These resultant mean displacements are on the order of the cell size. Hence water diffusion in tissue is sensitive to the cellular environment. In biological tissue, water molecules do not move freely but instead interact with intracellular elements, cell membranes, and macromolecules. In such an environment, water motion no longer follows a Gaussian distribution and the relationship stated by Eq. 2.1 does not hold. The interactions with various cellular elements mean that measurement of water molecular motion in tissue reveals information about the tissue microstructure.

2.1.2. Pulsed Gradient Spin Echo

In 1965 Stejskal and Tanner introduced the pulsed gradient spin echo (PGSE) pulse sequence [44], which is the most widely used sequence for DWI. The PGSE sequence (Figure 2.1) is composed of 90° and 180° radiofrequency (RF) pulses and a pair of diffusion-sensitizing gradients placed on either side of 180° RF pulse. Each diffusion gradient has duration δ and magnitude G . The RF pulse has a short duration, oscillates

at radiofrequencies, and is primarily used for excitation and refocusing. The temporal separation of the diffusion gradient pulses is referred to as Δ . The time between the start of RF pulse and the maximum in the MRI signal is called TE (echo time).

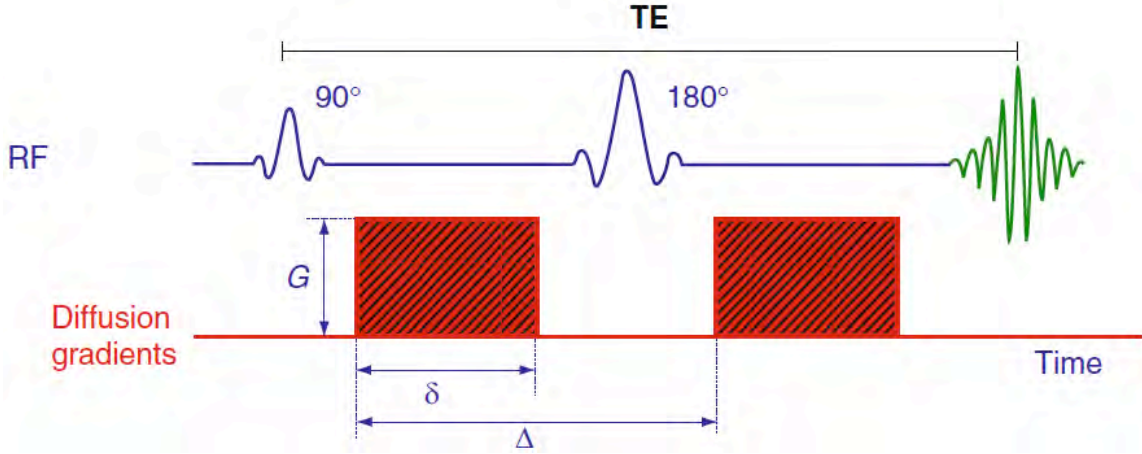


Figure 2.1: A schematic representation of a PGSE sequence

Two diffusion-sensitizing gradients are added to a spin echo sequence. δ denotes the gradient pulse duration, Δ the interval between two gradients, and G the amplitude of the gradient. (Reproduced from [45] with permission from Springer Berlin Heidelberg, Germany)

The applied diffusion-sensitizing gradient introduces a phase shift of a spin. Figure 2.2 shows the phase evolution of the static and moving (translating) spins during the PGSE sequence. After 90° RF excitation, a firstly applied gradient pulse offsets a position-dependent phase of a spin by

$$\phi_1 = \gamma \int_0^{\delta} G(t)x(t)dt \quad [2.2]$$

where γ is the gyromagnetic ratio, $G(t)$ is the magnetic field gradient and $x(t)$ is the position of the spin. Next, an 180° RF pulse is applied that has the effect of reversing the sign of the accumulated phase shift, a second gradient pulse that is identical to the first gradient pulse produces another position-dependent phase change,

$$\phi_2 = \gamma \int_{\Delta}^{\Delta+\delta} G(t)x(t)dt \quad [2.3]$$

Therefore, the net phase shift is

$$\phi = \phi_2 - \phi_1 = \gamma \left(\int_0^\delta G(t)x(t)dt - \int_\Delta^{\Delta+\delta} G(t)x(t)dt \right) \quad [2.4]$$

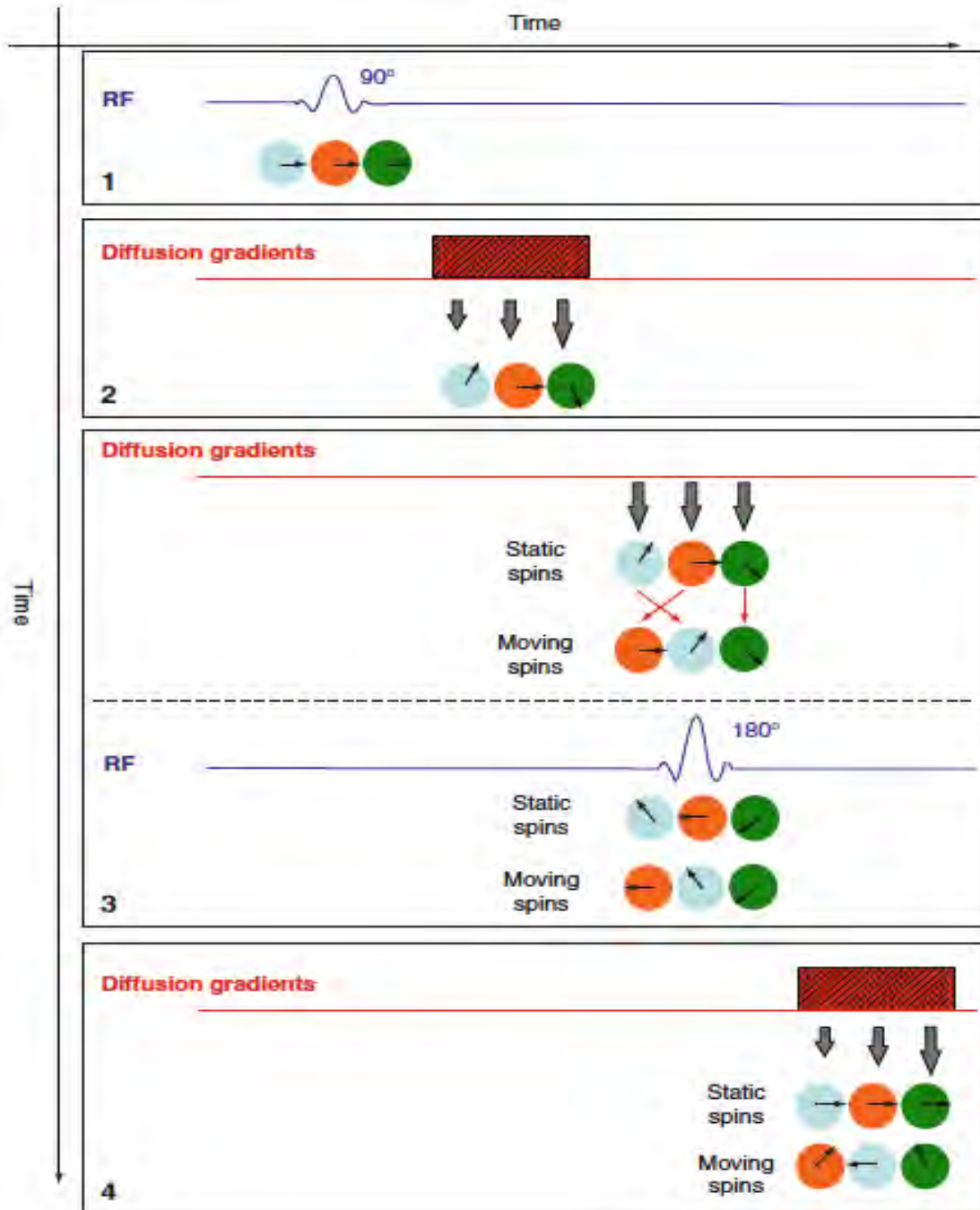


Figure 2.2: Schematic representation of the phase evolution of the static and moving spins during the PGSE sequence.

After 90° RF excitation, the first gradient pulse is applied causing a diphas in all the spins. A 180° RF pulse is then applied flipping the phase of all the spins 180°. Finally, the second gradient pulse which is the same as the first gradient is applied. After the second gradient, static spins remain in the same position and thus the net phase shift

is zero. On the other hand, the moving spins change their position (red arrows in 2.2.3), so they do not recover the phase. This phase incoherence causes attenuation of MRI signal. (Reproduced from [45] with permission from Springer Berlin Heidelberg, Germany)

In the case of static spins meaning that spins remain at the same position, the phase shifts accumulated during the application of both gradient pulses are the same, and thus the net phase shift is zero. In this situation, no attenuation of MRI signal (but rather phase change) would occur, as in the case of, for example, flow. Conversely the moving spins change their position so that the phase change accumulated during the second gradient pulse could not cancel the phase change experienced during the first gradient pulse. This incomplete cancellation yields a non-zero net phase shift. The phase incoherence within a voxel, which is the result of random motion of these spins, leads to attenuation of MRI signal at TE along the direction of the applied gradient pair. The MRI signal attenuation (S)

$$S = S_0 \exp(-bD) \quad [2.5]$$

where S_0 is the MRI signal attenuation in the absence of diffusion gradients, b is a measure of diffusion weighting, and D is the self-diffusion coefficient for free diffusion. In biological tissue where diffusion is generally not free, the measured D is smaller than the self-diffusion coefficient, namely ADC. The b -value for rectangular gradient pulses in the PGSE sequence is

$$b = \gamma^2 G^2 \delta^2 \left(\Delta - \frac{\delta}{3} \right) \quad [2.6]$$

According to Eq. [2.6], b is a function of δ , G , and Δ . In practice, different b -values are usually obtained by changing values of G with fixed values of δ and Δ . It is worth noting that Δ is an important parameter because it determines the scale on which water molecules interact with the tissue structure.

2.2. Diffusion in Biological Systems

Water diffusion in biological tissue is a complex process because water diffusion is affected by the packing geometry of the cells and cell membrane permeability that controls the water exchange across the membranes [46,47]. Three important types of

diffusion effects will be described in this section. They are restricted diffusion, hindered diffusion, and anisotropic diffusion.

2.2.1. Restricted Diffusion

Restricted diffusion refers to the trapping of water molecules inside a closed compartment. In biological tissue, cell membranes provide a physical boundary that prevents water molecules from moving freely. For the most permeable cell membrane, red blood cell, only one in ten thousand water molecules which are located closely to the cell membrane will cross the membrane and move into the extracellular space [48]. Thus water diffusion in an intracellular compartment is usually highly restricted. The distribution of restricted diffusion is a complicated function, which deviates from a Gaussian function and is influenced by many factors including the cell permeability, the size and shape of restricting geometry, and MRI experimental parameters [49]. The values of Δ (diffusion time) determine the extent to which water molecules interact with the tissue geometry. To illustrate this, consider a water molecule undergoing free diffusion and restricted diffusion in a closed spherical pore of radius a as shown in Figure 2.3. To characterize the effect of restricted diffusion, the dimensionless variable ξ is defined from Eq. 2.1 where δ is replaced by 1, t by Δ and r by a ,

$$\xi = D\Delta/a^2 \quad [2.7]$$

For a short diffusion time ($\xi \ll 1$), most water molecules do not diffuse far enough to feel the effects of the borders, and thus water molecular motion behaves as for free diffusion. As diffusion time increases ($\xi \approx 1$), a certain fraction of water molecules will interact with the boundary. The mean squared displacement along the z -axis in this situation does not continue to rise linearly with diffusion time. Thus the observed diffusion coefficient D (or ADC) appears to be Δ dependent. For a very long diffusion time ($\xi \gg 1$), all of water molecules feel the effect of restriction. The mean squared displacement becomes independent of Δ and depends only on a . Figure 2.4 shows the mean squared displacement of water molecules in free diffusion and restricted diffusion. In free diffusion, the mean squared displacement is proportional to the square root of diffusion time and is time dependent. In restricted diffusion, the mean squared displacement is sublinear in time and is limited by dimensions of the restricting compartment. The ADC for restricted water decreases with diffusion time over a finite range as a larger proportion of water molecules feel the boundary.

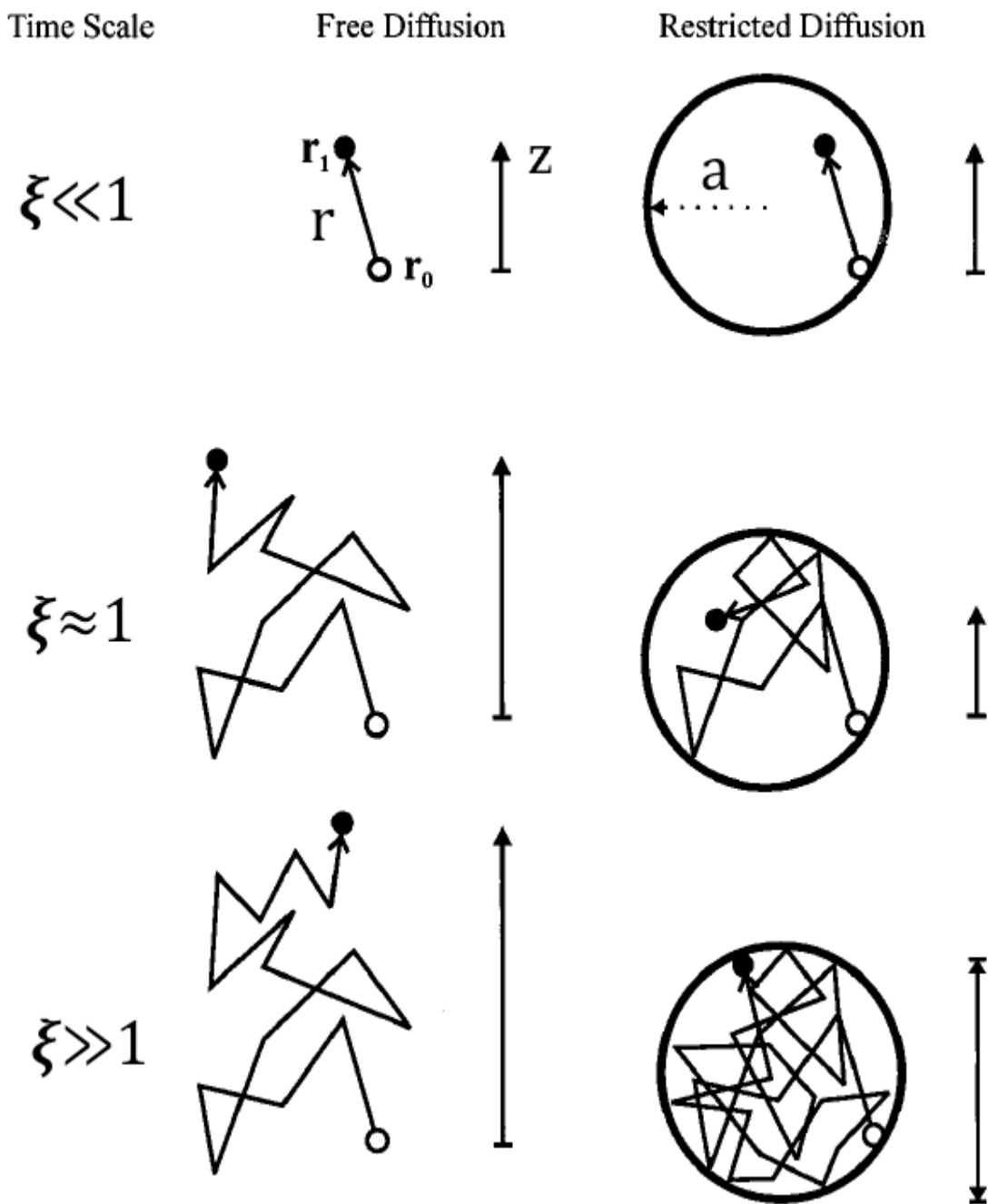


Figure 2.3 A schematic diagram comparing free diffusion with restricted diffusion in a sphere of radius a at three different timescales.

The displacement of a water molecule in the z direction is measured by observing its starting position r_0 (white circle) and then at r_1 (black circle) after Δ . r denotes the displacement between r_0 and r_1 . The vertical arrows represent the displacement, Z , in the vertical direction. Timescale variable ξ is defined in Eq. [2.7]. (Reproduced from [50] with permission from John Wiley and Sons, US)

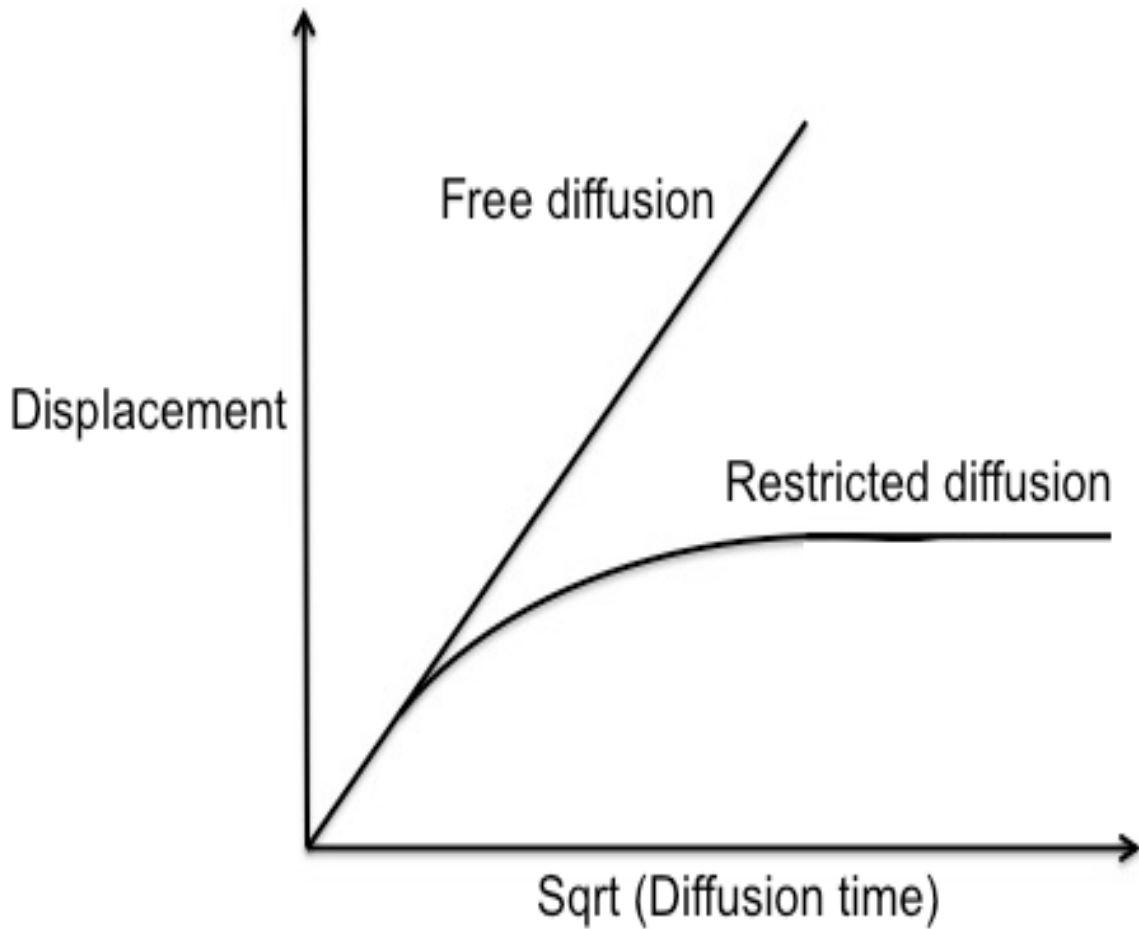


Figure 2.4 The mean displacement vs the square root of diffusion time.

In free diffusion, the mean squared displacement increases linearly with the square root of diffusion time with a slope that is self-diffusion coefficient D . In restricted diffusion, the mean squared displacement is limited by the compartment dimensions, leading to a sublinear time evolution of the mean squared displacement and a decreased ADC. The ADC of restricted water decreases with diffusion time over a finite range as a larger fraction of water molecules feel the boundary.

2.2.2. Hindered Diffusion

Hindered diffusion is a term used for describing the delay of the passage of water molecules because of the presence of obstacles compared with that in free water. To illustrate this idea, Figure 2.4 gives an example of restricted and hindered diffusion in brain white matter. Water diffusion inside axon (diameter, d) is restricted. To go from A to B, water molecules in the compact extracellular space have to travel around fibres rather than diffuse in a straight way. This hindrance effect results in a decrease in the diffusion distance covered over a given diffusion time and in the measured ADC. The degree of the hindrance is conventionally quantified using the tortuosity coefficient

$$\lambda = \sqrt{D/D^*} \quad [2.8]$$

where D is diffusion coefficient in the absence of obstacles, and D^* is the measured ADC and would not depend on diffusion time, unless diffusion time becomes very short, so that diffusion paths appear free [51]. In the hindered diffusion, water molecules are allowed to diffuse over a long distance, as opposed to restricted diffusion, so that the diffusion distance remains linear with the square root of diffusion time. Other factors, such as transient trapping of molecules and binding of molecules to the membrane surface, may also make contributions to the hindrance to the diffusion [52].

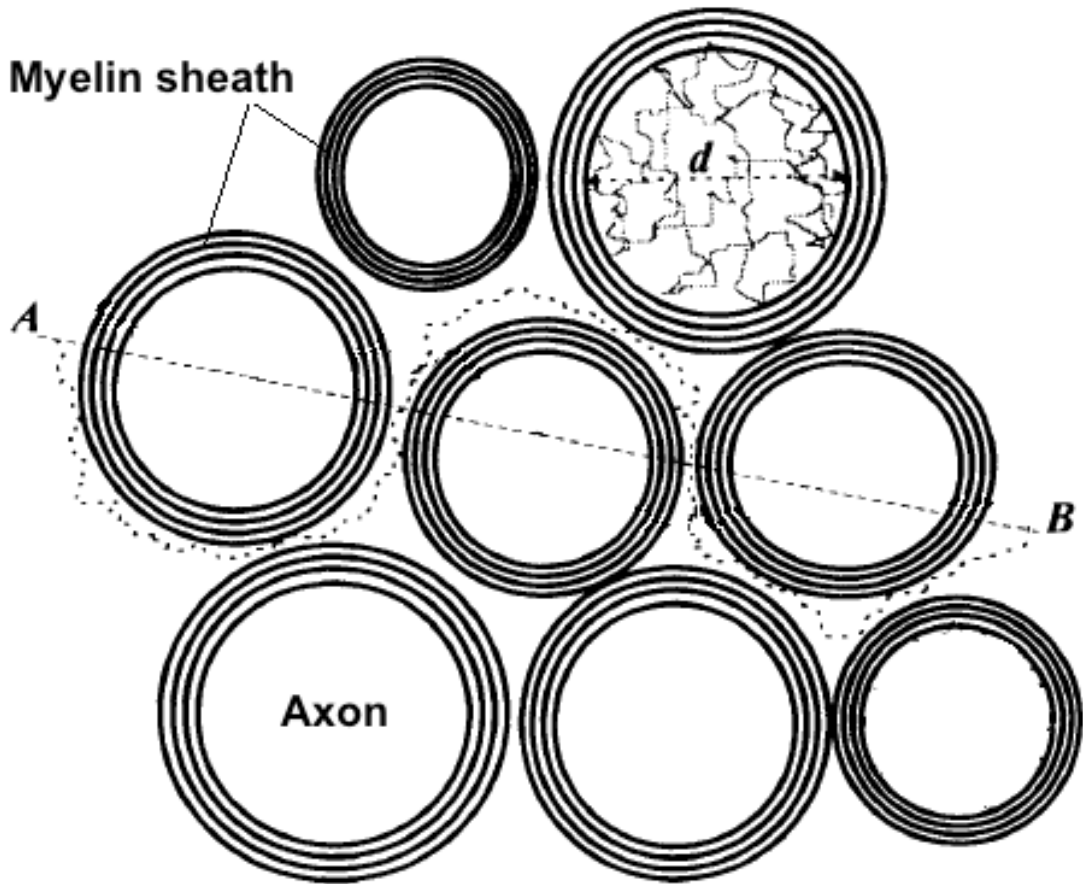


Figure 2.5 Restricted and hindered diffusion in white matter.

Water diffusion inside axons of dimension d is restricted. Fibres are arranged in a compact way. To go from A to B, water molecules in the extracellular space have to move around fibres instead of diffusing in a straight way. In this situation, water molecules need longer diffusion time to diffuse between two locations. (Reproduced from [49] with permission from John Wiley and Sons, US)

2.2.3. Anisotropic Diffusion

Anisotropic diffusion simply means that the diffusion coefficient is not the same in all directions. The diffusion anisotropy may be attributed to the medium geometry or the presence of obstacles. A three-dimensional Gaussian probability density function is used to characterize the displacement of molecules in anisotropic diffusion

$$P(r_0, r, t) = \frac{1}{(\sqrt{4\pi Dt})^3} \exp\left(-\frac{(r-r_0)^2}{4Dt}\right) \quad [2.9]$$

where D is the diffusion tensor (DT). More details on DT are discussed in section 2.3.1. Figure 2.5 shows isotropic and anisotropic diffusion in three different mediums. In free

water, the displacements of water molecules increase equally in all directions and water diffusion is isotropic (Figure 2.5A). Figure 2.5B shows water diffusion in an environment where spheres are randomly distributed. Water diffusion outside the spheres is isotropic because the boundaries of the spheres have no preferred direction and hinder water motion equally in all directions. Figure 2.5C shows water diffusion in a medium where cylinders are located parallel to each other. Water movement is hindered more in a direction perpendicular to the cylinder axis than along the cylinder axis. Thus water diffusion outside the cylinders is anisotropic. The neural tissue has been found to exhibit anisotropy. The diffusivity of water molecules along the white matter fibres is several-fold faster than that perpendicular to the fibres [53]. There is considerable interest in anisotropic diffusion properties of white matter, which are used for delineation of fibre tracts [54]. Diffusion anisotropy is also present in non-neural tissue including prostate [55,56], kidney [57] and cardiac muscle [58]. It is important to point out that diffusion can be both anisotropic and restricted (e.g., white matter fibres [53]) or both anisotropic and unrestricted (e.g., liquid crystals [59]).

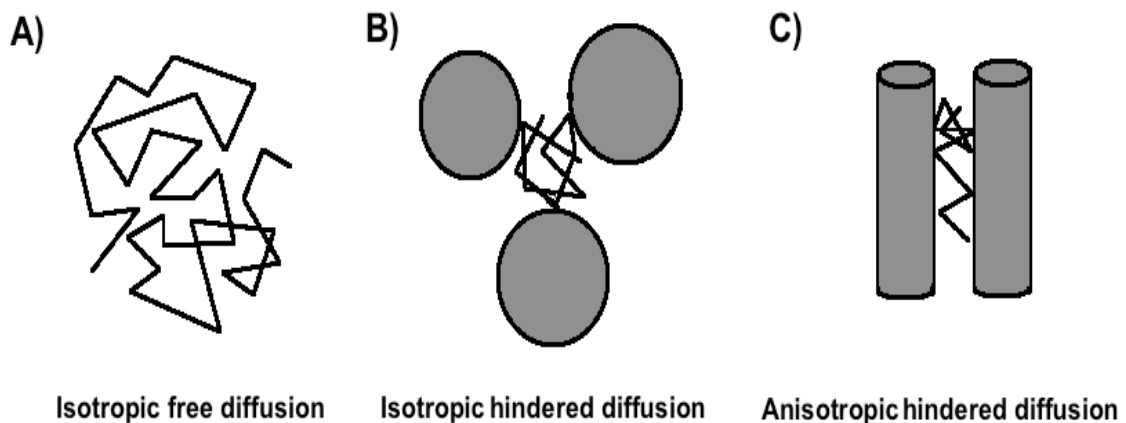


Figure 2.6 Schematic diagrams for water motion in free water and two different mediums.

A) Free water diffusion is isotropic in the absence of any obstacles. B) Water diffusion outside the spheres is isotropic and hindered in the presence of the random barriers. C) Water diffusion outside the cylinders is anisotropic and hindered due to the aligned barriers to water movement.

2.3. Models of DWI Signal Attenuation

In biological tissue, the displacement of water molecules is affected by the packing of cells and consequently DWI signals are sensitive to the structural changes at cellular and subcellular scales. It is a crucial feature of DWI that is particularly appealing for both preclinical and clinical studies. Analytical models of water diffusion in tissue have been proposed to provide quantitative information about the underlying tissue microstructure. The analytical models of water diffusion can be broadly classified into two categories: phenomenological models and compartment models. Phenomenological models aim to provide reliable mathematical descriptions of DWI signals but have limited biophysical insights. Compartment models are constructed based on diffusion properties of each structural compartment within a tissue and aim to offer parameters directly related to the specific tissue structure. Compartment models have proven successful in brain imaging and have recently gained much attention outside of the brain. This section provides a review of models of water diffusion in tissue.

2.3.1. Phenomenological Models

Free diffusion describes the random motion of water molecules in the absence of any obstacles. In heterogeneous biological tissue, however, water molecules are constantly interacting with various tissue elements and thus water motion is highly complex. In such case, the self-diffusion coefficient D in Eq. 2.5 is replaced by a global parameter called ADC to characterize the complex diffusion in tissue.

$$S = S_0 e^{-bADC} \quad [2.10]$$

This simple monoexponential model is also known as the ADC model. The acquisition of DWI images with one zero b -value and one nonzero b -value (e.g., 0 and 1000 s/mm²) is often performed for clinical studies. The ADC generally displays a lower value in cancer than in healthy tissue. ADC is an overall concept that encompasses all concurrent motion effects in tissue. These motion effects include restricted diffusion, hindered diffusion, perfusion, and water exchange between compartments. Consequently, the ADC model is not able to provide specific information on tissue structure. The calculated ADC may be highly dependent on DWI protocols and signal analysis methods, although this is rarely mentioned in the clinical DWI literature [60].

In heterogeneous tissue where water molecular motion is not equal for all directions, a single ADC is insufficient to characterize the diffusion process at the voxel scale. Diffusion tensor imaging (DTI) assuming a three-dimensional Gaussian model of water molecular displacement generalizes the ADC model to assess the anisotropy of the tissue [16].

The diffusion tensor is a symmetric 3×3 matrix:

$$\begin{bmatrix} D_{xx} & D_{xy} & D_{xz} \\ D_{xy} & D_{yy} & D_{yz} \\ D_{xz} & D_{yz} & D_{zz} \end{bmatrix}$$

Moreover, the relationship between the tensor D and the DWI signal is as follows:

$$S = S_0 e^{-\sum_{i=x,y,z} \sum_{j=x,y,z} b_{ij} D_{ij}} \quad [2.11]$$

where b_{ij} is a component of the symmetric b -matrix calculated from the applied diffusion gradient vector (G_x, G_y, G_z). The tensor has an ellipsoidal surface. In an isotropic medium, the diffusion ellipsoid is a concentric sphere. In an anisotropic medium, the diffusion is modelled with an elongated ellipsoid. At least six diffusion-encoded image sets acquired along noncollinear directions and one $b = 0$ s/mm^2 image set are required to estimate all six diagonal and off-diagonal elements of the tensor.

There are a number of parameters used for describing the orientation, size and shape of the diffusion tensor. The tensor D is diagonalized via a linear rotation to derive three principal axes of the diffusion tensor, known as the eigenvectors $[\vec{\varepsilon}_1, \vec{\varepsilon}_2, \vec{\varepsilon}_3]$ and their associated eigenvalues $\lambda_1, \lambda_2, \lambda_3$. The primary eigenvector $\vec{\varepsilon}_1$ and its associated eigenvalue λ_1 indicate the direction and magnitude of the highest diffusion respectively. λ_2 and λ_3 represent the magnitudes of diffusion along $\vec{\varepsilon}_2$ and $\vec{\varepsilon}_3$ that are perpendicular to $\vec{\varepsilon}_1$.

Of all the diffusion metrics derived from the tensor, mean diffusivity (MD) and fractional anisotropy (FA) are the most frequently used parameters for clinical studies because they are rotationally invariant. MD is the mean of the three eigenvalues and characterizes the size of the diffusion ellipsoid:

$$MD = (\lambda_1 + \lambda_2 + \lambda_3)/3 \quad [2.12]$$

FA measures the degree of directionality of diffusivity within a voxel and characterizes the shape of the diffusion ellipsoid:

$$FA = \frac{\sqrt{(\lambda_1 - \lambda_2)^2 + (\lambda_2 - \lambda_3)^2 + (\lambda_3 - \lambda_1)^2}}{\sqrt{2\lambda_1^2 + 2\lambda_2^2 + 2\lambda_3^2}} \quad [2.13]$$

The values of FA range from 0, in an isotropic medium, to 1, in the case of perfectly linear diffusion along the primary eigenvector.

Both ADC and DTI models assume the Gaussian distribution of molecular motion. However, the DWI signal attenuation in the heterogeneous tissue is widely observed to be non-Gaussian. Several models have been proposed to quantify this deviation from the Gaussian behaviour.

It is well known that tissue exhibits non-monoexponential diffusion decay, particularly over a broad range of b -values (e.g., b : 0 - 3000 s/mm²). In such case, a biexponential model has been extensively used and has been shown to offer a better fit to the data [10-12]:

$$S = S_0[(1 - f)e^{-bD_s} + fe^{-bD_f}] \quad [2.14]$$

where D_s and D_f are the slow and fast diffusion coefficients respectively, and $(1 - f)$ and f are their fractions. The biexponential model requires a wide range of b -values with the maximum value that is typically ≥ 2000 s/mm². However, the exact origin of biexponential behaviour remains unclear. A common explanation associates D_f and D_s in the biexponential function with extra- and intracellular compartments, respectively, yet this assignment is controversial [61-63]. Furthermore, biexponential behaviour has been observed for the signal decay from the intracellular compartment alone [64].

The kurtosis model has been introduced to quantify the non-Gaussian diffusion behaviour by using excess kurtosis [13]

$$S = S_0 e^{-bD_k + \frac{K}{6}b^2D_k^2} \quad [2.15]$$

where K is the kurtosis reflecting the degree of the complexity of the tissue, and D_k represents non-Gaussian diffusion coefficient. The estimation of diffusion kurtosis needs DWI images acquired with at least three b -values including high b -value (about

2000 s/mm²) [65]. Although the biophysical interpretation of K is less straightforward, K has been shown to provide greater accuracy than ADC in detecting cancer [28,65,66].

A stretched exponential model assumes that there are a large number of Gaussian components having a continuous distribution of diffusivities and has been used to characterize the intravoxel heterogeneity [15]:

$$S = S_0 e^{-(bD_s)^\alpha} \quad [2.16]$$

where D_s is coined as distributed diffusion coefficient, and α is the stretching parameter ($0 < \alpha \leq 1$). The parameter α characterizes the deviation of the signal decay from monoexponential behaviour. When α is 1, the stretched exponential model becomes a monoexponential model. Lower values of α signify increasing number of separate proton pools within the voxel, suggesting a higher degree of the heterogeneity.

The biexponential model is generalized to a multiexponential model [67]:

$$S = S_0 \sum_{i=1}^n f_i e^{-bD_i} \quad [2.17]$$

where $n \geq 3$, f_i is the volume fraction of the i th component, and the sum of f_i is 1. The multiexponential model adds extra freedom for the model to fit the data compared with the biexponential model. A study of water diffusion in brain tissue has demonstrated that DWI signal decay is better fitted by a triexponential function than monoexponential and biexponential models [68].

2.3.2. Compartment Models

The general aim of clinical DWI is to infer tissue structure properties, particularly pathology, from measurements of diffusion attenuation under conditions of varying diffusion times and diffusion-weightings. For this purpose, compartment models are more useful than phenomenological models. Because compartment models are based on assumptions about tissue geometry and thus their model parameters are directly related to properties of the tissue structure. Compartment model sees biological tissue as a combination of compartments. These compartments represent separate populations of water molecules in distinct structural environments. In this way biological tissue can be roughly divided into intracellular and extracellular spaces. In the absence of exchange

between intracellular and extracellular compartments, the DWI signal S can be expressed as a summation of the signals from these two spaces,

$$S = f_i S_i + f_e S_e \quad [2.18]$$

where S_i represents the signal from water in the intracellular space, S_e represents the signal from water in the extracellular space, and f_i and f_e are the signal fractions of these two water pools, with $f_i + f_e = 1$. The precise formula of Eq. 2.18 depends on the shape and arrangement of cellular structures and can be modified to account for the permeability of cell membranes. Multi-compartment models have proven successful in brain white matter. White matter is mainly composed of axons, which are arranged in parallel bundles. Two-compartment models, based on intra- and extra-axonal compartments, have been proposed to model white matter [17-19,69]. These two-compartment models often assume restricted diffusion inside axons and hindered diffusion outside axons. Other models described diffusion in white matter with three or more compartments by including other cellular structures, such as the myelin sheath, glial cells, and cerebrospinal fluid regions [20,21,70,71].

However, compartment models generally lack for non-neural tissue. One of the early attempts is to model DWI signals in tissue in vivo with a two-compartment model called intravoxel incoherent motion (IVIM) instead of the ADC model when the measurement is performed at low b values ($< 200 \text{ s/mm}^2$) [72,73]. In such case, the DWI signal decay is not Gaussian anymore due to the perfusion effects of the blood vessel in tissue in vivo. The IVIM model divides the tissue into vascular and non-vascular spaces and is represented by a biexponential function

$$S = S_0 [(1 - f)e^{-bD} + fe^{-bD^*}] \quad [2.19]$$

where f is perfusion fraction, D the diffusion coefficient and D^* the perfusion coefficient. The IVIM model has been widely used for many cancer types such as prostate [74], breast [75], and kidney [76], showing that IVIM parameters may offer additional information for tissue characterization.

A three-compartment model called VERDICT, which describes tissue as a composition of intracellular, extravascular-extracellular and intravascular compartments, has been recently used to model colorectal cancer [41]. The signal for the VERDICT model is

$$S = \sum_{i=1}^3 f_i S_i \quad [2.20]$$

where signal S_1 is from water inside cells, S_2 is from water outside cells and blood vessels, S_3 is from water in blood vessels, and f_i is the signal fraction of the corresponding compartment. The precise form of each compartment model depends on a tissue type. The VERDICT model parameters including cell radius and vascular volume fraction were in good agreement with histology of colorectal tumors. More importantly, VERDICT model successfully distinguished two types of colorectal tumors and reflected the effects of chemotherapy treatment by the differences in the parameters while the ADC and biexponential models failed to detect either of these differences. A subsequent study applied VERDICT model to prostate tissue in vivo [42]. It showed that VERDICT model differentiated cancer from benign tissue more reliably than the ADC and biexponential models. These pioneering studies on compartment models have demonstrated their superiority in cancer detection and inference of tissue microstructure over phenomenological models. To model water diffusion in non-neural tissue, two important effects should be taken into account:

- Water molecules inside cells will experience restricted diffusion.
- Water molecules in the extracellular space will experience hindered diffusion.

Depending on cell types, cellular membranes might be considered either permeable or impermeable to water molecules during diffusion time of the MRI experiment. In this study, it is assumed there is no water exchange between compartments. To model restricted and hindered diffusion in non-neural tissue, five single-compartment models that have been used for white matter [23] are selected (Table 2.1). They are as follows:

1. The first is an isotropic tensor, which is referred as a ‘Ball’. The model has only one parameter, the diffusivity D .
2. The second referred to as ‘Zeppelin’, is a cylindrically symmetric tensor. The model has the principle eigenvector ε , parallel diffusivity D_{\parallel} , perpendicular diffusivity D_{\perp} .

3. The third is a conventional single-component DTI model that is referred as ‘Tensor’. The model provides the following parameters: parallel diffusivity D_{\parallel} , two perpendicular diffusivities $D_{\perp 1}$, $D_{\perp 2}$, and three orthogonal eigenvectors ε , $\varepsilon_{\perp 1}$, $\varepsilon_{\perp 2}$.
4. The fourth is ‘Stick’ model assuming diffusion within idealized cylinder of zero radius. The model has a direction n and diffusivity D as parameters.
5. The ‘Sphere’ model describes restricted diffusion inside impermeable spherical pore with a non-zero radius R_s .

The analytical expression for ‘Sphere’ model is obtained using the Gaussian phase distribution approximation and is given by

$$\ln S = -2\gamma^2 G^2 \sum_{m=1}^{\infty} \frac{2Da_n^2\delta - 2 + 2e^{-Da_n^2\delta} + 2e^{-Da_n^2\Delta} - e^{-Da_n^2(\Delta-\delta)} - e^{-Da_n^2(\Delta+\delta)}}{D^2 a_n^6 (R^2 a_n^2 - 2)} \quad [2.21]$$

where D is the free diffusion constant and a_n is the n th root of the Bessel equation $(a_n R) J'_{\frac{3}{2}}(a_n R) - \frac{1}{2J_{\frac{3}{2}}}(a_n R) = 0$, where J is the Bessel function of the first kind.

In this study, the applications of compartment models in four types of non-neural tissue have been investigated. These four types are prostate, breast, lymph node and cultured cells.

Table 2.1 Candidate compartment models for non-neural tissue

(Reproduced from [23] with permission from Elsevier, UK)

Model	Form ^a	Degrees of freedom
 Ball	$\mathbf{D} = D\mathbf{I}$	D
 Zeppelin	$\mathbf{D} = \alpha\boldsymbol{\varepsilon}\boldsymbol{\varepsilon}^T + \beta\mathbf{I}, D_{\parallel} = \alpha + \beta, D_{\perp} = \beta$	$D_{\parallel}, D_{\perp}, \theta, \phi$
 Tensor	$\mathbf{D} = D_{\parallel}\boldsymbol{\varepsilon}\boldsymbol{\varepsilon}^T + D_{\perp 1}\boldsymbol{\varepsilon}_{\perp 1}\boldsymbol{\varepsilon}_{\perp 1}^T + D_{\perp 2}\boldsymbol{\varepsilon}_{\perp 2}\boldsymbol{\varepsilon}_{\perp 2}^T$	$D_{\parallel}, D_{\perp 1}, D_{\perp 2}, \theta, \phi, \alpha$
 Stick	$S = e^{-bD(n\mathbf{G})^2}$	D, θ, ϕ
 Sphere	GPD approximation. $R_s > 0$	D, R_s

a) \mathbf{D} is the diffusion tensor. \mathbf{I} is the identity tensor. θ, ϕ, α are tensor angles.

2.4. Prostate Tissue

2.4.1. Anatomy and Histology

The prostate consists of three major glandular regions and an anterior fibromuscular layer. These three regions are the peripheral zone (PZ), the central zone (CZ) and transition zone (TZ), which differ histologically and biologically (see Figures 2.6 and 2.7). The CZ comprises about 25% of the total prostate volume and has the shape of an inverted cone immediately surrounding ejaculatory duct orifices to form part of the prostate base [77]. The PZ comprises about 70% of the prostate volume and extends posterolaterally around the CZ and distal prostatic urethra. The TZ consists of two independent small lobes lying anterolaterally to the proximal prostatic urethra. Approximately 70%-75% of prostate cancers occur in the PZ and 20%-30% in the TZ. Cancers originating in the CZ are rare [78].

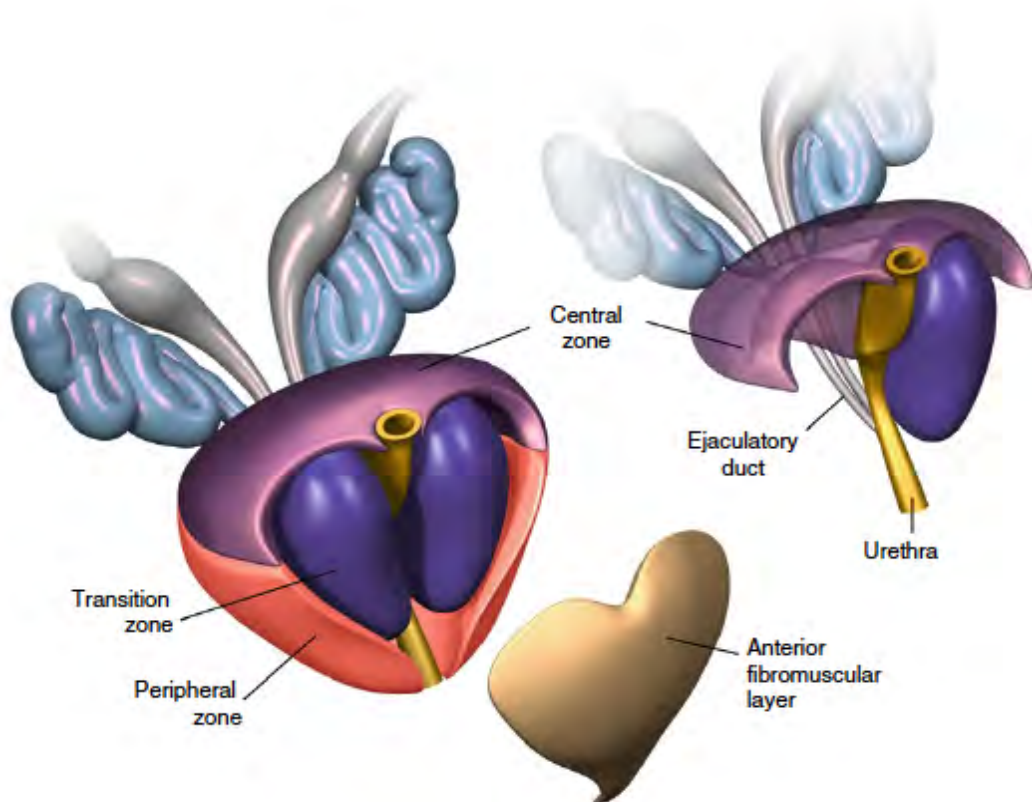


Figure 2.7 The anatomy of the prostate

(Reproduced from [79] with permission from Springer-Verlag Berlin Heidelberg, Germany)

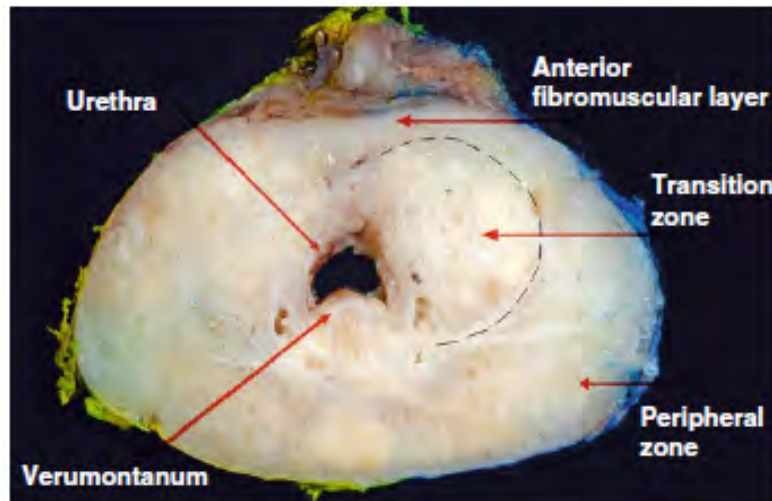


Figure 2.8 Coronal section of the prostate.

It shows the location of the peripheral zone and transition zone in relation to the proximal urethral and verumontanum. (Reproduced from [79] with permission from Springer-Verlag Berlin Heidelberg, Germany)

Histologically, the prostate gland is globally composed of epithelium and stroma (Figure 2.8a) [80]. The prostate epithelial cells represent a continuum of differentiation from basal cells to secretory cells (Figure 2.8b). Secretory cells are cuboidal or columnar-shaped with clear to pale cytoplasm and pseudostratified nuclei. Basal cells are situated at the periphery of the gland beneath the secretory cells with blue-grayish, smooth nuclei. Adenocarcinoma of the prostate is an epithelial malignancy that happens in aging men. Over 95% of prostate cancers are adenocarcinomas [81]. Therefore, the prostate epithelial cells play a major role in the development of benign and malignant disorders.

If a prostate cancer region is found in a tissue sample, the Gleason grading scheme is used to quantify the degree of malignancy [82]. The Gleason grading system is based on architectural features of prostate cancer and has five patterns (Figure 2.9).

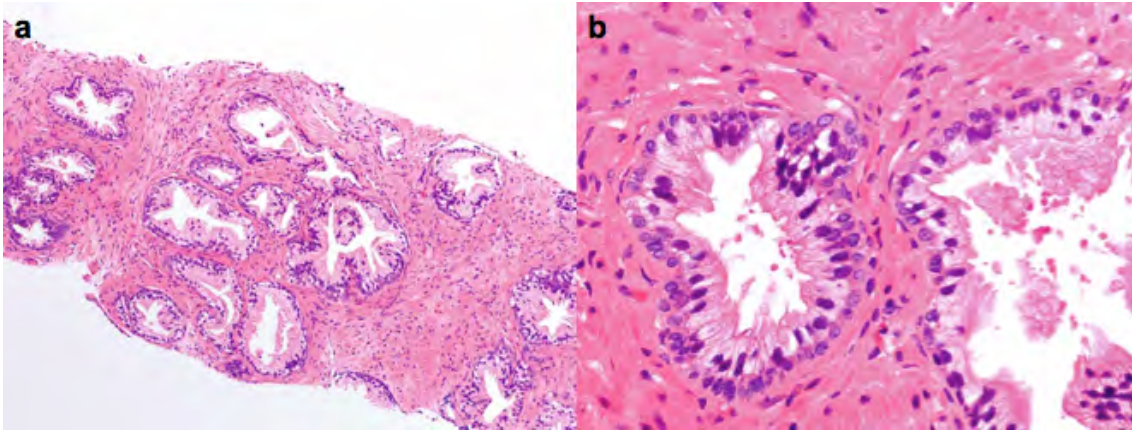


Figure 2.9 Histology of the normal prostate gland.

(a) Benign prostatic tissue. Prostate glands form lobulated architecture with intervening fibromuscular stroma. (b) Normal prostate glands. They consisted mainly of secretory cells and basal cells. (Reproduced from [79] with permission from Springer-Verlag Berlin Heidelberg, Germany)

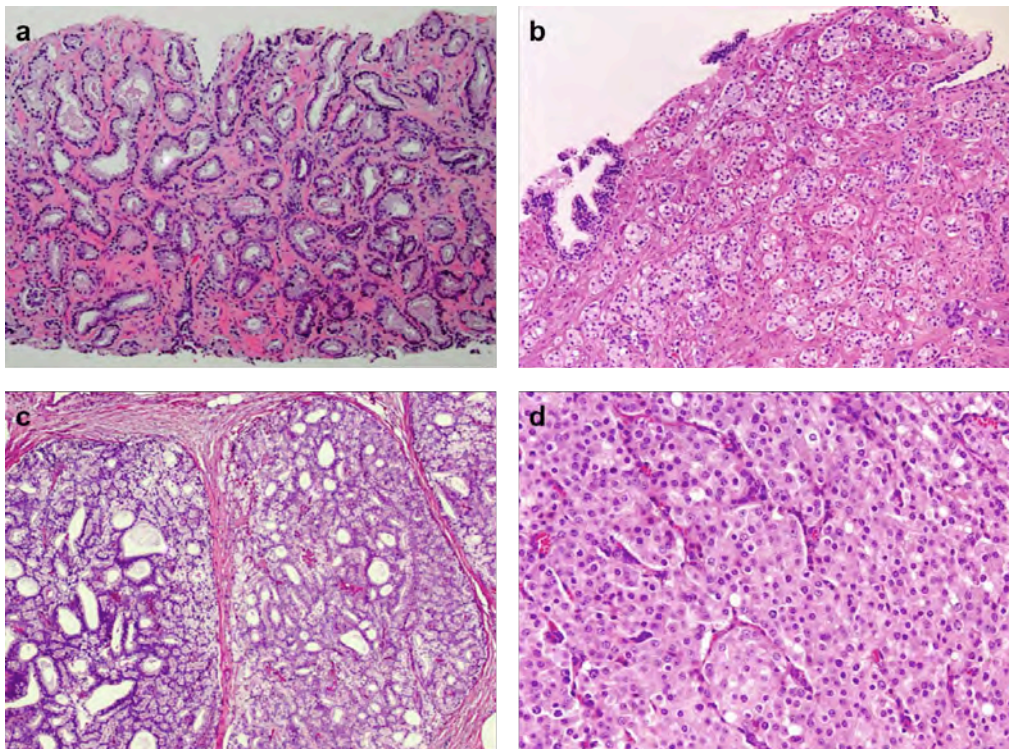


Figure 2.10 Morphologic spectrum of Gleason patterns.

(a) Gleason pattern 3. (b) A cluster of poorly formed glands representing Gleason pattern 4. (c) Gleason pattern 4 cribriform carcinoma. (d) Solid nest representing

Gleason pattern 5. (Reproduced from [79] with permission from Springer-Verlag Berlin Heidelberg, Germany)

2.4.2. Models of DWI in Prostate Tissue

Prostate cancer is the most common cancer diagnosed in Australia and the third most common cause of cancer death [83]. The most commonly used tests to aid early detection of prostate cancer are digital rectal examination and serum prostate-specific antigen level. However, both tests result in overdiagnosis and overtreatment [84], as well as systematically miss significant tumor [85]. Recently, a great interest has been shown for multi-parametric magnetic resonance imaging (mpMRI), which includes T₂-weighted imaging (T2W), dynamic contrast-enhanced MRI (DCE) and DWI. mpMRI is increasingly being used to assist target biopsy, risk stratification and treatment selection for prostate cancer [4,5]. To uniform and standardize reports of mpMRI of the prostate, the European Society of Urogenital Radiology published a unified Prostate Imaging Reporting and Data System (PI-RADS) in 2012 and upgraded to PI-RADS version 2.0 in 2015 [78,86]. The sensitivity and specificity of T2W for prostate cancer vary widely [87]. DCE needs intravenous administration of contrast medium. DWI is the most reliable component of the mpMRI exam. A clinical study has shown that DWI correlates more strongly with both cancer grade and volume than do T2W and DCE [88].

Most clinical DWI studies applied ADC model and found that ADC values were lower in prostate cancer compared to normal prostate, indicating reduced water mobility [26,27,89-92]. Also, ADC values showed a moderate negative correlation with Gleason score [93,94].

In fact, it has been shown that DWI signal decay in prostate tissue in vivo is non-monoexponential at least in two regimes: over a range of low b -values (< 200 s/mm²) and over an extended b -value range including high b -values (> 2000 s/mm²) [10,95]. Besides, ADC values of malignant and benign tissue in the PZ and TZ showed a considerable overlap [96]. As the ADC model is a poor descriptor of complex diffusion environment of prostate tissue, more sophisticated models have been employed to describe non-monoexponential diffusion signals.

For measurements over a range of low b -values, the IVIM model has been used to separate true water diffusion from perfusion within capillaries in prostate tissue.

However, some studies reported that the IVIM model did not yield a clear added value for tumour detection as compared with the ADC model [95,97,98]. Other studies demonstrated that IVIM parameters were significantly different between prostate cancer and normal prostate [74,99]. Although these two studies found that the diffusion coefficient D of the IVIM model was significantly lower in prostate cancer than normal tissue, the perfusion fraction f was unexpectedly lower in tumour, which disagreed with findings in a DCE study of prostate cancer [100] and angiogenesis [101]. Another study reported a higher f in prostate cancer as compared with normal tissue [102].

In the healthy prostate and prostate cancer, the biexponential model provided a statistically better fit to the signal decay curve obtained over an extended b -value range [10,11]. Two studies showed that the biexponential model parameters differed significantly for discriminating prostate cancer from benign tissue [11,37].

The kurtosis model has been evaluated in terms of prostate cancer detection. Two studies [28,65] found that the kurtosis model may contribute to the diagnosis of prostate cancer while one study [103] reported no significant benefit of the kurtosis model for cancer detection in the PZ as compared with the ADC model.

The stretched model has been used for distinguishing prostate cancer and normal tissue. One study found that both distributed diffusion coefficient (D_s) and stretching parameter (α) were significantly lower in tumour than normal tissue [30].

A recent study used the triexponential model for diagnosing prostate cancer and suggested that the triexponential model could provide more detailed information on diffusion and perfusion of prostate cancer than the biexponential model [29].

Many studies investigated the feasibility of the DTI model for prostate cancer detection. MD values have been shown to be lower in tumors than in normal prostate [104-107]. However, measurements of diffusion anisotropy in prostate tissue have produced equivocal results with widely differing FA values [104,105,108-111]. It has been shown that low signal to noise ratios will lead to artificially high FA values [111,112]. A combined in vivo and ex vivo study of histologically defined prostate cancer reported no significant diffusion anisotropy differences between cancer and benign tissue in the

PZ [113]. An ex vivo study demonstrated a decrease in FA as voxel volume increased and wide variations in average FA between prostates [56].

Clearly, the more complex the model becomes, the more challenging its applicability is. Several groups have compared some of the aforementioned models in terms of fitting quality, the variance of the fitted parameters and theoretical information. Quentin et al. [114] evaluated which phenomenological model (ADC, biexponential, statistical and kurtosis) fitted best to the DWI signal. They showed that a more complex model might provide a better fit to the data, and the ADC model is sufficient to distinguish prostate cancer from normal tissue using b -values ranging from 0 to 800 s/mm². Bourne et al. [39] made a comparison of four popular models (ADC, biexponential, stretched and kurtosis) and found that the biexponential model had highest information for measurements including b -values above 2000 s/mm². Jambor et al. [115] compared the same four models and demonstrated that the kurtosis model is the preferred model for characterization of normal prostate and prostate cancer using b -values up to 2000 s/mm² in terms of fitting quality and variance of the model parameters. Although these advanced models show improvement in data description compared to the ADC model, the biologic interpretation of the model parameters is limited.

Whereas the development of advanced models continues within research settings, the ADC model remains the mainstay approach in clinical practice. Decreased ADC values in cancer tissue are commonly attributed to higher cellularity. The cellularity commonly refers to either nuclear count per unit area or nuclear area per unit area. However, a recent study of fixed prostate tissue has demonstrated that the clinically observed variations of ADC are likely to have mainly resulted from volume changes in the gland compartments (epithelium, stroma and lumen space) of prostate tissue having distinct diffusivities rather than from differences in cellularity [116]. Preliminary diffusion microimaging studies of formalin-fixed prostate tissue reported highly restricted diffusion in the epithelial cell layers, intermediated diffusion in the stroma, and free diffusion in ducts and acinar lumina [117,118]. Fibromuscular stromal tissue exhibited significantly higher diffusion anisotropy than the glandular epithelium and lumen spaces [55]. Fiber tracks generated from DTI data were consistent with stromal myocyte and actin fiber orientation seen on light microscopy [55]. These new findings motivate

the development of compartment models to provide more specific information on prostate tissue.

The first attempt to investigate compartment model of diffusion in fixed prostate tissue was made by comparing the fitting quality of single and multi-compartment models including isotropic restricted Ball-sphere model [119]. This study found that the triexponential model gave the best fit to the data. A three-compartment ‘VERDICT’ model based on vascular, intracellular, and extracellular-extravascular compartments has recently been shown to successfully discriminate between normal and malignant prostate tissue as well as to provide model parameters consistent with histological features, such as cell size [42]. Moreover, an increase in VERDICT intracellular volume fraction was in good agreement with the proliferation of epithelial cells found in prostate cancer [117]. To make clinical adoption of the VERDICT models feasible, an experimental design optimization framework [17] has been used to reduce the scan time. The results showed that the VERDICT model differentiated between cancer and normal tissue, and the optimized protocol allowed stable fitting and sensible parameter estimates [43].

2.5. Breast Tissue

2.5.1. Anatomy and Histology

Breast is an organ whose structure reflects its special function – the production of milk for lactation. The adult female breast spans from the second to sixth/seventh ribs. The superficial and deep fascia of the chest wall encompasses the base of the breast. The breast is composed of skin, superficial fascia, nipple-areola complex, deep fascia and breast parenchyma (Figure 2.10). The parenchyma contains three principal tissue types: glandular epithelium, fibrous stroma, and fat. Glandular epithelium is comprised of 15-20 lobes. Each lobe contains 20-40 terminal ductal lobular units (Figure 2.11), which are the functional units of the breast. The terminal ductal lobular unit consists of intralobular terminal duct, extralobular terminal duct, and lobule. Fibrous stroma and supporting structures are referred to as Cooper’s ligaments. The ligaments are dense connective tissue that holds the breast upward.

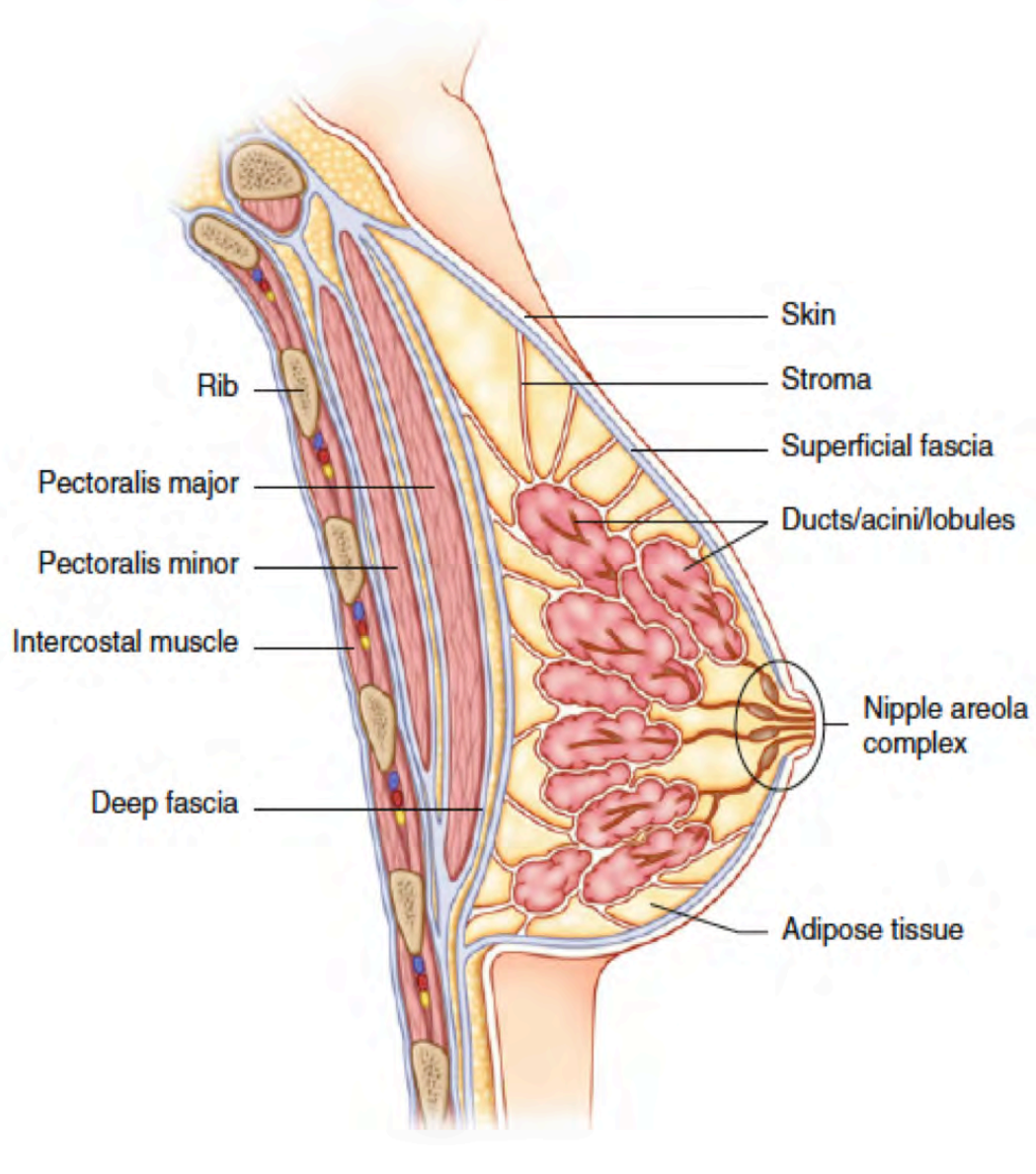


Figure 2.11 Components of the breast

(Reproduced from [120] with permission from Springer International Publishing, Switzerland)

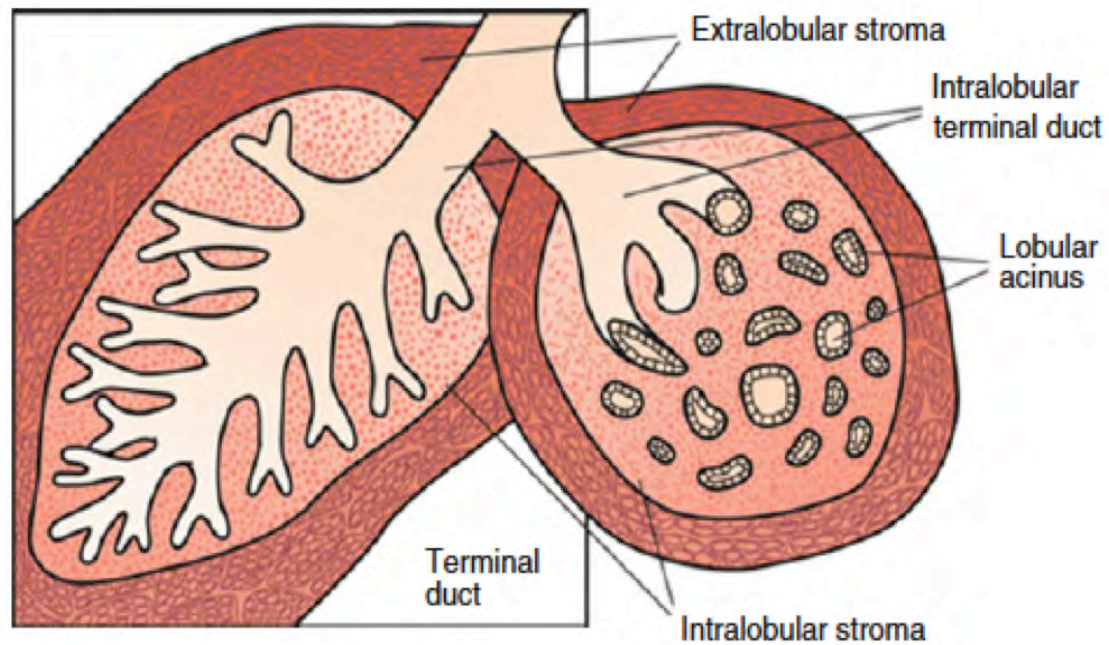


Figure 2.12 Fully developed breast lobular unit

(Reproduced from [120] with permission from Springer International Publishing, Switzerland)

Two of the most frequently encountered benign breast conditions are introduced here. Fibroadenomas is frequently diagnosed in young women, predominantly in the 20s or 30s [121]. They have epithelium and stroma with smooth, well-circumscribed borders. Lipoma is the most common soft tissue tumour in the body, with a prevalence of 2.1 per 1000 people [122]. Its specimen is composed of bland-appearing mature adipocytes.

For breast carcinoma, there are two broad categories with respect to its confinement to the ductal-lobular system of the breast or not. They are carcinoma in situ and invasive carcinoma.

2.5.2. Models of DWI in Breast Tissue

Breast cancer has the highest incidence of all malignancies occurring in women worldwide. Mammography is the primary screening imaging modality for the early detection of breast cancer, but has limitations in terms of sensitivity (39-86%) and specificity (88-94%), depending age and breast density [123,124]. Therefore, ultrasound is used in addition to mammography to improve breast cancer screening. Nevertheless, mammographic screening is associated with the overdiagnosis and ultrasound screening

requires a prohibitively long radiologist's examination time. These inherent problems have stimulated research in the field of MRI. MRI has been established as the most powerful breast imaging technique to support breast cancer diagnosis, staging, and evaluation. MRI has been shown to be superior to mammography for the diagnosis of primary or recurrent invasive or intraductal cancer [125,126]. DCE of the breast is the central modality of breast MRI as it provides detailed morphologic information, and, to some extent, functional information, which yields an excellent sensitivity [127,128]. However, it is limited by a low specificity [129,130]. Among all functional MRI parameters, DWI with quantitative ADC mapping has emerged as a valuable adjunct to DCE to provide additional specificity [6,7,131]. Mammography, ultrasound, and MRI are scored in seven categories according to the American College of Radiology Breast Imaging Reporting and Data System (BI-RADS): category 0, incomplete; 1, negative; 2, benign; 3, probably benign; 4, suspicious; 5, highly suggestive of malignancy; 6, known biopsy-proven malignancy [132].

Many studies have demonstrated significant differences in the ADC values of benign and malignant breast lesions [7,133-138]. The ADC value of malignant lesions is usually lower than that of benign lesions. ADC has also been proven useful for differentiating between invasive breast cancer and noninvasive ductal carcinoma in situ [139]. A recent study reported high reproducibility, repeatability and diagnostic accuracy of ADC values in breast lesions [140]. In the meanwhile, it is important to realize that there are no standard measurement protocols and data processing methods for DWI [141]. The ADC values are affected by acquisition parameters and physiological parameters such as perfusion [133].

Although the ADC model has widespread application in breast DWI, the biophysical basis of reduced ADC in malignant lesions remains poorly understood. There is an increasing use of advanced models to characterize both normal and cancer tissue. These models are expected to enable more powerful differentiation and classification of disease by providing additional specificity in the description of breast tissue.

Recently, the use of the IVIM model in the breast has gained attention for its sensitivity to microvascular flow. Numerous groups have found that the IVIM model parameters, the tissue diffusivity (D) and the perfusion fraction (f) show significant differences between benign and malignant lesions (significantly lower D and higher f in malignant

lesions compared with benign lesions) [142-147]. Two studies reported that a combination of D and f improved diagnostic accuracy [142,146].

The observed diffusion signal decay over an extended range of b -values is non-monoexponential. The kurtosis model has been used to describe this behaviour in breast tissue. Several studies reported significantly higher kurtosis K in malignant lesions compared with benign lesions, suggesting that K added to the diagnostic accuracy of ADC alone [66,148,149].

A model combining IVIM with kurtosis showed higher perfusion fraction, lower ADC_0 (ADC obtained at $b = 0$) and higher kurtosis in malignant lesions than in benign lesions and normal tissue using b -values up to 2500 s/mm^2 [150].

DTI extends ADC by probing water motion in six or more directions to measure the full diffusion tensor. Many studies have demonstrated the feasibility of DTI characterization of normal breast [33,151] and breast cancer [152-157]. These studies reported lower MD values in breast cancer as compared with benign lesions. However, the results for FA were contradictory. Several studies reported that FA values were significantly different between benign and malignant lesions [152,154,155] and others found no difference in FA [153,156,157].

The biexponential model has been used to investigate water diffusion in the breast cancer [12,158]. They found that DWI signal decay in tumours was better fitted by a biexponential function than a monoexponential function, and the slow component fraction of the biexponential model had a positive correlation with the cellular fraction. A recent study applied the stretched model to characterization of structural heterogeneity in breast cancer and demonstrated its diagnostic benefit [159].

Further improvements in modelling of DWI signal decay are desired for a better understanding of the physiologic basis of DWI. Preliminary diffusion microimaging study of fixed breast tissue reported low diffusivity of epithelial cells relative to supporting fibrous stroma [160]. This finding is similar to that previously reported in prostate [117,118] and esophagus [161]. These ex vivo microimaging results can serve as a basis for developing more advanced models that can provide biophysical specificity.

A three-compartment VERDICT model that characterizes water diffusion in intracellular, vascular and extracellular-extravascular spaces has shown success in differentiating two colorectal tumor types with different cell morphology [41]. The precise form for each compartment within the VERDICT framework is application dependent. Motivated by this work, a number of versions of VERDICT have been applied to breast tumours in vivo [162]. They were Ball-ball-sphere, Ball-stick-sphere and Ball-zeppelin-sphere models. The results demonstrated that the Ball-ball-sphere model best explained the data and its parameters were consistent with histology (cellularity and cell radius). A subsequent study fitted a number of one- and two-compartment models to ex vivo data and found that two-component anisotropic and restricted models (Zeppelin-sphere and Tensor-sphere) best characterized the signals in glandular breast tissue [163].

2.6. Cultured Cell Constructs

2.6.1. 3D culture system

Multicellular spheroids are analogous to avascular tissue in vivo [164]. The physical characteristics of spheroids including size, cell density, metabolites and proliferation gradients are tumour type dependent [165]. Due to metabolic waste accumulation caused by inefficient mass transport in spheroids [164], a spheroid with a size above 500 μ m in diameter commonly displays a layer-like structure consisting of a necrotic core, a middle layer of quiescent cells and an outer layer of proliferating cells (Figure 2.12) [166].

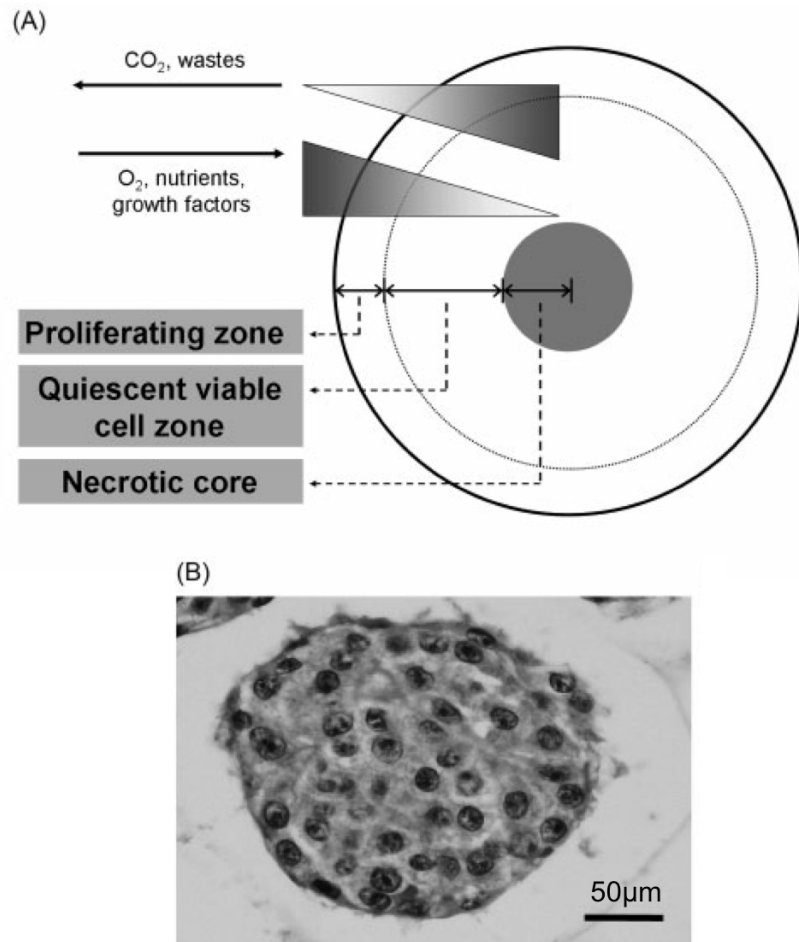


Figure 2.13 Microenvironments inside a spheroid.

(A) Tumor spheroids exhibit spherical geometry with a concentric organization of dead, quiescent and proliferating cells. (B) Hematoxylin-and-eosin staining of an HepG2 hepatoma spheroid. Note the cells that differentiate into smooth, epithelium-like surface on the spheroid. (Reproduced from [166] with permission from John Wiley and Sons, Germany)

2.6.2. Models of DWI in Cell Constructs

Multicellular three-dimensional (3D) spheroids are being used with increasing frequency in various aspects of cancer research. Spheroids can closely mimic the tumor environment by culturing cells in a spatially relevant manner, encouraging cell-cell and cell-matrix interactions [167]. These interactions enable the 3D-cultured cells to acquire morphological and cellular characteristics relevant to *in vivo* tumors [168]. In contrast, conventional two-dimensional (2D) cultured cells are grown as monolayers, losing physiological extracellular matrix and high serum concentrations that are present in

native tumors [169]. Consequently, 2D-cultured cells lose relevant properties and introduce artificial effects. Recent reports demonstrate low-diffusivity epithelia in prostate [118], breast [160], and esophagus tissue [170]. Cultured epithelial cell spheroids recapitulate the complex 3D microenvironment of glandular epithelia and therefore provide an ideal biological model system for investigation of the distinctive structural properties that may contribute to the observed low water mobility.

DWI has become a well-established clinical [7,31,87] and preclinical [23,39,55,161] tool for characterization of biological systems. Nevertheless, to date, there are few DWI studies of spheroids. The measured apparent diffusivity has been used for investigating compartmentation of diffusion in tumor spheroids [171,172]. They demonstrated the presence of slow and fast compartments in spheroids. One study found that these distinct diffusion compartments also differed in T_2 relaxation, with significantly shorter T_2 for the slow compartment than for the fast compartment [171]. A recent study reported that the diffusivity of hydrogel-based spheroids was sensitive to both cell proliferation and Taxol treatment [173].

2.7. Lymph Node Tissue

2.7.1. Anatomy and Histology

The lymphatic system is a network of variable lymph vessels and lymph nodes that run throughout the body (Figure 2.13). It is an important part of our immune system. The lymphatic system defends the body from bacteria and other infections and destroys old or abnormal cells. The lymph nodes are oval or bean-shaped structures, 0.1-2.5 cm long that lie along the course of lymph vessels [174]. Each lymph node consists of fibrous capsule and parenchyma (Figure 2.14). The fibrous capsule invests the entire node and is separated from the parenchyma by subcapsular sinus. The parenchyma is divided into cortex and medulla.

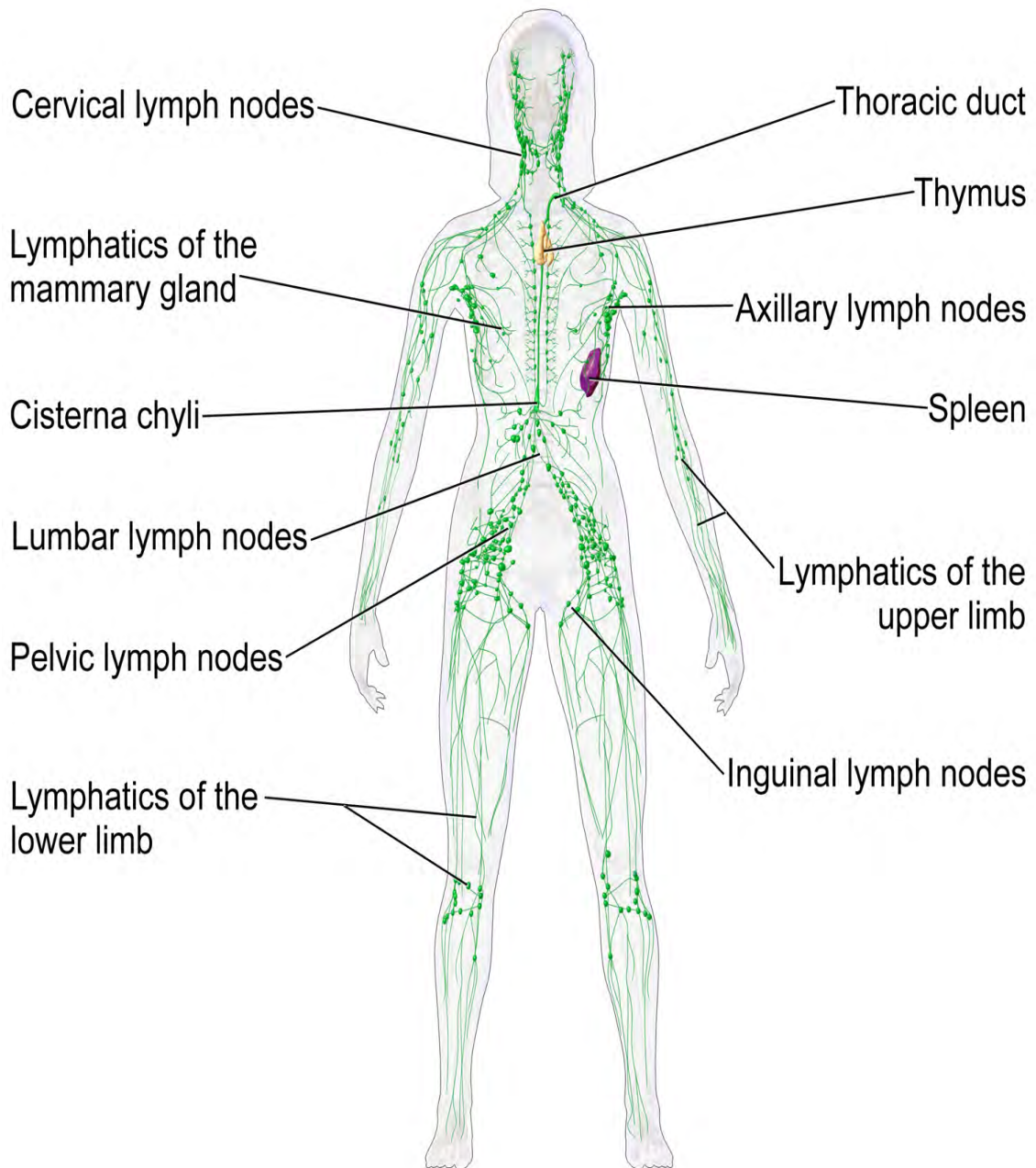


Figure 2.14 Schematic diagram of a female being showing major locations of lymph nodes, thoracic duct, thymus, spleen and other lymph vessels

(Reproduced from [175] with permission from Wikimedia Foundation, US)

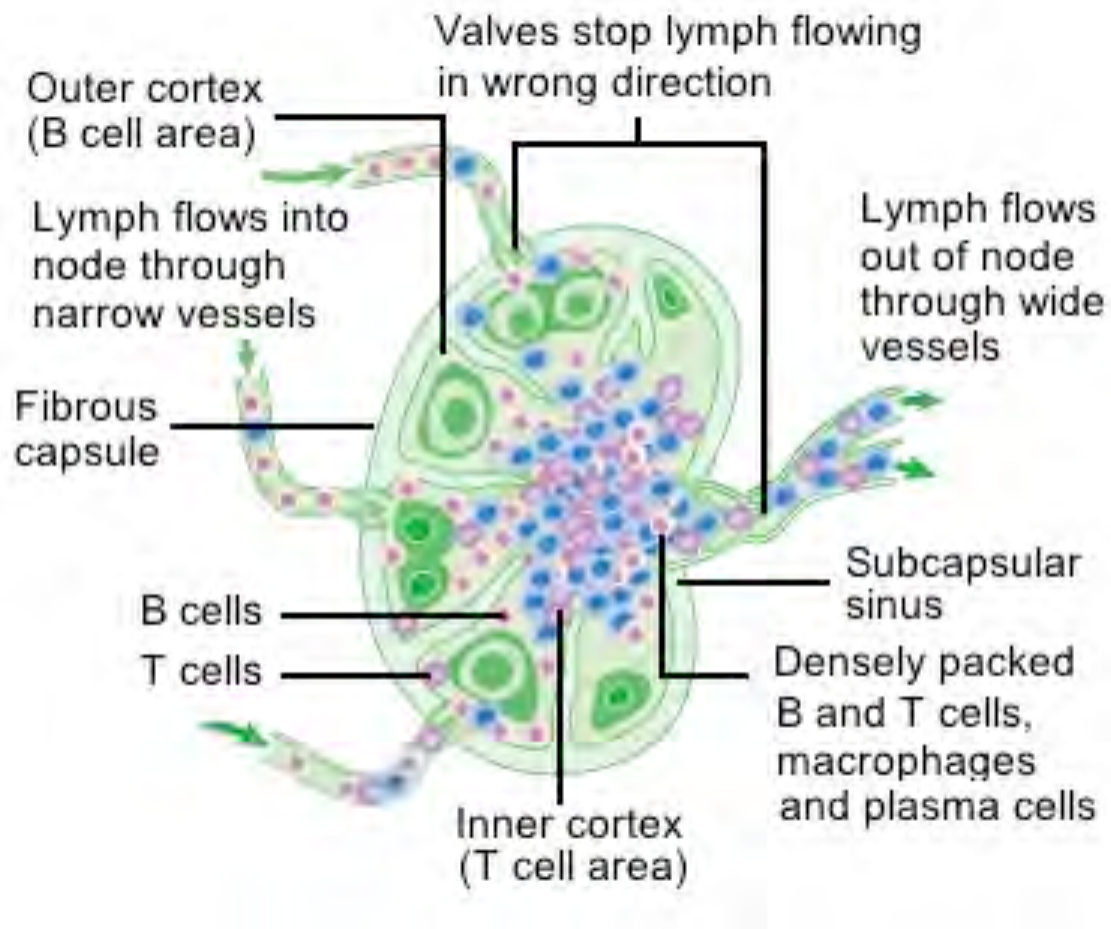


Figure 2.15 Structure of a lymph node

(Reproduced from [176] with permission from Cancer research, UK)

The normal lymph node is populated mostly by lymphocytes and usually <1 cm in size (Figure 2.15A) [177]. Lymphoma is cancer that starts in lymphatic cells (Figure 2.15B). There are dozens of subtypes of lymphomas. Metastatic lymph nodes represent involvement of lymph nodes by non-lymphoid tumours (Figures 2.15C and 2.15D) [178].

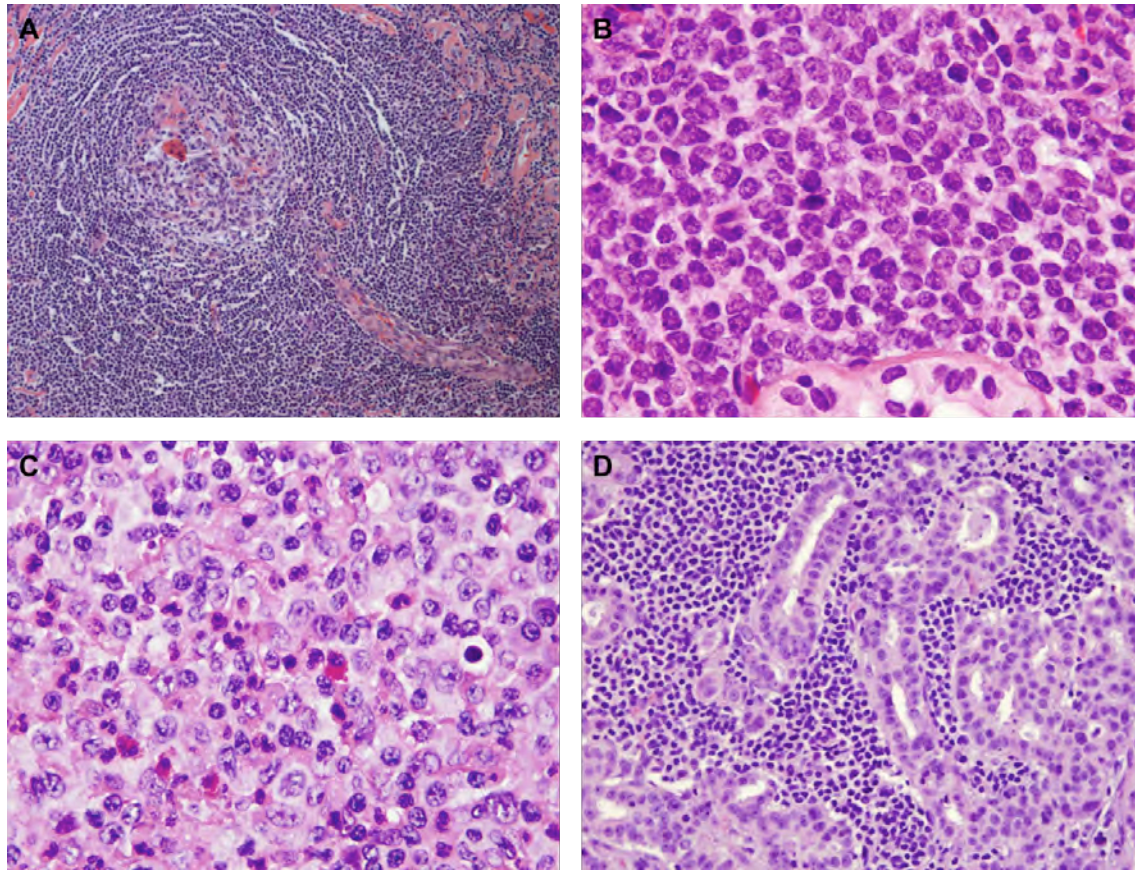


Figure 2.16 Histology of normal and malignant lymph nodes

(A) Involved germinal center, with depletion of germinal center lymphocytes and depletion of the marginal zone. (B) B-lymphoblastic lymphoma/leukemia. (C) Metastatic nasopharyngeal carcinoma. (D) Metastatic breast carcinoma in axillary lymph node. (Reproduced from [178] with permission from Springer New York, US)

2.7.2. Models of DWI in Lymph Node

The detection and accurate staging of lymph node metastases are important for the prognosis, treatment, and follow-up of oncological patients. Lymph node dissection is the golden standard for assessing nodal involvement but increases the risk of complications by exposing the patient to dissection-related sequelae and morbidity [179]. As a result, non-invasive imaging by computer tomography (CT), conventional MRI, ultrasonography or positron emission tomography has been used for nodal staging. The criteria used by these imaging techniques to date are morphological features including nodal size, shape, borders, extracapsular spread, and abnormal internal architecture. The size is the most used criterion for determining nodal metastases. However, neither CT nor conventional MRI is sufficient to discriminate benign from

malignant lymph nodes by applying the size criterion. DWI is an imaging tool yielding unique information that reflects microstructural alterations in tissue. Accumulating evidence shows that DWI may be helpful in discriminating between malignant and non-malignant lymph nodes by using ADC [34-36]. A recent systematic review of eighty studies reported that DWI had higher sensitivity (84%), specificity (95%) and area under curve (0.95) for detection of pelvic lymph node metastasis and recommended DWI as the first choice for metastasis exclusion [180]. Another review of thirteen studies showed that DWI appeared to be a reliable method for differentiation between metastatic and nonmetastatic lymph nodes in breast cancer patients [36].

The ADC values of metastatic lymph nodes were often found to be lower than those of benign lymph nodes [34-36,181,182]. However, some studies reported contradictory results. Several groups observed lower ADC values in benign than in malignant lymph nodes [183-185]. Two studies found no significant differences in ADC between benign and malignant lymph nodes [186,187]. In addition, the ADC values of benign and malignant nodes varied widely [188].

The ADC model assumes a Gaussian water displacement probability that is well known to be invalid in the heterogeneous environment of biological tissue. For measurements that include intermediate and low b -values, the IVIM model is often used to separate blood flow in vessels from water motion corresponding to true diffusion [72,73]. The IVIM model will probably enhance the accuracy of detection of malignant lymph nodes. Two recent studies have demonstrated that the IVIM model is useful for discrimination between metastatic and nonmetastatic lymph nodes in rectal cancer [189,190]. One study found significantly lower D (diffusion coefficient) and D^* (perfusion coefficient) in metastatic lymph nodes than those in nonmetastatic lymph nodes and no significant difference in f (perfusion fraction) [189]. However, the other study reported significantly higher D and f values of metastatic lymph nodes than those of normal lymph nodes and statistically lower D^* in metastatic lymph nodes [190]. Another study showed that the f in lymph nodes might be helpful for prediction of treatment response in head and neck carcinomas [191].

2.8. Summary

This chapter gave general background knowledge on DWI and then described three principal physical modes of diffusion (restricted, hindered and anisotropic) within tissue. Two complementary approaches for analysing the diffusion signal were discussed. One is the phenomenological model that provides empirical diffusion signal representation but lacks specificity. The other is the compartment model that is based on the assumption about tissue structure and can provide estimates of specific tissue features. However, compartment models are generally lacking for non-neural tissue. In this work, compartment models for four types of non-neural tissue including prostate, breast, spheroids and lymph nodes were investigated. The structure of these four types of tissue and modelling techniques that have been used for them were reviewed in this chapter.

Chapter 3 Information Based

Ranking of Models of Diffusion in

Prostate Tissue

3.1. Introduction

This chapter compares the theoretical information of single and multi-compartment models of DWI signal attenuation measured over an extended range of b -values and multiple diffusion times in prostate tissue. It aims to identify compartments that are necessary for accurately describing DWI signals in prostate tissue. Most previous DWI studies of prostate [39,114,115] made a comparison of phenomenological models that lack specificity and do not account for anisotropy and restricted diffusion (see Section 2.4.2, Chapter 2). A recently proposed three-component ‘VERDICT’ model [42] has demonstrated more reliable differentiation between prostate cancer and normal tissue than ADC and biexponential models. More importantly, the VERDICT model provides useful microstructural parameters such as cell size, intracellular, vascular, extracellular-extravascular volume fractions. However, previous DWI studies [42,43] that applied the VERDICT framework to prostate tissue in vivo used only isotropic compartment model. This study investigates the non-perfusion components of the VERDICT model by comparing information of eleven compartment models that include anisotropic components. To obtain high signal-to-noise ratio (SNR) measurements to inform the further development of clinical imaging methods this study used measurements performed on formalin fixed prostates.

3.2. Methods

3.2.1. Tissue Handling and Histopathology

Four prostates were collected with institutional ethics approval and written informed consent from patients, and they are: Prostate 1, age 59y, 47g, Gleason 4+4; Prostate 2, age 57y, 38g, Gleason 3+3; Prostate 3, 56y, 47g, Gleason 3+4; Prostate 4, healthy prostate, 35g. The intact prostate was sent to the pathology department immediately upon surgical resection and without immersion in a fixative solution. The organ was weighed and inked, and the seminal vesicles and any surgical clips were removed. The total time between resection and immersion in formalin was 6-8 hr. An experienced urologic pathologist confirmed that there was no significant tissue degradation due to delayed fixation of the specimens. The organ was immersed in 10% neutral buffered formalin for 24 hr and then immersed in normal saline for 24 hr to remove formalin. Fixed prostates were imaged for 24-48 hr before being returned to the pathology department for routine histology. All prostates were sectioned at 4-mm intervals in planes approximately parallel to imaging slices. All measurements were performed on fixed prostate tissue.

3.2.2. MRI Acquisition

Each organ was imaged suspended on a 5-mm saline-filled NMR tube inserted through the urethra and mounted in brackets in a plastic casing that maintained the tube axis parallel to and ~5 mm above the magnet z axis [192]. Imaging of fixed prostate tissue was performed at room temperature (22°C) on a 9.4T Bruker BioSpec Avance III 94/20 system (Bruker, Karlsruhe, Germany), which is equipped with a 72-mm internal diameter quadrature radiofrequency coil and BGA-12S HP gradients with maximum strength 660 mT/m and slew rate 4570 T/m/s. Imaging was performed transaxial to the urethra with the imaging planes oriented orthogonal to the 5-mm NMR tube.

All diffusion-weighted measurements were performed using a PGSE sequence and preceded by the acquisition of two reference ' $b = 0$ ' images. To maximize SNR, all measurements applied the minimum available TE ($\sim \Delta + 8$ ms). Intrinsic SNR was calculated from the ratio of the signal S , which is the mean signal intensity in a large intraprostatic region of interest (ROI) manually drawn inside a mid-organ slice of each prostate, relative to the noise level N , which is the standard deviation of the difference

between the ROI voxel values in the two reference ' $b = 0$ ' images. The DWI signal was sampled in three orthogonal directions. Separate DTI acquisitions were performed using six gradient directions. To test the generality of the model selection, each prostate was imaged with a different acquisition. Prostates 1 and 2 were imaged with nominal b -value range of 50-3000 s/mm² and voxel volume of 16 mm³ to emulate feasible clinical voxel volumes and b -values. Prostates 3 and 4 were scanned at high spatial resolution (voxel volume, 1.6 mm³ and 3.9 mm³, respectively) over an extended b -value range of 50-10354 s/mm². DWI and DTI acquisition parameters are detailed in Table 3.1.

Table 3.1 DWI acquisition parameters								
Prostate	1	2		3			4	
FOV (mm²)	64×50	64×50		50×50			45×45	
Matrix size	32×25	32×25		50×50			45×45	
Voxel size (mm³)	2×2×4	2×2×4		1×0.78×2			1.4×1.4×2	
SNR	225	232		291			240	
TR (ms)	2000	2000		2000			2000	
δ (ms)	5	5	10	5	5	10	5	10
Δ (ms)	10, 20, 40, 60, 80	10, 20, 40, 60, 80	40, 60, 80	10	20, 40	20, 40	20, 40, 80	20, 40, 80
TE (ms) (=Δ + 8 ms)	18, 28, 48, 68, 88	18, 28, 48, 68, 88	93, 93, 93	18	28, 48	33, 53	28, 48, 88	28, 48, 88
<i>b</i>-value (s/mm²) 6-directions	1500	1500		1500			1599	
<i>b</i>-value^a (s/mm²) 3-directions	50, 147, 275, 430, 607, 806, 1024, 1259, 1512, 1780, 2064, 2362, 2674, 3000	50, 147, 275, 430, 607, 806, 1024, 1259, 1512, 1780, 2064, 2362, 2674, 3000	50, 147, 275, 430, 607, 806, 1024, 1259, 1512, 1780, 2064, 2362, 2674, 3000	50, 178, 373, 632, 951, 1328, 1761, 2249, 2790, 3384, 4029, 4724, 5470, 5960	50, 178, 373, 632, 951, 1328, 1761, 2249, 2790, 3384, 4029, 4724, 5470, 5960	216, 511, 940, 1507, 2217, 3073, 4077, 5231, 6538	105, 279, 589, 1044, 1646, 2403, 3318, 4394, 5631, 7036, 8610, 10354	105, 279, 589, 1044, 1646, 2403, 3318, 4394, 5631, 7036, 8610, 10354
a) Nominal <i>b</i> -value. Effective <i>b</i> -values were used for model fitting.								

3.2.3. Model Description

Prostate tissue was modelled with combinations of up to three components described according to the taxonomy used for brain tissue DWI in [23]. There were five candidate components (see Table 2.1 in Section 2.3.2): 1) a Tensor which is a conventional DTI model providing two commonly used parameters FA and MD [193]; 2) a Zeppelin,

which is a cylindrically symmetric tensor and also provides FA and MD; 3) a Ball which is an isotropic tensor and equivalent to the ADC model; 4) a Sphere describing water molecules diffusing inside an impermeable pore with a non-zero radius; and 5) a Stick assuming water diffusion in an idealised cylinder with zero radius. In total, eleven models were considered (Table 3.2)

Table 3.2 Fitted models			
Name	Components from Table 2.1 in Section 2.3.2	Fitted parameters ^a	No. parameters
Ball (ADC)	Ball	D	1
Bi-ball	Ball + Ball	$f_1 D_1 D_2$	3
Ball-sphere	Ball + Sphere	$f_1 D_1 R D_2$	4
DTI	Tensor	$D_{ } D_{\perp 1} D_{\perp 2} \theta \phi \alpha$	6
Ball-zeppelin	Ball + Zeppelin	$f_1 D_{ } D_{\perp} \theta \phi D$	6
Zeppelin-sphere	Zeppelin + Sphere	$f_1 D R D_{ } D_{\perp} \theta \phi$	7
Ball-tensor	Ball + Tensor	$f_1 D_{ } D_{\perp 1} D_{\perp 2} \theta \phi \alpha D$	8
Bi-ball-zeppelin	Ball + Ball + Zeppelin	$f_1 f_2 D_1 D_2 D_{ } D_{\perp} \theta \phi$	8
Bi-zeppelin	Zeppelin + Zeppelin	$f_1 D_{ 1} D_{\perp 1} \theta_1 \phi_1 D_{ 2} D_{\perp 2}$ $\theta_2 \phi_2$	9
Tensor-sphere	Tensor + Sphere	$f_1 D_{ } D_{\perp 1} D_{\perp 2} \theta \phi \alpha D R$	9
Ball-stick-sphere	Ball + Stick + Sphere	$f_1 f_2 D_1 D_2 \theta \phi D_3 R$	8

a) Signal normalized before fitting ($S_0 = 1$). Sum of signal fractions $f_1 + f_2 + f_n = 1$. D is the diffusivity, $D_{||}$ is tensor parallel diffusivity, and D_{\perp} is tensor perpendicular diffusivity. θ , ϕ and α are tensor angles. R is sphere radius.

3.2.4. Model Fitting Method

This study used rich data sets with a wide range of b -values and diffusion times to ensure stable fitting [41]. As the measured diffusivity of restricted diffusion is diffusion

time dependent (see Section 2.2.1 Chapter 1), the 3-direction data with multiple diffusion times were acquired to enable the estimation of a restriction radius. The 6-direction data with single b -value and single δ/Δ value were acquired to enable the fitting of anisotropic components. The combination of 3- and 6-direction data were fitted to each model using the Levenberg-Marquardt minimization algorithm available in the open source Camino toolkit [194]. The signals were normalized to the ‘ $b=0$ ’ signal before fitting to minimize T_2 effects [41]. Model fitting was based on minimization of an objective function that uses an offset-Gaussian noise model to account for the inherent Rician distributed noise in the magnitude MRI data [41]. The objective function is the sum of squared errors:

$$SSE = \sum_{n=1}^M (S_n(\delta, \Delta, G) - \widetilde{S}_n(\delta, \Delta, G))^2 \quad [3.1]$$

where M is the number of measurements, $S_n(\delta, \Delta, G)$ is the signal predicted by the model and $\widetilde{S}_n(\delta, \Delta, G)$ is the signal of the n th measurement. Firstly, the evolution of the objective function over 1000 runs was monitored to assess convergence to the best parameter estimates (with lowest objective function). This test shows that the number of runs that is required to obtain the best solution in each model with probability > 0.99 is less than 100. Subsequently, for each voxel, the best-fit parameters were chosen after 100 perturbations of the starting point to avoid local minima. The range of model parameters was limited to biophysical meaningful values. For the sphere component, radius R was constrained so that $0.1 \leq R \leq 20 \mu\text{m}$. All component signal fractions were constrained to be in $[0, 1]$ and sum to 1. Diffusivities of all components were constrained to the range of $0 \leq D \leq 2.1 \mu\text{m}^2/\text{ms}$ according to the 22°C sample temperature [195].

3.2.5. Information Based Model Ranking

The Akaike Information Criterion (AIC) provides an estimate of the expected, relative distance between the candidate model and the unknown true system that generates the observed data, and does not require arbitrary selection of cutoffs for hypothesis testing. AIC is useful in selecting the best model that is estimated to be closest to the unknown reality. Lower AIC indicates higher model information, equivalent to less information loss, and predicts superior model prediction performance. In the case of DWI of tissue,

the general definition of the AIC on p. 62 of Burnham and Anderson [196] leads to the expression:

$$AIC = \left(\frac{SSE}{\sigma^2} \right) + 2p \quad [3.2]$$

where SSE is the sum of squared errors returned by the fit algorithm (see Eq. [3.1]), σ is the noise standard deviation estimated from a pair of reference images, and p is the number of model parameters. AIC is the trade-off between bias and variance. If the number of measurements, n is comparable to the number of model parameters, p , the derived second-order variant of AIC called AICc is recommended:

$$AICc = AIC + \frac{2p(p+1)}{(n-p-1)} \quad [3.3]$$

A model is used for inference about the empirical data that is generated from the unknown full reality [196]. In this sense, the data helps determine the proper complexity of the model and what effects are justified. The larger data sets tend to support more complex models as further effects could probably be found, and reduced data sets possibly favour simpler models. It is worth noting that model selection informs us of inferences that the observed data support, not what full reality might be. AIC cannot be used to compare models across different data sets as the inference is conditional on the given data set. Furthermore, data sometimes do not support only one model as best. Several models would serve almost equally well for the analysis of the empirical data. The inability to select a single best model is not a defect of AIC. That is, the data are ambivalent concerning some effect or parametrization or structure [196].

Previous prostate ex vivo studies have validated AIC as a method of comparing information of models using a leave-one-out test of model prediction error [39,40]. Differences between model ranking AIC scores were assessed via a Mann-Whitney U-Test performed in Matlab (Mathworks, Natick, MA, USA).

3.3. Results

This section presents the evaluation and assessment of the models in terms of information, parameter estimates, quality of model fit and anisotropy.

3.3.1. AIC-based Model Ranking

Figure 3.1 presents positional variation in the ranking of the models according to AIC and displays the anatomical distribution of the highest ranked models in a mid-organ transverse slice of each organ. Figure 3.2 shows the rank variations of each model. Box and whiskers plots of the variation in AIC scores within and between models for each prostate are shown in Figure 3.3. Log(AIC) data are presented in Figure 3.3 because they produced a normal distribution of the skewed raw AIC scores.

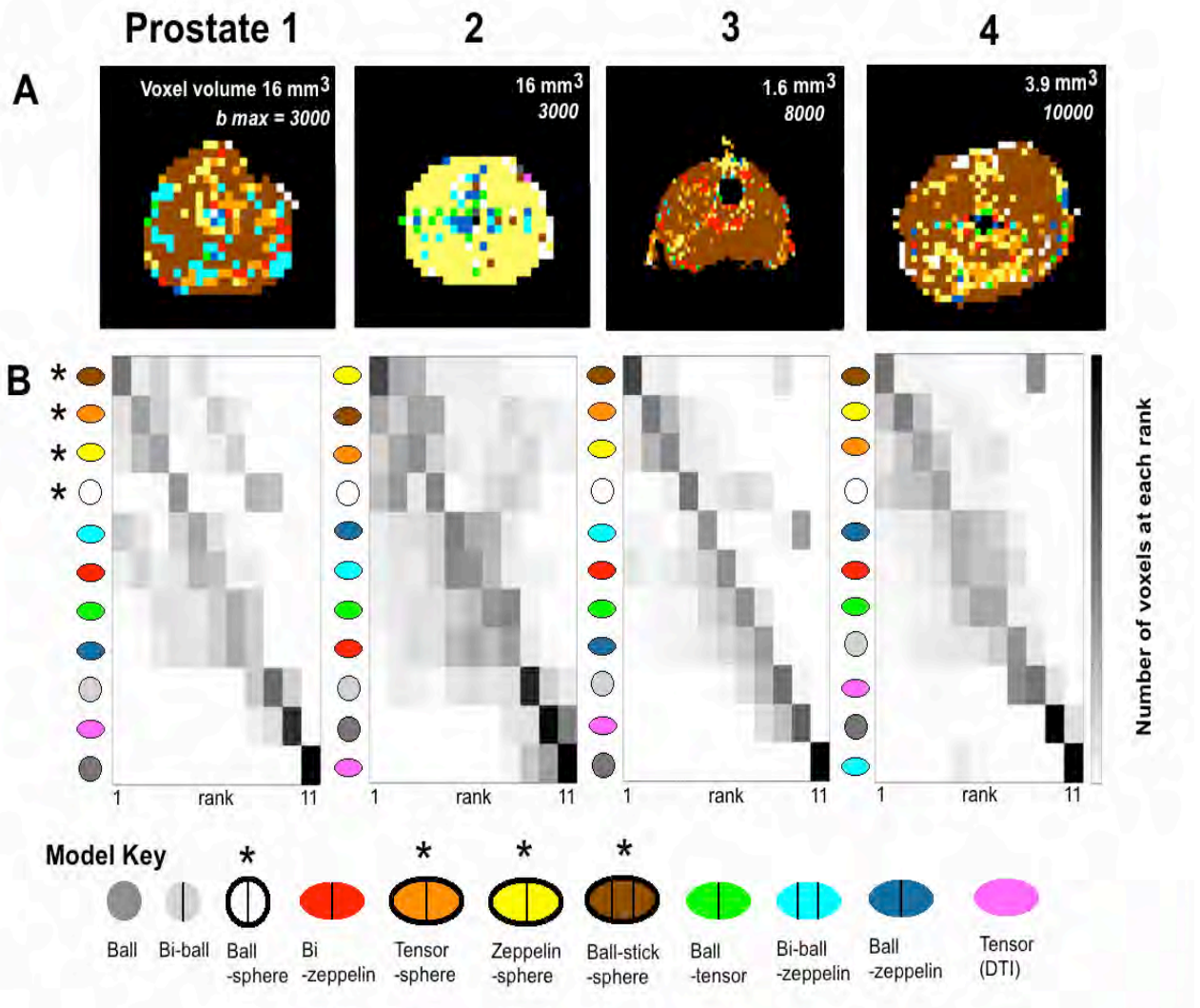


Figure 3.1 Variation in AIC-based model rankings for four prostates.

(A) Anatomical distribution of the highest ranked model in a mid-organ slice from each prostate (see Figure. 3.2 for pathology maps of these slices). Voxel color indicates model according to the Model Key. The Ball-stick-sphere (brown), Zeppelin-sphere (yellow) and Tensorsphere (orange) models ranked highest in most voxels in all prostates. (B) Positional variations in AIC-based model ranking. The gray scale indicates the number of times each model ranked at each position. The models were put in order according to the trends assessed subjectively [see Fig. 3.3 for a statistical analysis of AIC ranks]. Data from 558 voxels from slices 5 and 6 in Prostate 1, 504 voxels from slices 5 and 6 in Prostate 2, 1278 voxels from slices 7–9 in Prostate 3, and 2041 voxels from slices 3–6 in Prostate 4. Model Key: the four restricted models are shown with a bold black border and marked with an asterisk; anisotropic models are shown as ellipses; vertical lines within model symbols indicate the number of components.

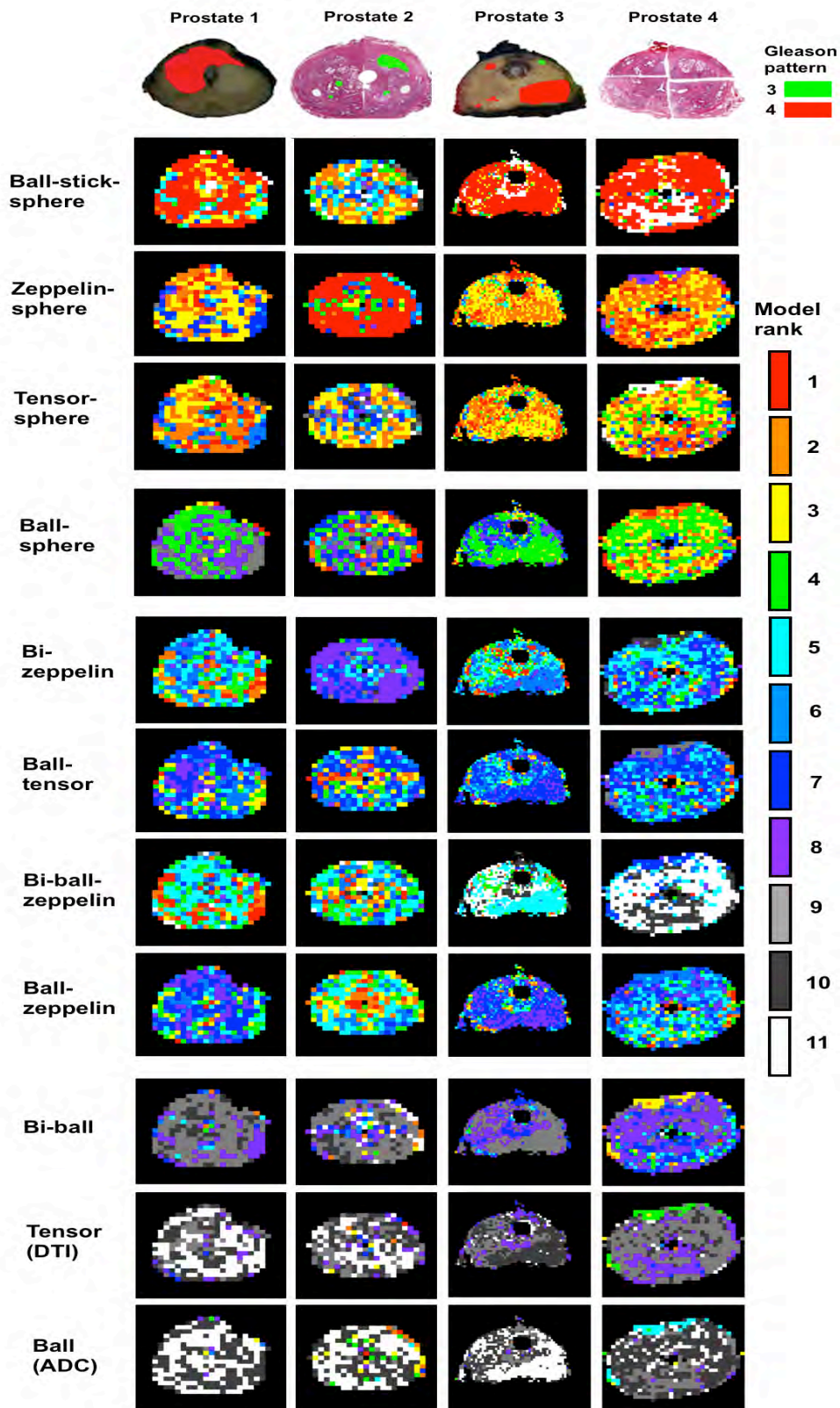


Figure 3.2 Rank variations of individual models in four prostates.

Slice positions as for Figures 3.1 and 3.5. Voxel color indicates model rank and models are grouped according to predominant rank.

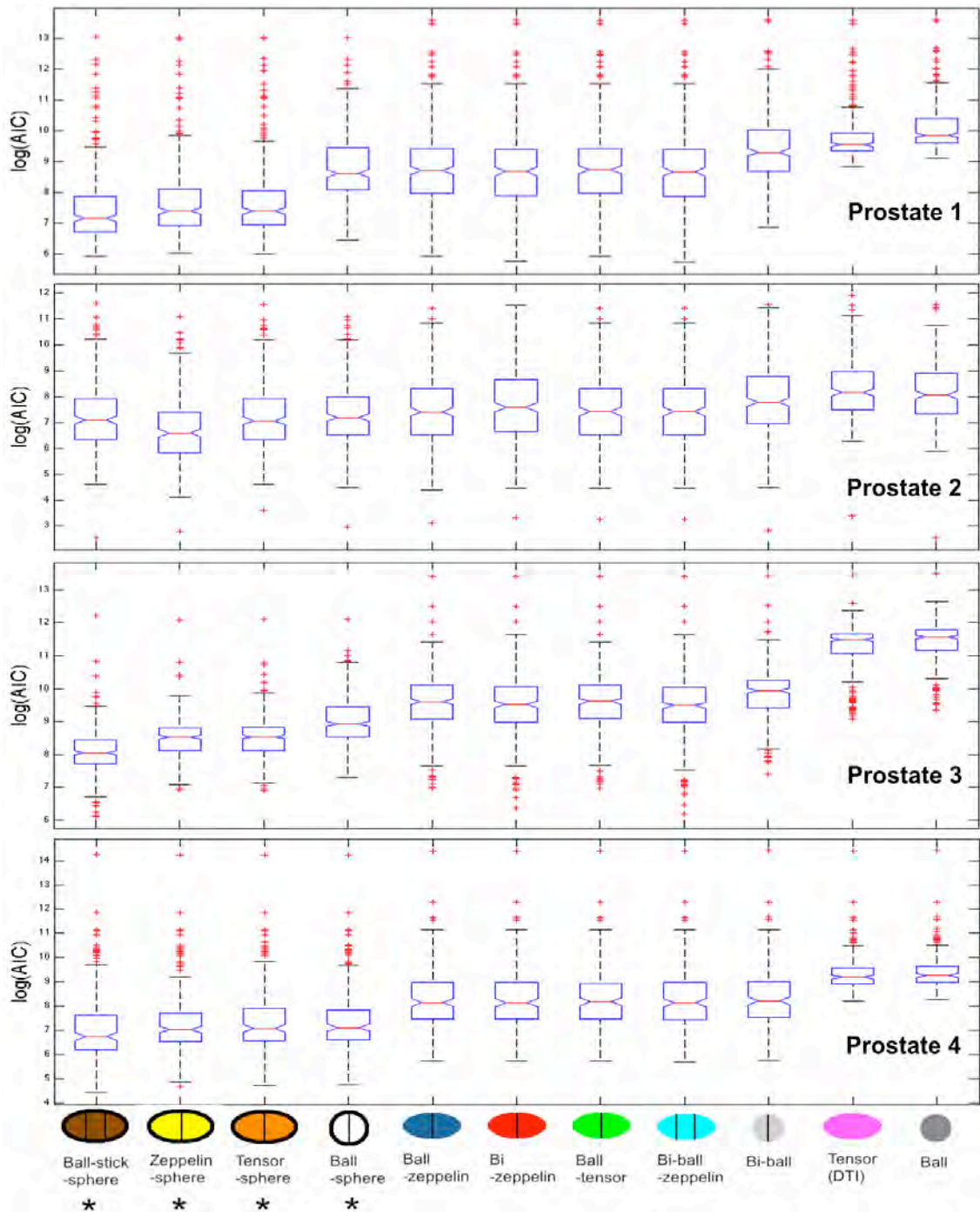


Figure 3.3 Box and whisker plots of $\log(\text{AIC})$.

Four restricted models are marked with a black asterisk. For each blue box, the central red mark is the median and the top and bottom edges of the box are the 25th and 75th percentiles. The whiskers extend to the most extreme data points. Outliers are plotted individually in red. Distributions were normal after the log transformation. Data from 558 voxels from slices 5 and 6 in Prostate 1, 504 voxels from slices 5 and 6 in Prostate 2, 1278 voxels from slices 7–9 in Prostate 3, and 2041 voxels from slices 3–6 in Prostate 4. Results for Mann–Whitney U-test are presented in Appendix.

In all prostates, the top three models are the Ball-stick-sphere, Zeppelin-sphere, and Tensor-sphere models in the majority of voxels. No distinct variation of ranking according to prostate zonal anatomy was observed. The isotropic restricted Ball-sphere model ranked close to three multi-component restricted and anisotropic models. The single-component Ball/ADC and DTI models ranked low in four prostates. Multi-component models that included anisotropic components generally contained more information than isotropic models, and models that account for diffusion restriction usually had higher information than unrestricted models. In addition, model ranking trends were largely independent of voxel volume, maximum b -value, maximum diffusion time, and whether or not two different diffusion encoding pulse lengths (δ) were used (Table 3.1).

Table A.1 in Appendix A provides results of a Mann-Whitney U-test for significant differences in AIC scores between models. Three distinct groups of models emerge: 1) Ball-stick-sphere, Zeppelin-sphere, (Tensor-sphere); 2) Ball-zeppelin, (Ball-sphere), (Bi-ball-zeppelin), Bi-zeppelin, Ball-tensor; 3) Ball, (Bi-ball), DTI. The brackets indicate models that may appear in the other group in some prostates. The models in Group 1 have significantly lower AIC scores than those in Group 2 and 3. The results of this statistical analysis are consistent with the qualitative data presented in Figures 3.1 and 3.2.

Taken together, these results demonstrate that multi-component anisotropic and restricted (Ball-stick-sphere, Zeppelin-sphere and Tensor-sphere) models extract more information from rich data, which are acquired with a wide range of multiple b -values and multiple diffusion times, than single-component models and multi-component models that do not account for diffusion restriction.

3.3.2. Synthesis and Fitting

Figure 3.4 illustrates the fit of eleven models to the summed data from a homogeneously anisotropic four-voxel ROI in the normal TZ tissue. Although FA in these four voxels was low (0.17-0.20), the model ranking shows that the top seven models all include at least one anisotropic component. These seven multi-component anisotropic models provide better fits to the measurement data than multi-component isotropic models and single-component models. Nonetheless, the results also show that

not even the most highly parameterized models provide an exact description of the measurement data.

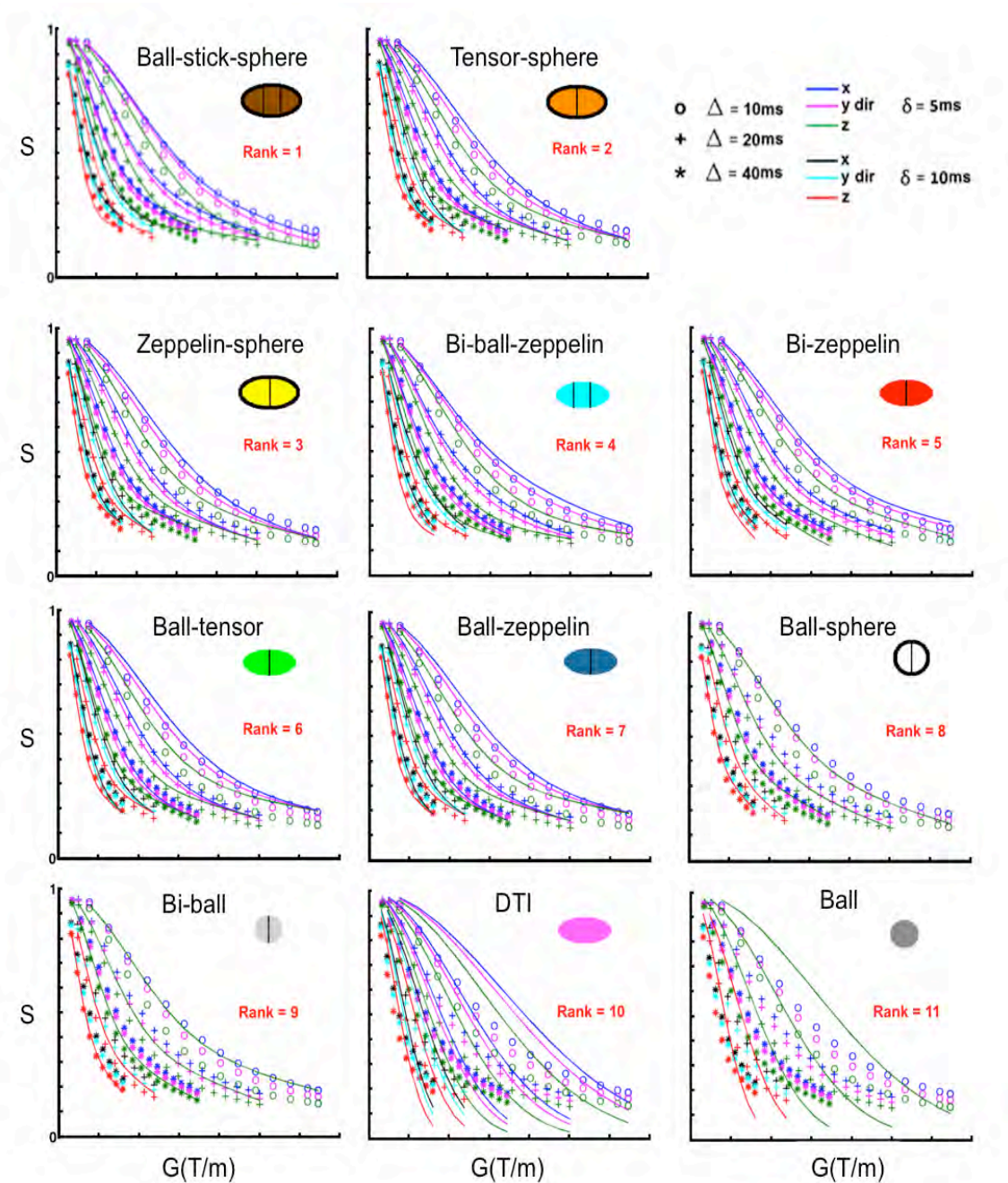


Figure 3.4 Representative model fit data.

The symbols represent measurement data and the lines show the measurements predicted by the models. Normalized signal S is plotted for all values of Δ and δ as a function of gradient strength $|G|$ for three directions. The model rank for this specific data set is presented. The data are the mean of four adjacent voxels in the TZ of Prostate 3 with similar primary eigenvector orientation.

3.3.3. Parametric Maps

Figure 3.5 presents Zeppelin-sphere model parameter maps for all four prostates with mapped pathology in approximately the same slice position. The map for diffusivity of the Ball model is also presented for reference. Very similar parameter maps were obtained for the Tensor-sphere and Ball-stick-sphere models (Figures A.1, A.2 in Appendix A).

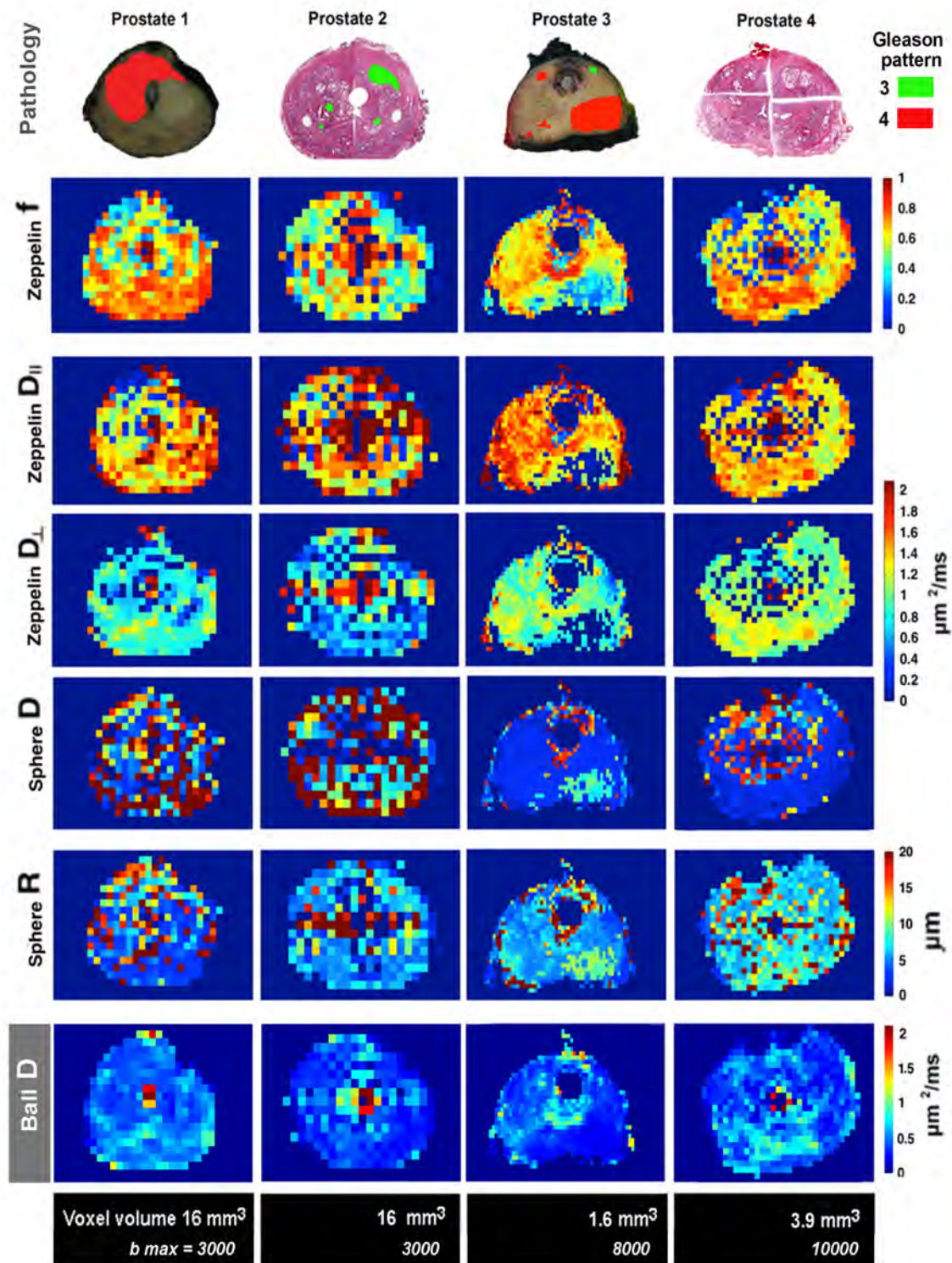


Figure 3.5 Zeppelin-sphere model parameter maps.

Slice positions as for Figures 3.1 and 3.2. Parameter maps for the Tensor-sphere and Ball-stick-sphere models for the same slices are provided in Figures A.1 and A.2. For reference, the Ball diffusivity maps are included.

Figure 3.6 shows the Zeppelin-sphere model parameter histograms. The histograms are presented as D or R versus the component signal fraction. The diffusivities for the two components ('zeppelin' and 'sphere') are less than the self-diffusion coefficient for water at 22°C [197] in the majority of voxels, and the range of the estimated sphere radius is in agreement with typical cell diameters, indicating that Zeppelin-sphere model is biophysically plausible. Simple histograms of D and R are provided in Figure A.3 (see Appendix A).

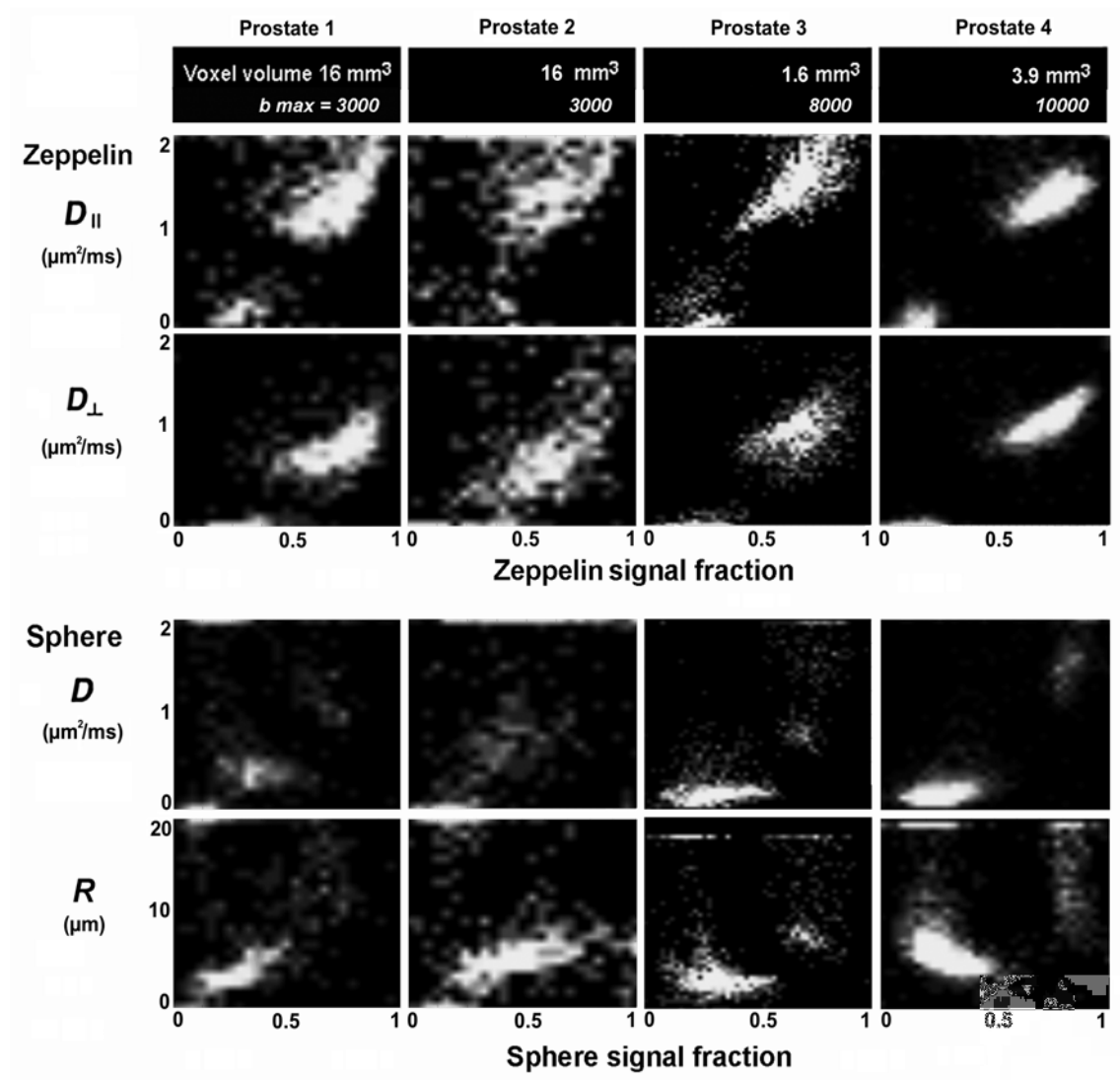


Figure 3.6 Two-way parameter histograms for the Zeppelin-sphere model.

The pixel brightness is proportional to the voxel count. The Zeppelin-sphere model returned parameters that are less than the defined limits in the majority of voxels, indicating that the model was biophysically plausible.

3.3.4. Anisotropy

Figure 3.7 compares MD and FA of the anisotropic component in the Tensor-sphere and Zeppelin-sphere models with MD and FA derived from the conventional DTI model. In this example (a central slice from Prostate 3) both FA and MD of the tensor and zeppelin components show clear differences between Gleason pattern 4 cancer and normal tissue (see Figure 3.2 for the pathology map of this slice) that are not detected by the single component DTI model.

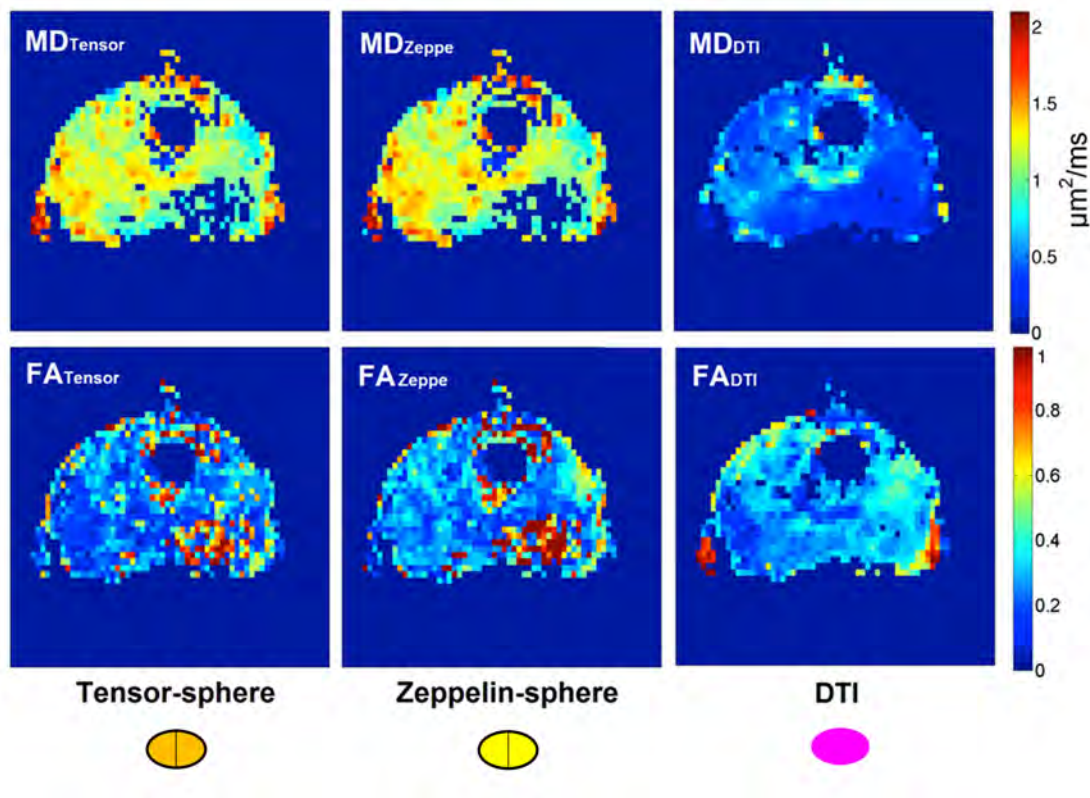


Figure 3.7 MD and FA maps from Tensor-sphere, Zeppelin-sphere, and DTI models for Prostate 3.

Slice position as for Figures 3.1 and 3.2.

3.4. Discussion

One previous study of prostate ex vivo [39] compared four phenomenological (ADC, biexponential, kurtosis and stretched) models in terms of information using AIC. They found that the biexponential model had highest information of these four models. The conventional biexponential model assumes that there are two distinct ‘slow’ and ‘fast’

water pools and each exhibits Gaussian behaviour. Another study of prostate ex vivo [40] applied the stretched exponential model to the individual components of this conventional biexponential model and found these two distinct water pools exhibited non-Gaussian diffusion dynamics. Taken together, these results suggest the presence of two distinct diffusion (non-perfusion) environments in prostate tissue. These two diffusion environments have been modelled as an isotropic restricted water pool combined with an isotropic unrestricted water pool in an in vivo study utilizing the VERDICT model [42]. However, none of these studies have modelled both diffusion anisotropy and restricted diffusion in prostate tissue. This study provides further information about the diffusion environments in prostate tissue by comparing information of eleven compartment models including anisotropic and restricted components.

The results show that multi-component models, including anisotropic and restricted components, have higher information than single-component (ADC and DTI) models and multi-component unrestricted models. The superior performance of multi-component anisotropic and restricted models suggests that both anisotropic and restricted components are required to accurately describe DWI signals measured over multiple b -values and multiple diffusion times. At all voxel volumes (1.6, 3.9, and 16 mm³) tested in this study, multi-component anisotropic and restricted models consistently rank highest, indicating that the two water pools identified by the anisotropic and restricted components exist on a microscopic scale.

The low ranking of ADC, DTI and Bi-ball/biexponential models found in this study is consistent with previous prostate ex vivo studies [39,40]. It is worth noting that DWI is the key component of prostate mpMRI exam and ADC is the mainstay approach in clinical DWI studies. The results in this study have demonstrated that multi-component anisotropic and restricted models extract more information from measurements with multiple b -values and multiple diffusion times than the simple ADC model. These results suggest that implementation of more sophisticated models, such as the VERDICT model, and appropriate DWI acquisition methods might improve the DWI performance in prostate cancer assessment significantly.

Recently, a three-component VERDICT model has been used to characterize prostate tissue in vivo by providing estimates of specific tissue properties including cell size, and

intracellular and vascular volume fractions [42]. The VERDICT model describes DWI signals as the sum of three signals (S_1 , S_2 , S_3) arising from separate populations of water in three distinct structural environments. S_1 comes from a water pool inside the cells, S_2 from a water pool in blood vessels, and S_3 from a water pool outside cells and blood vessels. The VERDICT model for prostate tissue uses an isotropic sphere to model S_1 , AstroSticks (cylinders with uniformly distributed orientations and zero diameter) [23] to model S_2 , and an isotropic diffusion tensor to model S_3 . The results show that the VERDICT model provides reliable discrimination of malignant and benign human prostate tissue and returns parameter estimates in agreement with histology. However, the *in vivo* VERDICT study did not model diffusion anisotropy in prostate tissue. The *ex vivo* study presented here addressed this limitation by including anisotropic components.

Another important difference between this *ex vivo* study and the *in vivo* VERDICT study is the number of estimated parameters. The VERDICT model was applied to prostate tissue at clinical setting and the measurement data had a median SNR of 14 that is lower than that measured in this *ex vivo* study. To avoid overfitting the relative noisy *in vivo* data, the diffusion and perfusion coefficients of the VERDICT model were fixed to values that minimize fitting error (an objective function) averaged over all voxels. As a result, the VERDICT model has three free parameters: intracellular volume fraction, extracellular-extravascular volume fraction, and sphere radius.

In contrast, the high SNR measurements with a wide range of b -values and diffusion times acquired in this study enable reliable fitting of highly parameterized models with fewer constraints on parameters. So all diffusion coefficients of the eleven models tested were allowed to float within the biophysical limits. Multi-component anisotropic and restricted models returned values of parameters (diffusivities, sphere radius, and signal fractions) that were less than the defined limits in the majority of voxels, suggesting that they were biophysically plausible models. It is noteworthy that the peak value of Zeppelin parallel diffusivity (Figure 3.6) is $\sim 1.4 \mu\text{m}^2/\text{ms}$ corresponding to $2 \mu\text{m}^2/\text{ms}$ at human body temperature. The value of $2 \mu\text{m}^2/\text{ms}$ is consistent with the fixed diffusivity value used for intracellular and extracellular-extravascular compartments in the *in vivo* VERDICT study. In addition, the results show that multi-component anisotropic and restricted models with fewer constraints rank higher than single-

component models and multi-component unrestricted models, indicating that the parameters of less constrained models contain information about the tissue structure.

This study shows that multi-component restricted models rank higher than the models that did not account for diffusion restriction in the majority of voxels. This finding supports the *in vivo* VERDICT study, which uses a restricted component to describe the intracellular diffusion environment. Moreover, this result suggests the importance of inclusion of a restricted component for modeling water diffusion in prostate tissue.

DTI-based measurements of FA in prostate tissue have produced inconsistent results [104,105,108-111]. Possible FA-affecting differences between the reported *in vivo* studies include voxel volume, *b*-values, noise and diffusion time. A recent study of diffusion anisotropy in prostate tissue reported wide inter-prostate FA variations and a strong voxel volume dependence (FA decreases with the increasing voxel volume) [56]. A diffusion microimaging study of prostate tissue *ex vivo* demonstrated significantly higher anisotropy in the fibromuscular stroma than the epithelium and lumen space [55]. At typical clinical spatial resolutions (voxel size 4–16 mm³), it is likely that fibromuscular stroma, epithelium and lumen space are present within a voxel. Another possible reason for inconsistent FA values is that significant sub-voxel diffusion anisotropy of the stroma may be masked by the presence of a substantial pool of isotropically diffusing water in epithelium and lumen space when FA is assessed with a simple single-component DTI model. FA calculated from the anisotropic component of the Tensor-sphere and Zeppelin-sphere models were higher than that derived from a conventional DTI model (Figure 3.7), indicating the presence of this masking effect. The diagnostic value of this relatively high sensitive anisotropy detection method needs further investigation.

This study compared information of eleven models using AIC. Although AIC is useful in selecting the model which extracts the most information from the given set of measurement data, it is possible that the measurement data do not contain information that can discriminate between different tissue structures including normal tissue and prostate cancer. As noted in Section 1.2 Chapter 1, it is important to define an imaging protocol that can acquire appropriate information, particularly information that has diagnostic value. To improve the clinical performance of DWI, optimization of both DWI acquisition methods and signal models is needed. This study did not compare

models in terms of cancer detection performance due to the small number of patients. With regard to the assessment of model performance in cancer detection, most of previous prostate DWI studies correlated the individual model parameter with tissue pathology. It has been suggested that the information of models is distributed among model parameters [39]. Thus it is more appropriate to use combinations of model parameters (that include all information) for evaluating the efficacy of models for cancer detection in a large patient population.

3.4.1. Limitation

This study is based on diffusion imaging of formalin-fixed prostate tissue. There are several advantages of ex vivo imaging over in vivo imaging: (1) it can acquire high SNR and high spatial resolution measurement data; (2) it allows long scan time; (3) it is relatively inexpensive; (4) it is free from organ movement, perfusion, and susceptibility which are present in in vivo imaging. However, the absence of perfusion may cause a decrease in the volume of extracellular-extravascular water. This decrease would have an effect on signal fractions of each compartment.

As high spatial resolution measurements require long imaging time, all four prostates were stabilized by formalin fixation. A previous prostate DWI study reported that formalin fixation caused a significant decrease in the measured diffusivity [113,192]. Nevertheless, it has been suggested that the formalin fixation is unlikely to affect the model ranking [39,198].

In this study, DWI signals were normalized to the ' $b = 0$ ' signal before model fitting to minimize T_2 effects. Previous prostate studies [199,200] demonstrated that prostatic T_2 decay was biexponential, indicating the presence of two water pools with distinct T_2 values. To date, no studies have investigated whether different T_2 water pools in prostate tissue correspond to two distinct water pools identified in diffusion analyses. A recent study extended three-component models of diffusion in white matter to account for T_2 effects [24]. Future work will investigate compartment models that incorporate T_2 effects (probably in a similar way to [24]).

The multi-component models tested in this study assumed no water exchange between compartments. The influence of cell membrane permeability on diffusion measurements in prostate tissue has yet to be investigated. Previous experiments on cultured cells

demonstrated that cell membrane permeability could have a significant impact on the model parameters depending on the applied diffusion time [62,201]. Stanisiz et al. [70] constructed a three-compartment model of diffusion in white matter with exchange between compartments by using the modified Bloch equations proposed by Karger et al. [202]. Future work will explore the incorporation of compartmental exchange into compartment models of diffusion in prostate tissue.

As there exist differences (in temperature, perfusion, tissue fixation, and available diffusion times) between ex vivo imaging and in vivo imaging, the findings presented here cannot be directly related to clinical prostate imaging. Nonetheless, the information on diffusion environments in prostate tissue obtained in this high field ex vivo study, which acquires high SNR measurement data with a wide range of b -values and diffusion times, can be used to guide future development of clinical imaging methods.

3.5. Conclusions

This study provides further information on diffusion environments in prostate tissue. The results show that multi-component anisotropic and restricted models extract more information from the multi- b and multi- Δ measurement data than single-component (ADC and DTI) models and multi-component unrestricted models. The rankings of models are largely independent of maximum b -value, maximum diffusion time, and voxel volume over the range tested in this study. For further development of promising VERDICT model, this study suggests that it is important to model both diffusion anisotropy and diffusion restriction in prostate tissue.

Chapter 4 Predicting the Impact of Diffusion Time on Mean Diffusivity and Fractional Anisotropy in Fixed Prostate Tissue

4.1. Introduction

Diffusion time is an important parameter that determines the spatial scale of tissue structure probed by DWI. However, for imaging methods, DWI studies generally consider optimum b -values and rarely report diffusion time. The b -value (see Eq. [2.6] in Chapter 2 Section 2.1.2) depends on diffusion time (Δ), gradient duration (δ) and gradient strength (G). In practice, the selected Δ , δ , and G values vary between MRI scanners and depend on scanner software, available maximum gradient strength, and selected b -values. It is likely that the same b -value is produced from different combinations of Δ , δ , and G generated by different scanners. DTI model provides two useful parameters: MD and FA. MD values have been shown to be lower in prostate cancer than in normal prostate [104-107]. However, the reported FA values in prostate tissue in vivo vary widely [104,109-111]. It has been suggested that relative low SNR causes artificially high FA estimates [111,112]. This chapter aims to investigate the influence of diffusion time and noise on MD and FA in fixed prostate tissue. Measured MD and FA are derived from the inevitably noisy DTI data. To assess the actual impact of diffusion time (separate from the noise effect), this study uses an anisotropic and restricted model to generate ‘noise-free’ synthesized DTI data, which are used for calculating predicted MD and FA. Chapter 3 has shown that the highest three AIC-ranked models in four prostates are Ball-stick-sphere, Zeppelin-sphere and Tensor-sphere, all of which include both anisotropic and restricted components. Zeppelin-

sphere model that is less parameterized than the other two models is selected for predicting the impact of diffusion time.

4.2. Methods

4.2.1. Tissue Handling

Three radical prostatectomy specimens were collected with institutional ethics approval and written informed consent from patients. Specimens were fixed in 10% neutral buffered formalin for 32 h. Then the fixed prostate was washed in normal saline for 24 h to remove formalin [56]. Each specimen was imaged suspended on a 5-mm saline-filled NMR tube inserted through the urethra and mounted in brackets in a plastic casing that maintained the tube axis parallel to and approximately 5mm above the magnet z axis [192]. The prostate was wrapped in parafilm to minimize dehydration during imaging. After imaging, the prostate was returned to the pathology department for routine histology.

4.2.2. MRI Acquisition

Imaging was performed at room temperature (22 °C) on a 9.4T Bruker (Karlsruhe, Germany) BioSpec Avance III 94/20 system equipped with a 72-mm internal diameter quadrature radiofrequency coil and BGA-12S HP gradients with maximum strength 660 mT/m and slew rate 4570 T/m/s. Imaging was performed transaxial to the urethra with the imaging planes oriented orthogonal to the 5-mm NMR tube.

All diffusion-weighted measurements were performed using a PGSE sequence and preceded by the acquisition of two reference ' $b = 0$ ' images. To investigate the effect of diffusion time on MD and FA, DTI acquisitions used a six-direction scheme with nominal $b = 800, 1600 \text{ s/mm}^2$ and a wide range of diffusion times (10 - 120 ms). Three-direction DWI data acquired with eight b values (100 - 3000 s/mm^2) and four diffusion times ($\Delta = 10, 20, 40, 80 \text{ ms}$) were combined with $\Delta = 20 \text{ ms}$ DTI data to fit the Zeppelin-sphere model. To maximize SNR, all measurements applied the minimum available TE ($\sim \Delta + 8 \text{ ms}$). If measurements were performed with a fixed TE = 108 ms or 128 ms, this would lead to overall low SNR and introduce more artifacts. DTI and DWI acquisition parameters including SNR estimates are detailed in Tables 4.1 and 4.2

respectively. All SNRs were calculated from the ratio of the signal S relative to the noise level N . S is the mean signal intensity in a large region of interest (ROI) manually drawn inside a mid-organ slice of each prostate. N is the standard deviation of the difference between the ROI voxel values in the two ' $b = 0$ ' reference images. The signal S for SNR at $b = 800, 1600 \text{ s/mm}^2$, was defined as the mean ROI voxel value taken over all six gradient directions.

Table 4.1 6-direction DTI acquisition parameters										
Prostate	FOV (matrix)	Voxel size (mm)	TR (ms)	b-value^a (s/mm^2)	Δ^b (ms)	TE (ms)	AV	SNR $b=0$	SNR $b=800$	SNR $b=1600$
1	50×50 mm (40×40)	1.25×1.25×2	2200	800 1600	10	18	2	190	95	62
					20	28	2	137	74	50
					30	38	2	119	66	45
					40	48	2	105	59	40
					50	58	2	55	31	21
					60	68	4	89	50	35
					70	78	4	47	27	19
					80	88	8	57	32	22
					90	98	8	50	28	19
					100	108	8	30	16	12
2	50×50 mm (40×40)	1.25×1.25×2	2200	800 1600	10	18	2	311	153	97
					20	28	2	211	113	75
					30	38	2	173	95	64
					40	48	2	103	57	39
					50	58	2	78	44	30
					60	68	4	105	59	41
					70	78	4	75	42	29
					80	88	4	63	35	25
					90	98	4	38	21	15
					100	108	4	28	16	11
					120	128	4	18	10	7
					3	60×60 mm	1.5×1.5×2	2600	800	10
1600	20	28	2	165					82	53

	(40×40)				30	38	2	150	76	49
					40	48	2	140	71	46
					50	58	2	109	55	36
					60	68	4	147	74	48
					70	78	4	74	37	24
					80	88	8	137	68	44
					90	98	8	101	50	33
					100	108	8	77	37	24

a) Nominal b -value. Effective b -values were used for model fitting.

b) $\delta = 5$ ms for all measurements.

Table 4.2 3-direction DWI acquisition parameters

Prostate	FOV (matrix)	Voxel size (mm)	TR (ms)	b -value ^a (s/mm ²)	Δ ^b (ms)	TE (ms)	AV	SNR $b = 0$
1	50×50 mm (40×40)	1.25×1.25×2	2000	100, 311,	10	18	1	133
				603, 965,	20	28	1	123
				1391, 1873,	40	48	1	83
				2411, 3000	80	88	2	29
2	50×50 mm (64×64)	0.78×0.78×2	2200	100, 311,	10	18	4	448
				603, 965,	20	28	4	270
				1391, 1873,	40	48	4	164
				2411, 3000	80	88	4	56
3	60×60 mm (40×40)	1.5×1.5×2	2600	100, 311,	10	18	1	152
				603, 965,	20	28	1	134
				1391, 1873,	40	48	1	90
				2411, 3000	80	88	1	44

a) Nominal b -value. Effective b -values were used for model fitting.

b) $\delta = 5$ ms for all measurements.

4.2.3. Model Description

In Chapter 3, the Zeppelin-sphere, Tensor-sphere, and Ball-stick-sphere models incorporating both anisotropic hindered and isotropic restricted components have been demonstrated to have highest information for DWI measurements in prostate tissue. This study used the Zeppelin-sphere model, which has fewer free parameters than the other two models, to generate noise-free synthesized DTI data at each diffusion time. The Zeppelin-sphere model was described in detail in Chapter 3, Table 3.2.

4.2.4. Model Fitting

Figure 4.1 illustrates the process for deriving FA and MD from both measured DTI data and synthetic DTI data. To calculate measured FA and MD, the DTI model was fitted to a single b -value 6-direction DTI data set (Table 4.1) at each measured diffusion time. The Zeppelin-sphere model was fitted to the combined 3-direction data and $\Delta = 20$ ms 6-direction data. The purpose of using only the $\Delta = 20$ ms DTI data to define the zeppelin parameters was to maximize the independence of the measured and predicted MD and FA data. The zeppelin component also provides FA and MD. The fitted Zeppelin-sphere model parameters were used to synthesize noise-free 6-direction DTI data at $b = 800, 1600,$ and 3000 s/mm² for each diffusion time. The inclusion of $b = 3000$ s/mm² prediction is to investigate the diffusion time dependence at ultra high b -value. The DTI model was then fitted to the synthetic DTI data to obtain predicted FA and MD.

DTI and Zeppelin-sphere model fitting used the Levenberg-Marquardt algorithm in the open source Camino toolkit [194]. All data were normalized to the ' $b = 0$ ' signal to minimize any T_2 effects. The Zeppelin-sphere model parameters were constrained within biologically plausible limits. The sphere radius R was constrained to the range $0.1 - 20$ μm . Diffusivities were constrained so that $0 \leq D \leq 2.1$ $\mu\text{m}^2/\text{ms}$. Two component signal fractions were constrained to be in $[0, 1]$. The correlation between measured MD/FA and predicted MD/FA was accessed via the Pearson rank metric performed in Matlab (Mathworks, Natick, USA).

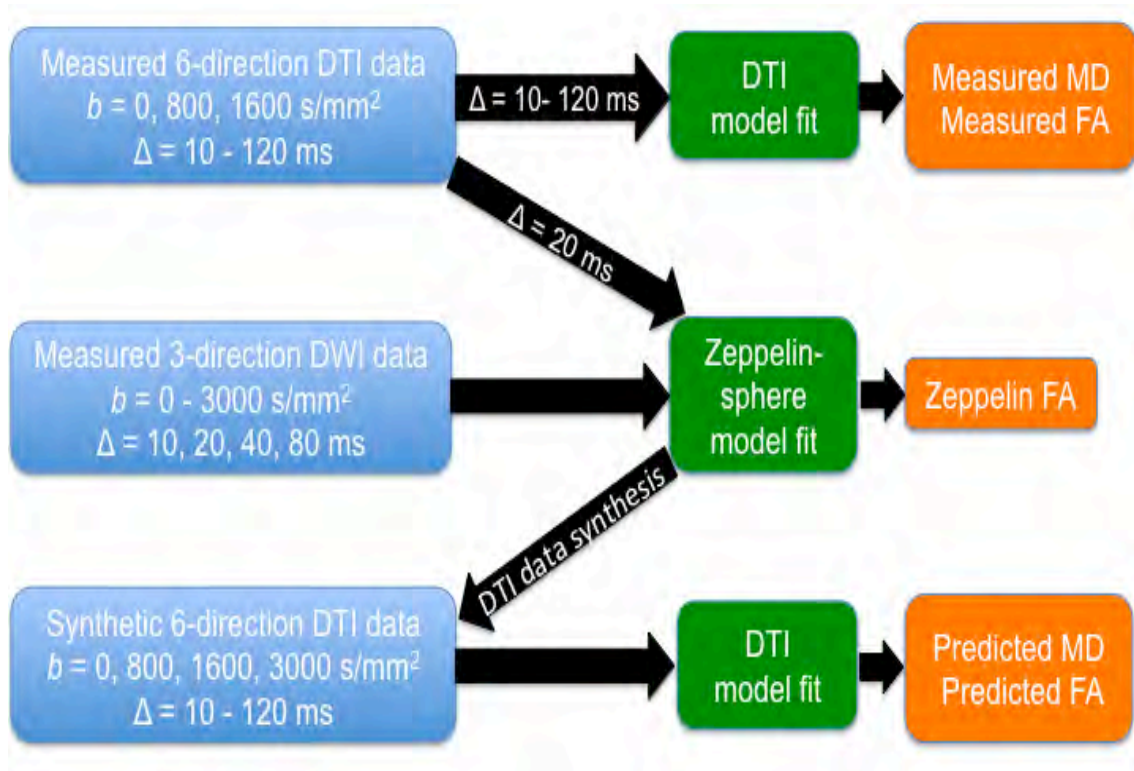


Figure 4.1 Calculation of FA and MD.

Measured and predicted MD and FA values were obtained from DTI measurements and synthetic DTI data, respectively. Zeppelin-sphere model was fitted to the combined DWI data and $\Delta = 20$ ms DTI data and then its fitted parameters were used to synthesize DTI data. DTI and Zeppelin-sphere model fitting were performed using the open source Camino toolkit.

4.3. Results

Figure 4.2 illustrates the effect of diffusion time on measured mean voxel MD and FA at $b = 800$ and 1600 s/mm^2 , and the predicted mean voxel MD and FA at $b = 800$, 1600 , and 3000 s/mm^2 . In all prostates, there was a general decrease in the mean voxel MD and a broad increase in the mean voxel FA as diffusion time increased. In Prostates 1 and 2, measured mean voxel MD and FA increased markedly in the noisier data at long diffusion time (> 70 ms). The predicted mean voxel FA at $b = 3000$ s/mm^2 is very low (< 0.2) and appears to be diffusion time independent. In contrast, the predicted mean voxel MD at $b = 3000$ s/mm^2 showed a greater diffusion time dependence than at $b = 800$, 1600 s/mm^2 .

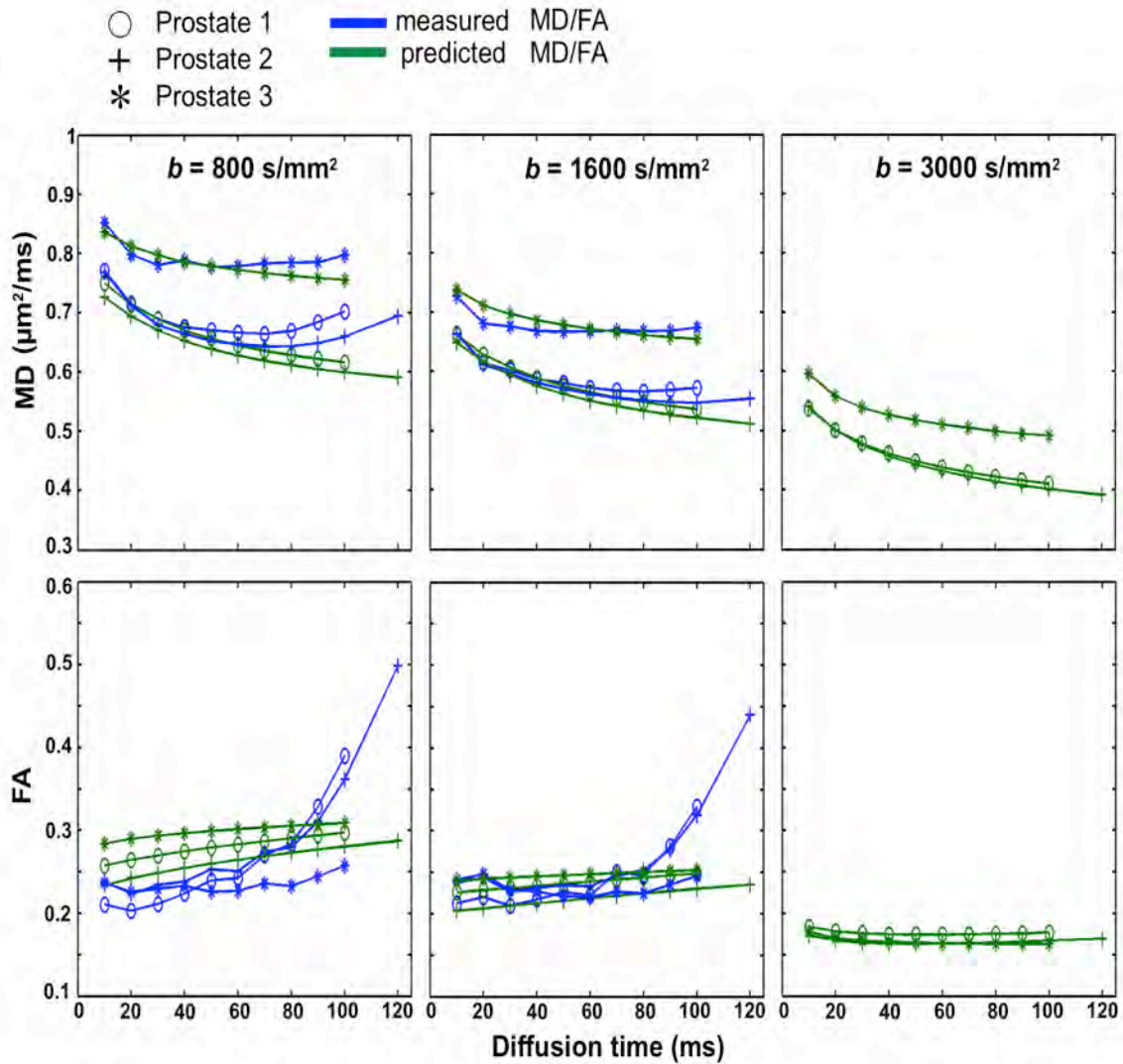


Figure 4.2 Effect of diffusion time on mean voxel MD and FA at $b = 800, 1600,$ and 3000 s/mm^2 .

Data represent the average of 3957 voxels from slices 3-6 in Prostate 1, 3510 voxels from slices 3-6 in Prostate 2, and 4680 voxels from slices 6-9 in Prostate 3.

Figure 4.3 shows the voxel-wise correlation between measured and predicted MD and FA at $b = 800 \text{ s/mm}^2$. Very similar plots were obtained for $b = 1600 \text{ s/mm}^2$ (see Figure B.1 in Appendix B). In all prostates, there was close agreement between measured and predicted MD over the range $\Delta = 10 - 70 \text{ ms}$. Correlation coefficients between measured and predicted MD are in the range of $\sim 0.48 - 0.99$ (Table 4.3). Measured and predicted FA showed a wider variance than MD with correlation coefficients in the range $\sim 0.15 - 0.75$ (Table 4.4). Measured FA was higher than predicted FA in the majority of voxels at long diffusion time.

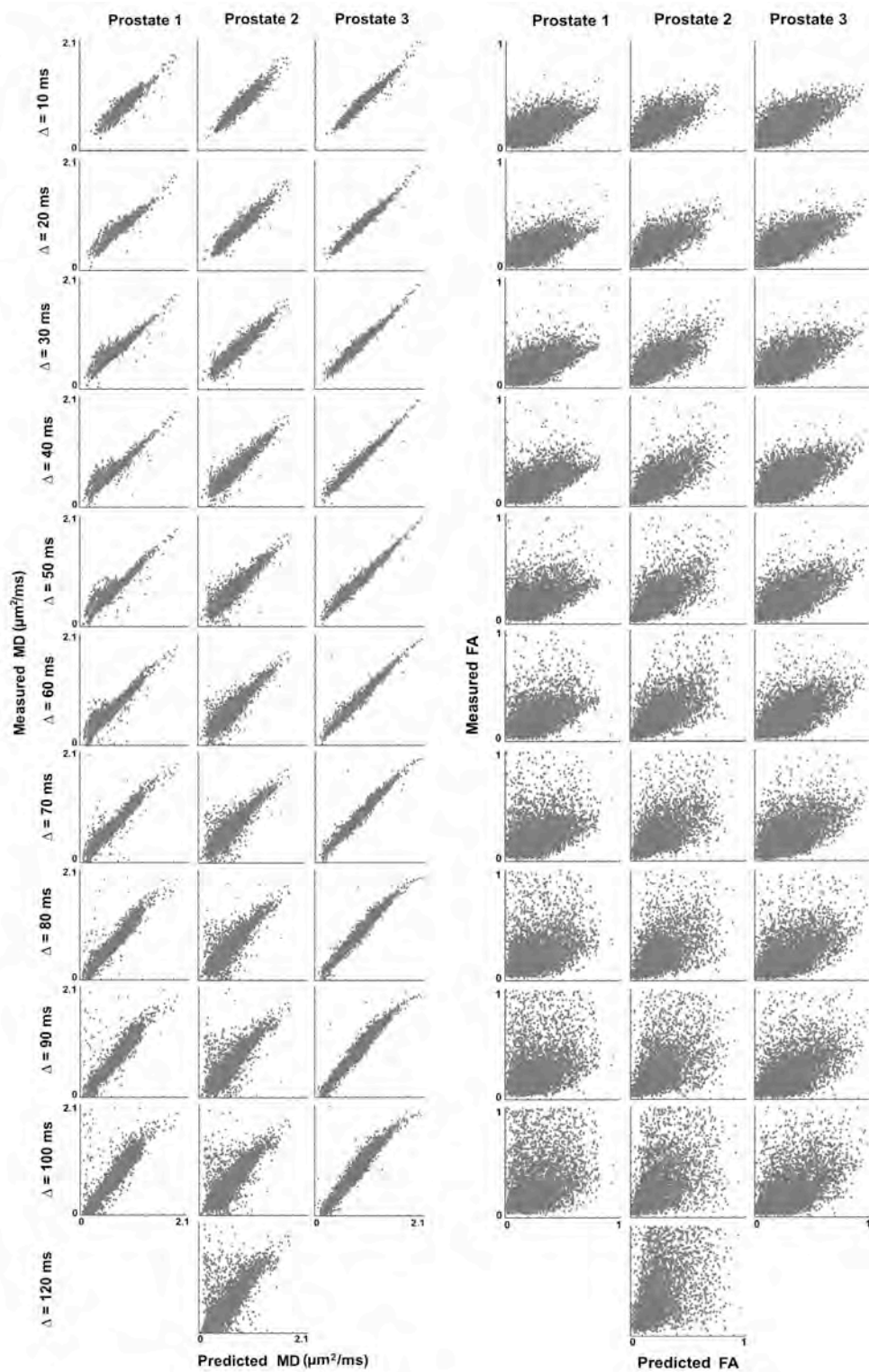


Figure 4.3 Scatter plots of measured MD and FA versus MD and FA predicted by the zeppelin-sphere model for $b = 800 \text{ s/mm}^2$.

Data are from 3957 voxels in Prostate 1, 3510 voxels in Prostate 2, and 4680 voxels in Prostate 3. The scatter plots for $b = 1600 \text{ s/mm}^2$ is provided in Figure B.1 in Appendix B.

Table 4.3 Correlation of measured MD and predicted MD ^a

Prostate	Δ (ms)	$b = 800s/mm^2$	$b = 1600s/mm^2$
1	10	0.959 (0.956, 0.961) [<0.05]	0.959 (0.956, 0.961) [<0.05]
	20	0.965 (0.963, 0.967) [<0.05]	0.966 (0.963, 0.968) [<0.05]
	30	0.959 (0.956, 0.961) [<0.05]	0.958 (0.955, 0.960) [<0.05]
	40	0.952 (0.949, 0.955) [<0.05]	0.958 (0.956, 0.961) [<0.05]
	50	0.929 (0.925, 0.933) [<0.05]	0.948 (0.945, 0.951) [<0.05]
	60	0.891 (0.885, 0.898) [<0.05]	0.936 (0.932, 0.940) [<0.05]
	70	0.894 (0.887, 0.900) [<0.05]	0.942 (0.939, 0.946) [<0.05]
	80	0.885 (0.878, 0.891) [<0.05]	0.948 (0.945, 0.951) [<0.05]
	90	0.815 (0.805, 0.826) [<0.05]	0.927 (0.922, 0.931) [<0.05]
	100	0.749 (0.735, 0.762) [<0.05]	0.906 (0.900, 0.911) [<0.05]
2	10	0.956 (0.953, 0.958) [<0.05]	0.956 (0.953, 0.959) [<0.05]
	20	0.957 (0.954, 0.960) [<0.05]	0.958 (0.955, 0.961) [<0.05]
	30	0.949 (0.946, 0.953) [<0.05]	0.955 (0.952, 0.958) [<0.05]
	40	0.929 (0.924, 0.933) [<0.05]	0.944 (0.940, 0.947) [<0.05]
	50	0.899 (0.893, 0.905) [<0.05]	0.926 (0.922, 0.931) [<0.05]
	60	0.845 (0.836, 0.855) [<0.05]	0.894 (0.887, 0.900) [<0.05]
	70	0.775 (0.762, 0.788) [<0.05]	0.849 (0.839, 0.858) [<0.05]
	80	0.758 (0.743, 0.771) [<0.05]	0.836 (0.826, 0.846) [<0.05]
	90	0.707 (0.690, 0.723) [<0.05]	0.806 (0.794, 0.817) [<0.05]
	100	0.631 (0.611, 0.651) [<0.05]	0.770 (0.756, 0.783) [<0.05]
3	10	0.978 (0.977, 0.980) [<0.05]	0.979 (0.977, 0.980) [<0.05]
	20	0.984 (0.983, 0.985) [<0.05]	0.984 (0.983, 0.985) [<0.05]
	30	0.984 (0.984, 0.985) [<0.05]	0.987 (0.986, 0.987) [<0.05]
	40	0.986 (0.985, 0.987) [<0.05]	0.988 (0.987, 0.988) [<0.05]
	50	0.984 (0.984, 0.985) [<0.05]	0.988 (0.987, 0.989) [<0.05]
	60	0.981 (0.980, 0.982) [<0.05]	0.989 (0.989, 0.990) [<0.05]
	70	0.981 (0.980, 0.982) [<0.05]	0.989 (0.988, 0.990) [<0.05]

	80	0.978 (0.977, 0.980) [<0.05]	0.982 (0.981, 0.983) [<0.05]
	90	0.969 (0.967, 0.970) [<0.05]	0.980 (0.979, 0.981) [<0.05]
	100	0.947 (0.944, 0.950) [<0.05]	0.975 (0.973, 0.976) [<0.05]
a) Data are Pearson rank correlation coefficients with 95% confidence interval in a parenthesis and p value in a bracket. Data are the same as for Fig 4.3			

Table 4.4 Correlation of measured FA and predicted FA ^a

Prostate	Δ (ms)	$b = 800\text{s/mm}^2$	$b = 1600\text{s/mm}^2$
1	10	0.548 (0.526, 0.570) [<0.05]	0.695 (0.679, 0.711) [<0.05]
	20	0.560 (0.539, 0.582) [<0.05]	0.663 (0.645, 0.680) [<0.05]
	30	0.519 (0.495, 0.541) [<0.05]	0.666 (0.648, 0.683) [<0.05]
	40	0.443 (0.418, 0.468) [<0.05]	0.610 (0.590, 0.629) [<0.05]
	50	0.329 (0.301, 0.356) [<0.05]	0.518 (0.495, 0.541) [<0.05]
	60	0.293 (0.265, 0.322) [<0.05]	0.466 (0.442, 0.491) [<0.05]
	70	0.217 (0.187, 0.247) [<0.05]	0.358 (0.330, 0.385) [<0.05]
	80	0.206 (0.176, 0.236) [<0.05]	0.344 (0.316, 0.371) [<0.05]
	90	0.152 (0.122, 0.183) [<0.05]	0.269 (0.240, 0.298) [<0.05]
	100	0.151 (0.121, 0.182) [<0.05]	0.238 (0.208, 0.267) [<0.05]
2	10	0.673 (0.654, 0.690) [<0.05]	0.712 (0.696, 0.728) [<0.05]
	20	0.715 (0.698, 0.731) [<0.05]	0.723 (0.707, 0.738) [<0.05]
	30	0.705 (0.688, 0.722) [<0.05]	0.745 (0.730, 0.759) [<0.05]
	40	0.652 (0.632, 0.670) [<0.05]	0.748 (0.733, 0.762) [<0.05]
	50	0.596 (0.575, 0.617) [<0.05]	0.691 (0.674, 0.708) [<0.05]
	60	0.572 (0.549, 0.594) [<0.05]	0.653 (0.633, 0.671) [<0.05]
	70	0.504 (0.479, 0.529) [<0.05]	0.595 (0.573, 0.616) [<0.05]
	80	0.484 (0.458, 0.509) [<0.05]	0.553 (0.530, 0.576) [<0.05]
	90	0.444 (0.417, 0.470) [<0.05]	0.516 (0.491, 0.540) [<0.05]
	100	0.403 (0.375, 0.430) [<0.05]	0.456 (0.430, 0.482) [<0.05]
	120	0.359 (0.329, 0.387) [<0.05]	0.376 (0.347, 0.404) [<0.05]
3	10	0.661 (0.645, 0.677) [<0.05]	0.743 (0.730, 0.755) [<0.05]
	20	0.673 (0.657, 0.688) [<0.05]	0.716 (0.702, 0.730) [<0.05]
	30	0.642 (0.625, 0.658) [<0.05]	0.743 (0.729, 0.755) [<0.05]
	40	0.621 (0.603, 0.638) [<0.05]	0.736 (0.722, 0.748) [<0.05]
	50	0.608 (0.590, 0.626) [<0.05]	0.709 (0.695, 0.723) [<0.05]
	60	0.581 (0.561, 0.599) [<0.05]	0.694 (0.679, 0.709) [<0.05]
	70	0.519 (0.497, 0.539) [<0.05]	0.646 (0.629, 0.662) [<0.05]
	80	0.496 (0.474, 0.517) [<0.05]	0.626 (0.609, 0.643) [<0.05]

	90	0.468 (0.445, 0.490) [<0.05]	0.567 (0.547, 0.586) [<0.05]
	100	0.437 (0.414, 0.460) [<0.05]	0.534 (0.513, 0.554) [<0.05]
a) Data are Pearson rank correlation coefficients with 95% confidence interval in a parenthesis and p value in a bracket. Data are the same as for Fig 4.3			

Figure 4.4 displays parametric maps of the Zeppelin-sphere model for each prostate. In all prostates, the anisotropic zeppelin component had higher diffusivity and greater signal fraction than the restricted sphere component. The Zeppelin-sphere model also provides a good fit to the measurement data. Representative Zeppelin-sphere model fits are presented in Figure 4.5.

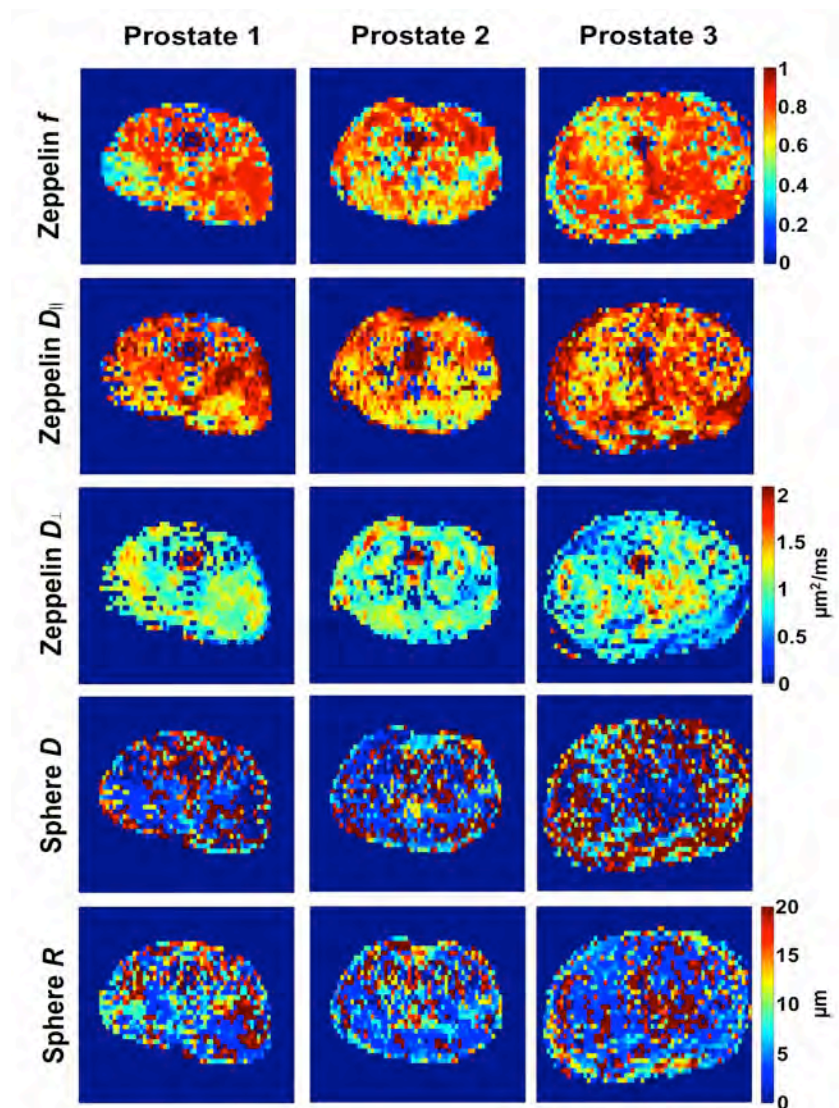


Figure 4.4 Zeppelin-sphere model parameter maps.

Data are from slice 3 in Prostate 1, slice 3 in Prostate 2, and slice 7 in Prostate 3.

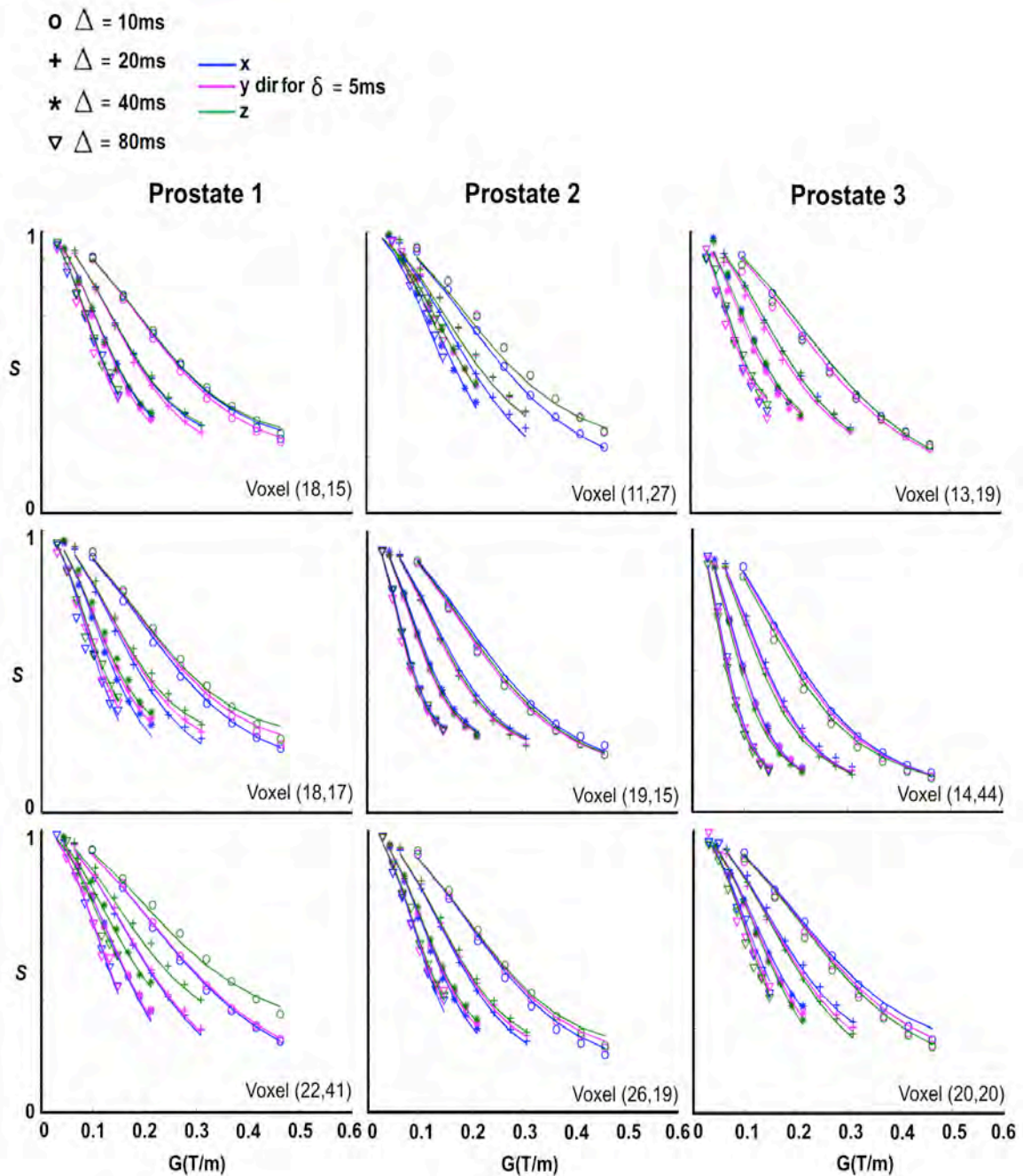


Figure 4.5 The fit of Zeppelin-sphere model to representative voxels from each prostate.

Voxel data are from slice 5 in Prostate 1, slice 5 in Prostate 2, and slice 8 in Prostate 3.

To illustrate a masking effect of the isotropic sphere component on apparent FA, Figure 4.6 shows the voxel-wise correlation between measured FA of the DTI model and the FA of the zeppelin component. As expected the Zeppelin FA was higher than DTI-

based FA except at long diffusion time where relatively low SNR caused an overestimation of DTI-based FA.

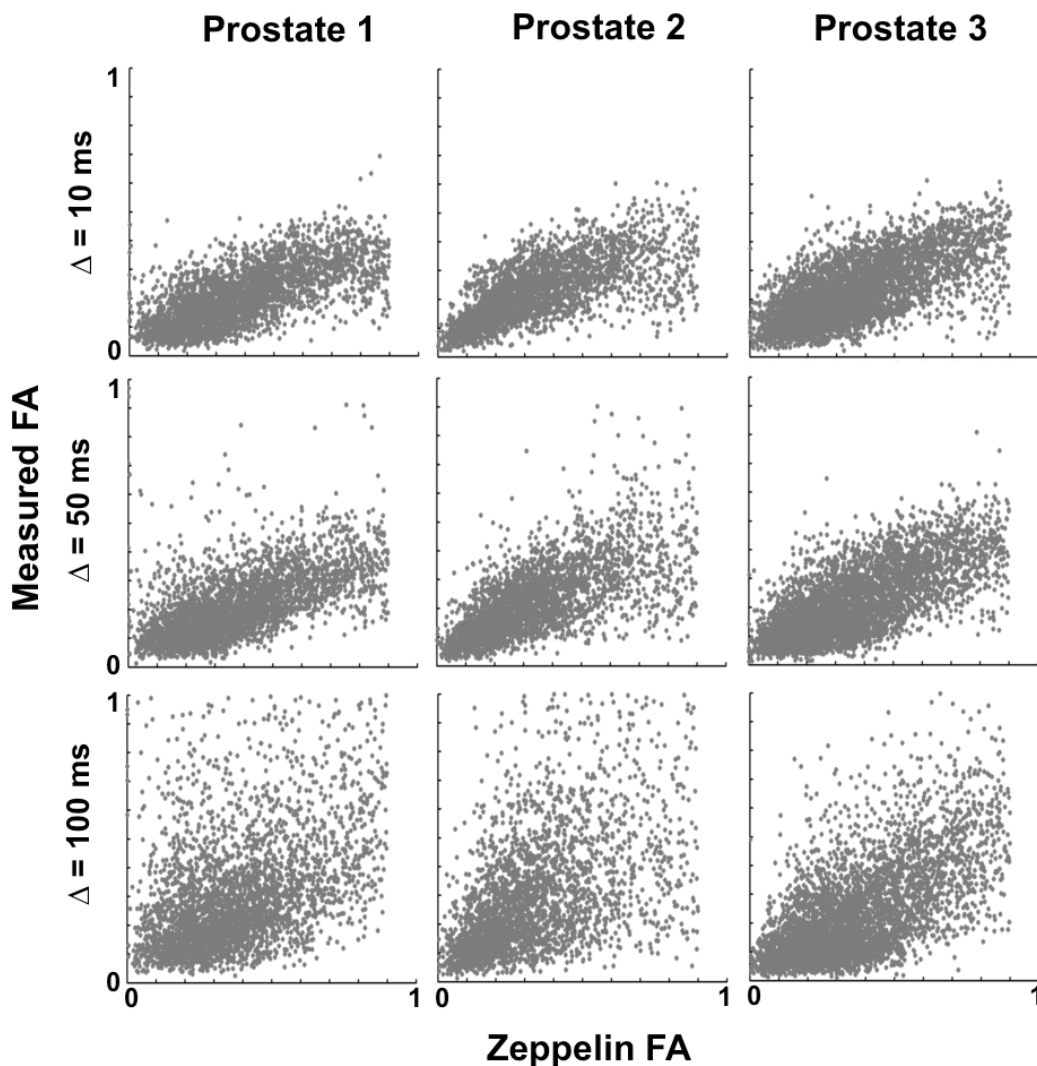


Figure 4.6 Scatter plots of measured FA versus Zeppelin FA at $b = 800$ s/mm².

Data is the same as Fig 4.3.

4.4. Discussion

Microimaging studies of fixed prostate tissue have demonstrated highly restricted diffusion and low anisotropy in the epithelium, and intermediate diffusivity and high anisotropy in the stroma [55,118]. Although previous studies of prostate tissue ex vivo indicated the existence of two distinct water diffusion environments [39,192,203], they did not model either diffusion anisotropy or restricted diffusion. A recent ex vivo

prostate study, which applied the stretched exponential model to the individual components of a ‘double-Gaussian’ biexponential model, found that these two distinct water pools were internally heterogeneous and their diffusion dynamics were diffusion time dependent (the tested diffusion times are 10, 20 and 40 ms) [40]. DWI studies of in vivo prostate also support the presence of two non-vascular diffusion environments [11,42]. The application of the VERDICT framework in prostate in vivo has used isotropic unrestricted and isotropic restricted components to describe these non-vascular water pools [42] but neglected the diffusion anisotropy. The superior performance of multi-component anisotropic and restricted models found in Chapter 3 is consistent with the presence of distinct diffusion microenvironments in prostate tissue. These anisotropic and restricted models would be expected to provide more accurate prediction of DWI signals in prostate tissue than isotropic restricted, biexponential, DTI and ADC models, which are previously used for modeling diffusion in prostate tissue. Thus this study used one of the anisotropic and restricted models tested in Chapter 3 for generating synthesized DTI data. This study shows that diffusion time dependence of MD and FA is observed for the 10 - 120 ms diffusion times and the anisotropic and restricted model accurately predicts the diffusion time dependence.

The range of the fitted Zeppelin-sphere parameters including signal fractions, diffusivities, and a sphere radius in this study is consistent with that of the same model parameter estimates in Chapter 3. It is noteworthy that the sphere radius (R) found in this study and Chapter 3 is generally lower than the R obtained by fitting the VERDICT model to in vivo data [42]. This difference is likely due to formalin fixation.

This study provides an independent validation of Zeppelin-sphere model, which describes DWI signals in prostate tissue as a sum of two signals respectively from an anisotropic Gaussian component (zeppelin) and an isotropic restricted component (sphere). This study also proposes a new way of using compartment models: application of compartment models for predicting the impact of diffusion time on MD and FA.

4.4.1. Effect of diffusion time and noise on MD

Both measured and predicted mean voxel MD showed a decrease as diffusion time increased from 10 ms to 70 ms. At long diffusion time ($\Delta > 70$ ms), the measured mean voxel MD started to increase in noisier data from Prostates 1 and 2 and the predicted mean voxel MD for these two prostates continued decreasing, indicating that the

increase in the measured mean voxel MD is a result of noise. The decrease of MD with diffusion time can be explained by the diffusion theory. At very short diffusion time, most water molecules do not have enough time to interact with the surrounding environment and the MD will be equivalent to the self-diffusion coefficient. With increasing diffusion time, more water molecules will have a chance of interacting with barriers and the MD will decrease. Therefore, measuring diffusion time dependence of the diffusivity may provide insights into the tissue microstructure [204]. For all prostates, the absolute change in MD over the range of tested diffusion times was similar. This absolute change at $b = 800, 1600$ and 3000 s/mm^2 was also similar.

The SNRs at $b = 800, 1600 \text{ s/mm}^2$, $\Delta = 80\text{-}120 \text{ ms}$ for Prostates 1 and 2 are low and range from 7 to 35. Above $\Delta = 70 \text{ ms}$, predicted MD still correlated strongly with measured MD while predicted FA showed a weak correlation with measured FA. These results indicate that MD is less susceptible to experimental noise, as compared to FA. This is probably because the calculation of MD by averaging three eigenvalues reduces the bias of each eigenvalue due to noise. Many prostate studies show that MD is significantly lower in tumours than benign tissue and is useful for the diagnosis and grading of prostate cancer [107,111,205,206]. However, FA in prostate cancer has been reported to be higher [109], lower [104], or similar [113] as compared with normal prostate.

4.4.2. Effect of diffusion time and noise on FA

Both measured and predicted mean voxel FA was low and increased as the diffusion time increased at $b = 800$ and 1600 s/mm^2 . This low mean voxel FA is in agreement with a previous study of diffusion anisotropy in seven prostates ex vivo [56]. The very low mean voxel FA at $b = 3000 \text{ s/mm}^2$ predicted by the Zeppelin-sphere model suggests that FA is basically independent of diffusion time at ultra high b -value. Above $\Delta = 70 \text{ ms}$, the measured FA in Prostates 1 and 2 showed a larger increase than the predicted FA for these two prostates and the measured FA in Prostate 3. This suggests that a large measured FA increase at long diffusion time is also likely due to noise. As noted by Pierpaoli et al [207], increasing noise (smaller SNR) can cause the eigenvalues of the diffusion tensor to diverge rapidly from their true values. As a result, the measured diffusion anisotropy will be significantly overestimated. A study of noise effect on

measurements of anisotropy suggests that SNR should be greater than ~ 20 to obtain meaningful metrics from DTI measurements [208].

Which prostate tissue features could lead to the increase of FA with diffusion time at low $b = 800$ and 1600 s/mm^2 ? Preliminary microimaging studies of fixed prostate tissue demonstrated higher anisotropy and diffusivity in the stroma than those in the epithelium [55,118]. In normal prostate, the stroma constitutes the largest volume fraction. The DWI signal arising from the stroma may be a main source of the anisotropic high diffusivity signal. If this hypothesis is true, then the FA increase can be interpreted as increasing lateral diffusion hindrance in the roughly parallel packing of stromal myocytes [55]. A previous study of diffusion anisotropy in prostate tissue reported a decrease in mean voxel FA at $b = 1600 \text{ s/mm}^2$ with increasing diffusion time ($\Delta = 20, 40, 80 \text{ ms}$) [56]. They only tested the dependence on FA over three diffusion times. In this study, FA at $b = 1600 \text{ s/mm}^2$ showed an overall increase over ten/eleven diffusion times ($\Delta = 10 - 120 \text{ ms}$) and fluctuated between 20 ms and 80 ms. The decrease of mean voxel FA with increasing b -value was observed. This decrease can be illustrated by the assumption of the fitted Zeppelin-sphere model. At low b -value, the high diffusivity water pool (the anisotropic zeppelin component) dominates the DWI signal. As the b -value increases, the signal from high diffusivity water pool will be strongly attenuated and the contribution of the low diffusivity water pool (the isotropic sphere component) will become significant.

The zeppelin-sphere model accurately predicted the diffusion time dependence of both MD and FA. The zeppelin-sphere model describes DWI signals in prostate tissue as the sum of two separate signals arising from an anisotropic unrestricted water pool (the zeppelin component) and an isotropic restricted water pool (the sphere component). The high diffusivity zeppelin component and the low diffusivity sphere component are consistent with the presence of distinct diffusion microenvironments in prostate tissue [118]. The possibility that the anisotropic unrestricted and isotropic restricted water pools correspond to the stroma and the epithelium respectively requires further investigation.

4.4.3. Clinical insights

Clinical use of the ADC model for prostate cancer detection is widespread. ADC is commonly calculated from a 3-direction measurement in conventional prostate DWI. In

this study, MD was calculated from a 6-direction DTI measurement. If voxel anisotropy were high, this would produce a strong direction dependence of ADC calculations based on a 3-direction measurement. The average FA in this study was very low. This suggests that ADC calculated from 3-direction DWI data will be minimally affected by anisotropy and thus MD can be equivalent to ADC.

The measured ADC may be highly dependent on imaging parameters [8] and measurements of anisotropy in the prostate in vivo have produced equivocal results [104,105,109,209]. As mentioned in Introduction, diffusion time is rarely reported explicitly. This study demonstrated diffusion time dependence of MD and FA in prostate tissue. These results indicate that unreported diffusion time differences between previous DWI studies of prostate tissue might have contributed to inconsistent results for the values of ADC and FA.

It is noteworthy that ADC is the mainstay of the mpMRI-based prostate cancer assessment. In the new PI-RADS guideline, the recommended DWI imaging parameters include *b*-value, TE, TR, slice thickness, FOV, In plane dimension but not diffusion time [78]. A specification of recommended diffusion time in mpMRI-DWI should be included.

4.4.4. Limitations

This study was based on DWI of prostate tissue ex vivo from a small number of patients. Ex vivo results cannot be directly related to in vivo prostate imaging. The differences from in vivo imaging include the absence of tissue perfusion and high temperature and the presence of formalin fixation and a wide range of diffusion times. All of these differences may significantly influence MD and FA. Nevertheless, the diffusion time dependence of MD and FA demonstrated in this study highlights the importance of considering and reporting diffusion time in clinical studies of prostate tissue.

In this study, all measurements applied the minimum available TE ($\sim \Delta + 8$ ms) to maximize SNR. DWI signals were normalized to the '*b* = 0' signal before model fitting to minimize T_2 effects. Therefore, the influence of TE on MD and FA would be expected to be not significant. Although previous prostate studies [199,200] demonstrated the presence of two water pools with distinct T_2 relaxation rates, it is not

clear whether different T_2 water pools correspond to two distinct water pools identified in diffusion analyses. It is an important topic for future work.

Zeppelin-sphere model used in this study assumes no water exchange between compartments. The influence of cell membrane permeability on diffusion measurements in prostate tissue has yet to be investigated. Previous experiments on cultured cells demonstrated that cell membrane permeability could have a significant impact on the model parameters depending on the applied diffusion time [62,201]. The Zeppelin-sphere model does not account for T_2 effects. Future work will explore the incorporation of compartmental exchange and T_2 effects into this two-component anisotropic and restricted model.

In the current study, only $\Delta = 20$ ms DTI data were used to define the orientation of the Zeppelin component. To improve Zeppelin-sphere model prediction about diffusion anisotropy, future work will perform the Zeppelin-sphere model fitting by including DTI data at all diffusion times.

4.5. Conclusions

In summary, this study reports diffusion time dependence of MD and FA in fixed prostate tissue observed for $\Delta = 10 - 120$ ms. The two-component anisotropic and restricted model accurately predicts the impact of diffusion time on MD and FA. These results validate the Zeppelin-sphere model, which describes DWI signals in prostate tissue as a sum of two signals respectively from an anisotropic unrestricted water pool and an isotropic restricted water pool. These findings highlight the importance of considering and reporting diffusion time in clinical DWI studies and consensus methods.

Chapter 5 Applications to Other Tissues

5.1. Introduction

In clinical DWI studies, the ADC model has been commonly used for studying cancer types including breast [31,32,210,211] and lymph nodes [34-36,181,182]. The ADC model assumes a Gaussian water displacement probability and is well known to be invalid in the heterogeneous environment of biological tissue. Although ADC values of malignant breast lesions are on average lower than those of benign lesions, there is a substantial overlap in ADC values between malignant and benign breast lesions. There is also a wide variation in the reported ADC values of benign and malignant lymph nodes [188]. These findings highlight limitations of the simple ADC model. A three-component VERDICT model, which characterizes water diffusion in the vascular, extracellular-extravascular and intracellular compartments, has recently shown success in differentiating colorectal cancer tumours and distinguishing between benign and malignant prostate tissue [41,42]. Compartment models are generally lacking for non-neural tissue. Chapter 3 has demonstrated higher information of anisotropic and restricted multi-component models than the ADC model and other unrestricted models in prostate tissue *ex vivo*, suggesting that the implementation of more sophisticated models may improve the performance of DWI in prostate cancer assessment. Recent studies report low diffusivity epithelia in prostate [118], and breast [160]. Epithelia are important tissue structures as many cancers are of epithelial origin. Cultured epithelial cell spheroids demonstrate many of the physiological properties of glandular epithelia and provide a well-controlled environment for studying distinctive structural properties that may contribute to the observed low water mobility [212]. Spheroids have been rarely used to investigate diffusion dynamics. Motivated by the successful application of compartment models in prostate tissue, this chapter extends the investigation in Chapter 3 by performing similar experiments on breast tissue, lymph nodes, and spheroids.

5.2. Methods

5.2.1. Tissue Handling and Histopathology

The study was conducted with institutional ethics approval and written informed consent from tissue donors.

Samples of breast tissue were collected from three patients during surgery, immersed in 10% neutral buffered formalin, and stored for 4-6 weeks. All the samples were imaged in a plastic casing, sampled according to the plastic casing size and washed in phosphate-buffered saline (PBS) containing 0.2% v/v Magnevist [117] for 3-4 days prior to imaging.

Spheroids were cultured from DLD-1 (human colorectal carcinoma) cell line using the liquid overlay method. 96-well plates were coated with sterile 0.75% (w/v) low-melting point agarose in PBS. The agar-coated wells were seeded with 1.8×10^6 cells/ml and incubated under standard conditions for 4 days without motion in order to secure optimal cell aggregation (final spheroids diameter of $\sim 500 \mu\text{m}$). Six spheroids were fixed with 4% paraformaldehyde for two hours, washed four times with PBS, and transferred to a 5-mm flat-bottom Shigemi NMR tube for imaging.

One sample of lymphoma from a dog and two samples of benign lymph nodes from two human patients were collected, immersed in 10% neutral buffered formalin, and stored for a night at room temperature. The samples were then washed with PBS containing 0.2% v/v Magnevist [117] before imaging.

5.2.2. MRI Acquisition

Imaging of breast tissue and lymph nodes was performed at room temperature (22 °C) on a 9.4T Bruker (Karlsruhe, Germany) BioSpec Avance III 94/20 system equipped with a 72-mm internal diameter quadrature radiofrequency coil and BGA-12S HP gradients with maximum strength 660 mT/m and slew rate 4570 T/m/s. Imaging of spheroids was performed at 25 °C in a 14T Bruker (Karlsruhe, Germany) AV600 scanner.

All diffusion-weighted measurements were performed using a PGSE sequence and preceded by the acquisition of two reference ' $b = 0$ ' images. Three-direction DWI data

were acquired at high spatial resolution with b -value range 50 - 3000 s/mm^2 . Additional DTI acquisitions were performed using six gradient directions. DWI and DTI acquisition parameters are detailed in Tables 5.1 and 5.2.

Table 5.1 DWI acquisition parameters used for imaging breast tissue						
Breast	1		2		3	
FOV (mm^2)	50×30		50×30		60×40	
Matrix size	50×30		50×30		60×40	
Voxel size (mm^3)	1×0.78×1		1×0.78×1		1×1×1	
SNR	105		209		81	
TR (ms)	4200		4200		2500	
δ (ms)	5	10	5	5	5	10
Δ (ms)	10, 20, 40, 80	20, 40, 80	10, 20, 40	20	10, 20, 40, 80	20, 40 80
TE (ms)	18, 28, 48, 88	33, 53, 93	18, 28, 48	28	18, 28, 48, 88	33, 53, 93
b-value (s/mm^2) 6 directions	965, 1873		800, 1600	196, 435, 1189, 2302, 3000	965, 1873	
b-value^a (s/mm^2) 3 directions	100, 311, 603, 965, 1391, 1873, 2411, 3000		50, 196, 435, 766, 1189, 1702, 2306, 3000		100, 311, 603, 965, 1391, 1873, 2411, 3000	
a) Nominal b -value. Effective b -values were used for model fitting.						

Table 5.2 DWI acquisition parameters used for imaging spheroids and lymph nodes				
Tissue	Spheroids			Lymph nodes
FOV (mm²)	5×5×1.6			35×35
Matrix size	62×62×20			64×64
Voxel size (mm³)	0.08×0.08×0.08			0.5×0.5×0.5
SNR	17			70
TR (ms)	400			2000
δ (ms)	2	2	2	5
Δ (ms)	10	20	40	10, 20, 40, 80
TE (ms)	19	26	46	22, 29, 49, 89
<i>b</i>-value (s/mm²) 6 directions	1000			800, 1600
<i>b</i>-value ^a (s/mm²) 3 directions	100, 311, 603, 965	100, 311, 603, 965, 1391, 1873	100, 311, 603, 965, 1391, 1873, 2411, 3000	100, 311, 603, 965, 1391, 1873, 2411, 3000
a) Nominal <i>b</i> -value. Effective <i>b</i> -values were used for model fitting.				

5.2.3. Model Description

In this study, eleven models (see Table 3.2 in Chapter 3), including different combinations of isotropic, anisotropic and restricted components, were tested on breast tissue and lymph nodes. It was assumed that diffusivity of spheroids was the same in all directions. So three isotropic models (Ball, Bi-ball, Ball-sphere) were tested on spheroids.

5.2.4. Model Fitting and Ranking

Each model was fitted to the combined 6- and 3-direction data using the Levenberg-Marquardt minimization algorithm in the open source Camino toolkit [194]. Data were normalized to the ' $b = 0$ ' signal to reduce T_2 dependence. Diffusivities were constrained to be within biologically plausible limits so that $0 < D < 2.1 \mu\text{m}^2/\text{ms}$. For the 'sphere' model, the radius was constrained to be $0.1 < R < 20 \mu\text{m}$. AIC was calculated to provide an objective quantitative estimate of the information of the models. Eleven models were fitted voxel by voxel in breast tissue and lymph nodes. A recent microimaging study of breast tissue ex vivo demonstrated that epithelial cell layers in gland had lower diffusivity than their adjacent supporting stroma [160]. Motivated by this finding, the performance of the eleven models in gland lobules from Breast 1 was also assessed.

5.2.5. ROI selection

For breast tissue including fat, gland lobule and interlobular stroma, 3445, 3289 and 4765 voxels from 3-4 slices in Breast 1, 2 and 3 respectively were selected for analysis. These selected voxels are from manual definition of masks that excluded the capsule and NMR tube on reference ($b = 0$) images. For glandular breast tissue, 68 ROIs (102 voxels) delineating gland lobule were drawn freehand on T_2 weighted image of a representative slice of Breast 1 (Fig 5.4A). Note that these ROIs do not include fat and interlobular stroma.

Four voxels from the center of each spheroid were selected on a reference ($b = 0$) image (Fig 5.6).

The total of 1203 voxels from dog and human lymph nodes were selected for analysis by manual definition of masks that excluded the background.

5.3. Results

5.3.1. Breast Tissue

Figure 5.1 shows the overall AIC rankings of the eleven models over all voxels from three or four adjacent slices of three breast samples and the anatomical distribution of the highest ranked models in a representative slice of each breast sample. Figure 5.2 presents the rank variation of the individual models. In all breast tissue samples, either Zeppelin-sphere or Ball-sphere model was ranked highest in the majority of voxels. The other restricted two-component model, Tensor-sphere model ranked closely to Zeppelin-sphere and Ball-sphere models. For Breast 2, the three-component Ball-stick-sphere and Bi-ball-zeppelin models did not find a solution within diffusion constraints in the majority of voxels so they were ranked lowest. These results indicate that two-component restricted models provide more information-rich descriptions of multi- b , multi- Δ , DWI measurement data than single- and multi-component models that do not account for diffusion restriction.

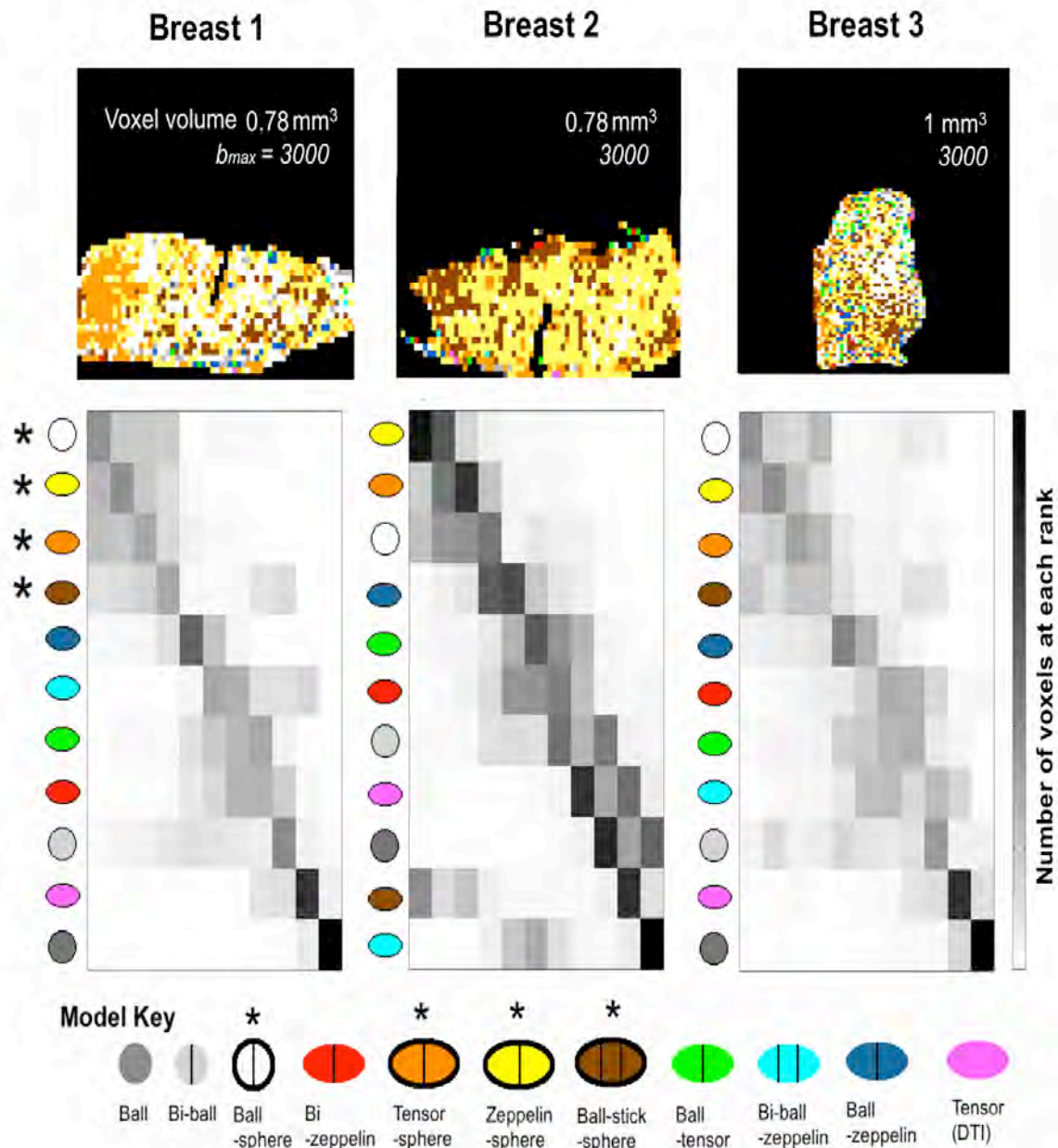


Figure 5.1 Variation of model rankings in three breast samples.

A) Anatomical distribution of the highest ranked model in a representative slice from each breast. Voxel color indicates model according to the Model Key. B) Variation in model ranking positions. The gray scale indicates the number of times each model ranked at each position. The model order is based on the trends assessed subjectively. Data are from 3445 voxels from slices 9-11 in Breast 1, 3289 voxels from slices 9-11 in Breast 2, and 4765 voxels from slices 1-4 in Breast 3. Model Key: the four models containing a restricted component are shown with a bold black border; models with an anisotropic component are shown as ellipses; vertical lines indicate the number of components; models including a restricted component are marked with an asterisk.

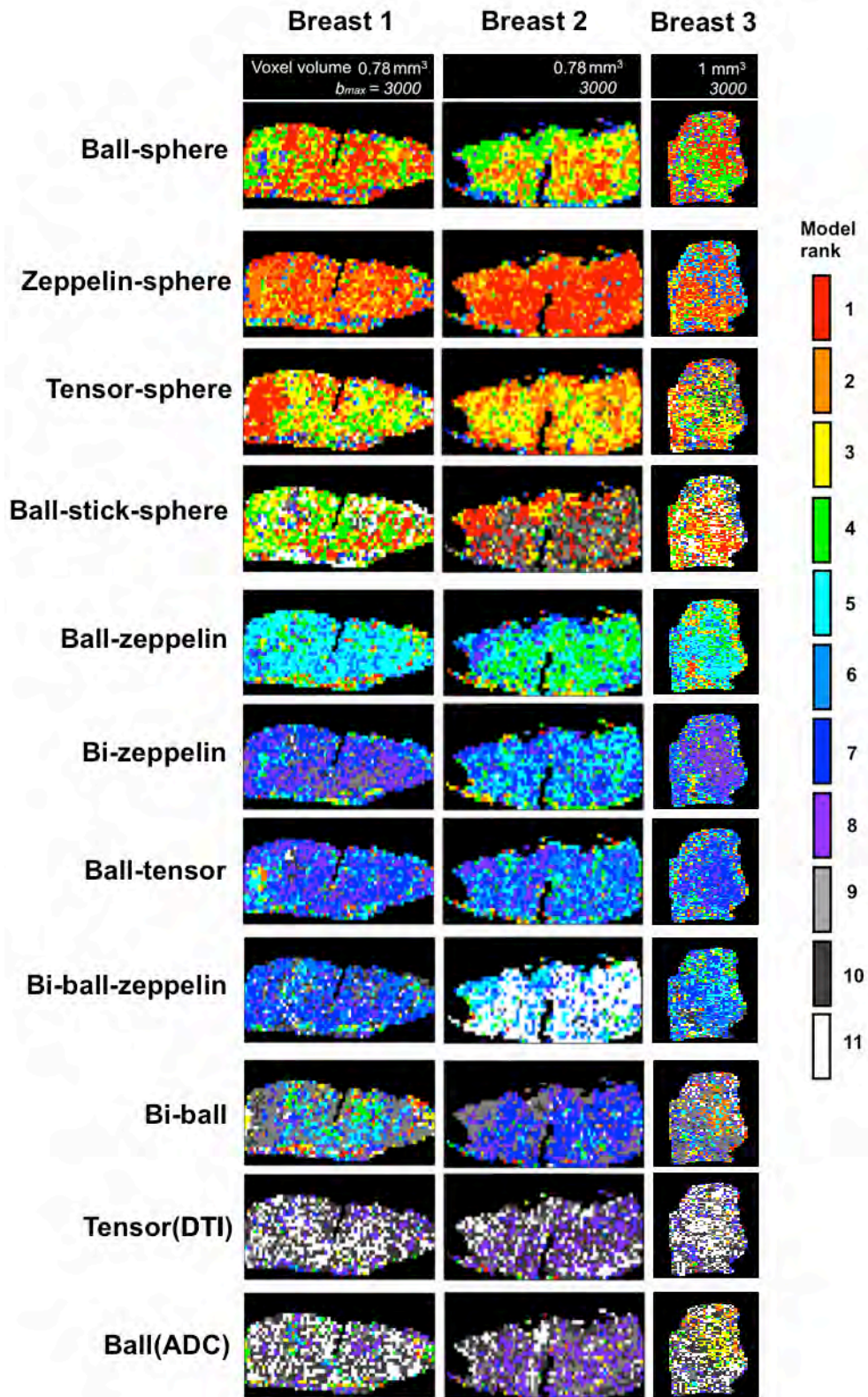


Figure 5.2 Variation in rankings of individual models in three breasts.

Slice positions as for Fig 5.1. Voxel color indicates model rank and models are grouped according to predominant rank.

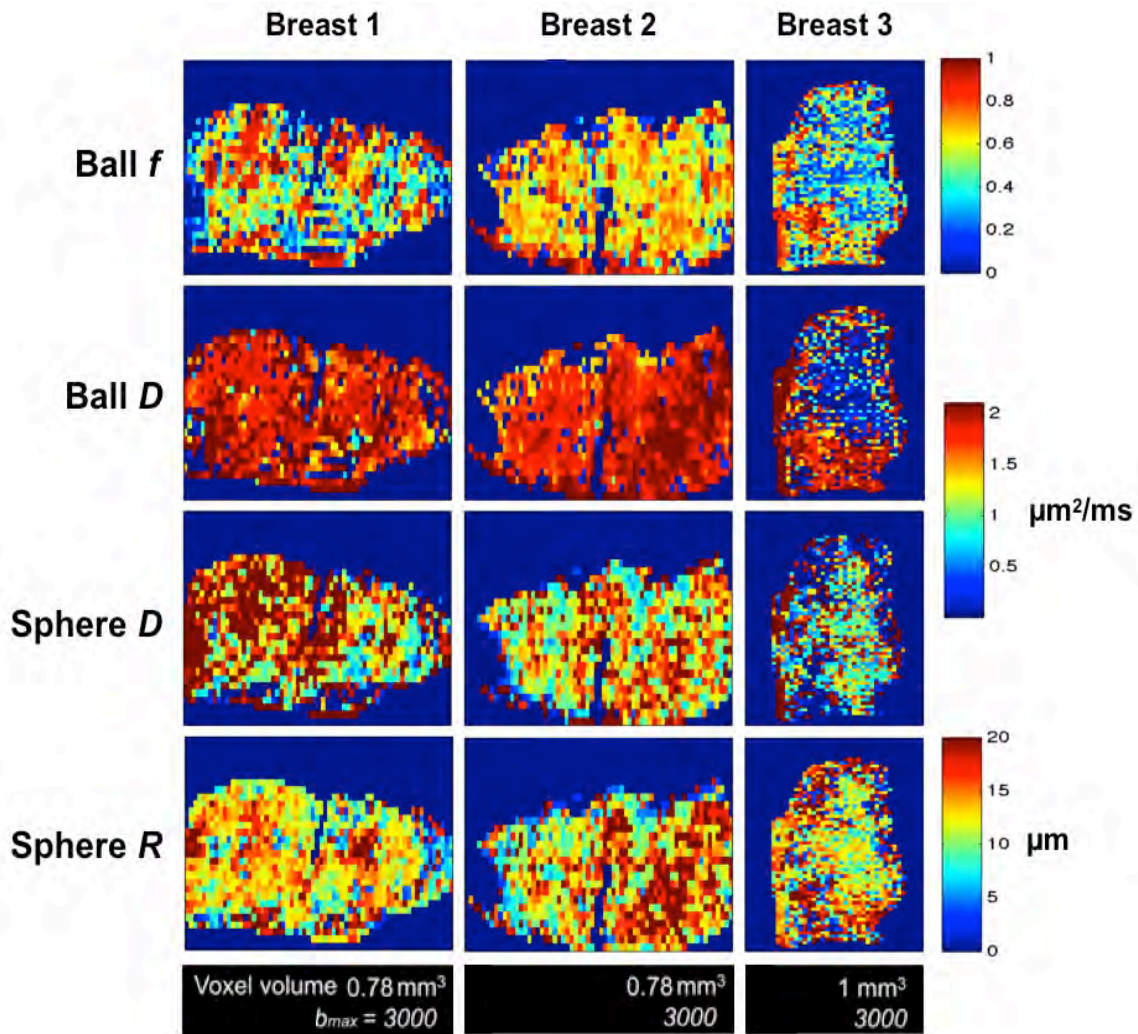


Figure 5.3 Ball-sphere model parameter maps.

Slice positions as for Fig 5.1. Parameter maps for the Zeppelin-sphere model for the same slices are provided in Figures C.1.

Parametric maps derived from the Ball-sphere model are presented in Figure 5.3. Figure 5.4B presents the AIC ranking of the eleven models over 102 voxels from 68 gland ROIs (see Fig 5.4A) of breast tissue. The models that included the restricted sphere component ranked highest, while the unrestricted Ball (ADC), Bi-ball (biexponential) and DTI models ranked lowest.

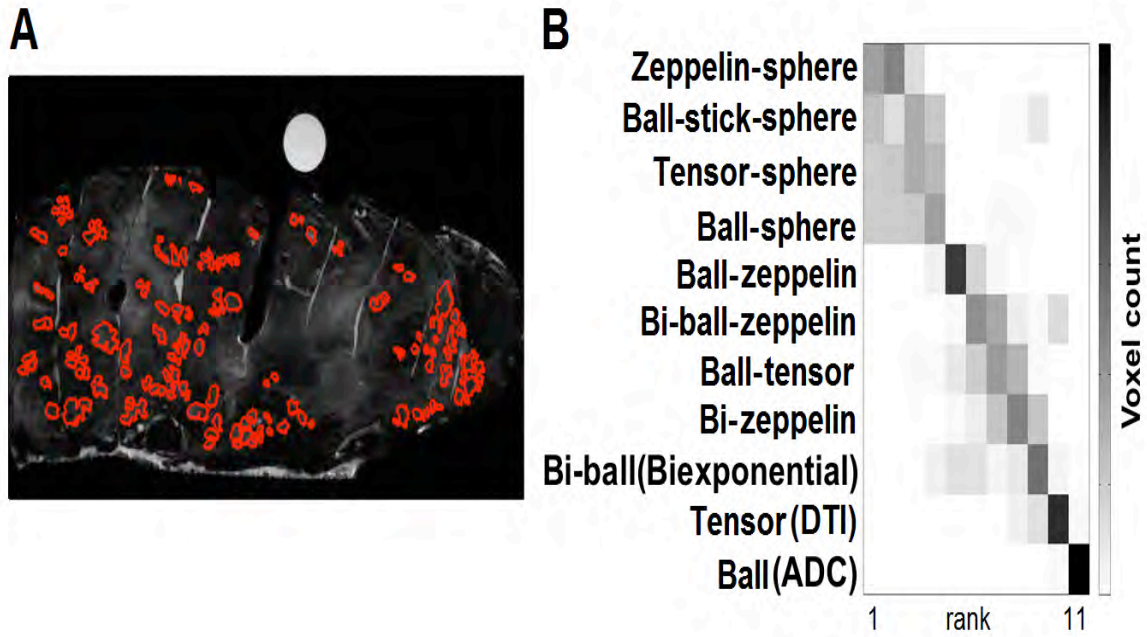


Figure 5.4 Variation of model rankings in gland ROIs.

A) T_2 weighted image of a representative slice from breast tissue showing gland ROIs in red. B) Variation of model rankings. The gray scale indicates the number of times each model ranked at each position. The model order is based on the trends assessed subjectively. Data are from 102 voxels of 68 gland ROIs in slice 9 of breast tissue.

Figure 5.5 illustrates the fit of eleven models to a representative voxel from gland ROIs with the corresponding AIC ranking position. The FA value of the representative voxel is 0.1, which is the average FA of all gland ROIs. The anisotropic and restricted two-component models ranked highest in the representative voxel and provided a better fit than the isotropic restricted model and unrestricted models.

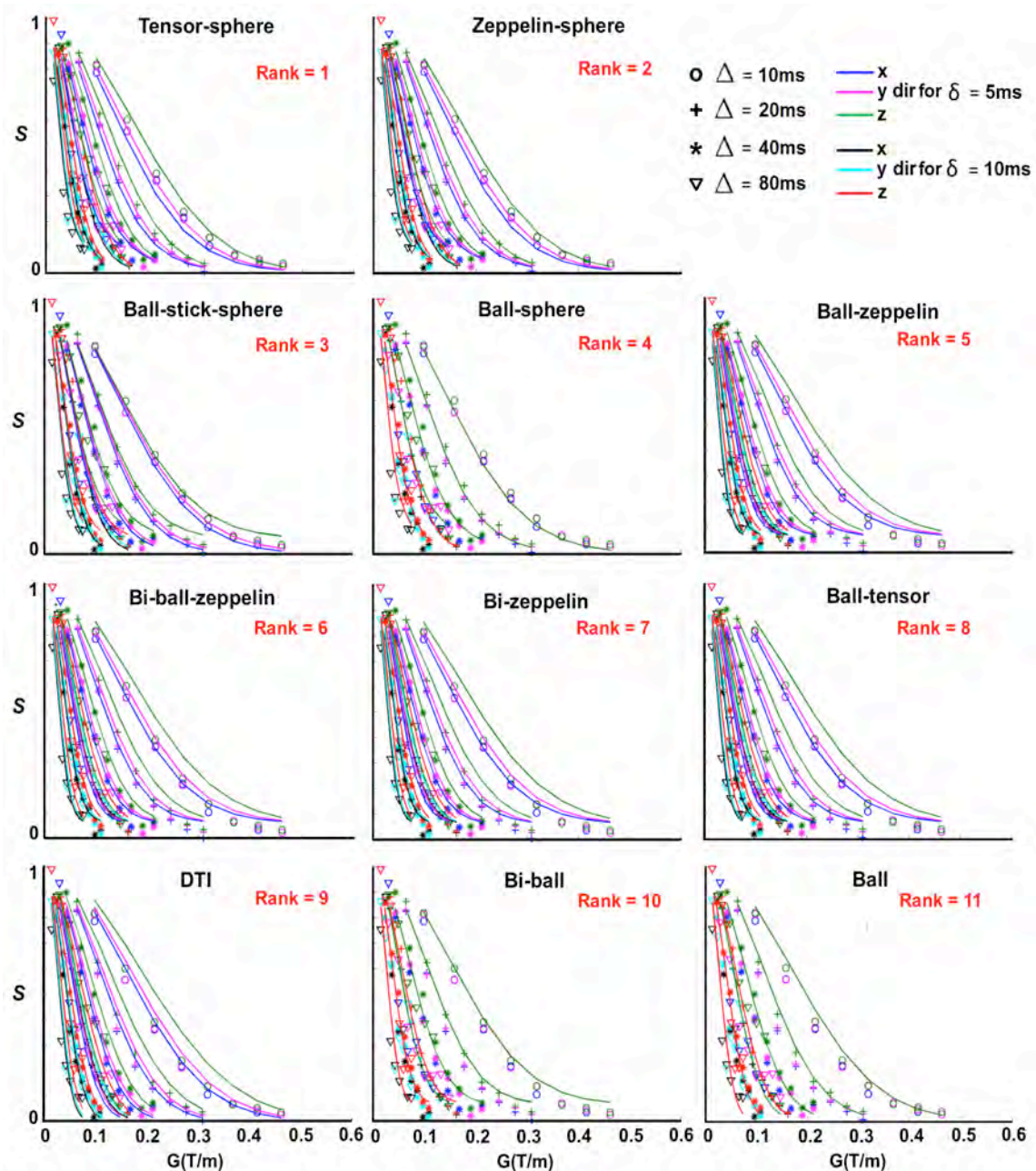


Figure 5.5 Fits of eleven models.

Normalized signal S is plotted as function of the gradient strength G . The raw signal is shown with point markers and the model fit as solid lines. Data are from the representative voxel with $FA = 0.1$ which is the mean FA of 68 gland ROIs in slice 9 of breast tissue.

Table 5.3 summarizes values of the sphere radius R from the four restricted models in all gland ROIs. The mean sphere radius is approximately $13 \mu\text{m}$.

Table 5.3 Sphere radius estimates from four models in breast tissue ^a	
Model	R (μm) Mean \pm standard deviation
Zeppelin-sphere	12 \pm 4
Ball-stick-sphere	13 \pm 3
Tensor-sphere	12 \pm 3
Ball-sphere	13 \pm 3
a) Data from 102 voxels of 68 gland ROIs in slice 9 of breast tissue	

5.3.2. Epithelial Cell Spheroids

In the majority of the 24 selected voxels (Fig 5.6), the ranking of three isotropic models by AIC showed that the Ball-sphere had higher information in spheroids than Bi-ball and Ball models.

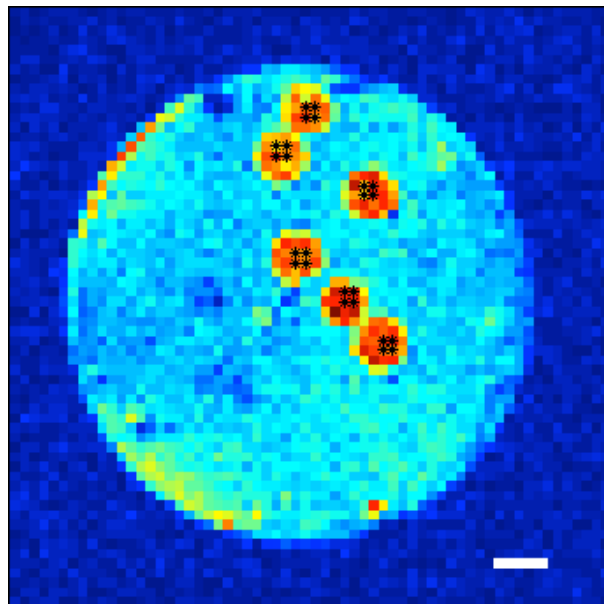


Figure 5.6 A reference ($b = 0$) image of spheroids showing 24 selected voxels marked with *. Scale bar = 500 μm .

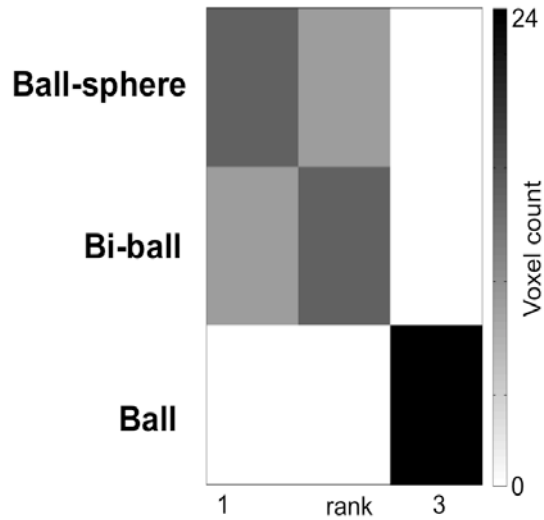


Figure 5.7 Variation of model rankings in spheroids.

The gray scale indicates the number of times each model ranked at each position. The model order is based on the trends assessed subjectively. Data are from 24 selected voxels of spheroids.

Table 5.4 lists the estimated Ball-sphere model parameters for fits to the 24 individual voxels. The ball component has higher diffusivity and lower signal fraction than the sphere component. The sphere radius of 10.9 μm is consistent with typical cell diameters for spheroids [213].

Table 5.4 Mean and standard deviation of Ball-sphere parameters in 24 voxels of spheroids	
$R (\mu\text{m})$	10.9±3.9
f_{sphere}	0.68±0.15
$D_{\text{ball}} (\mu\text{m}^2/\text{ms})$	1.5±0.9
$D_{\text{sphere}} (\mu\text{m}^2/\text{ms})$	0.93±0.77

5.3.3. Lymph Node Tissue

Figure 5.8 shows the variation in AIC ranking of eleven models for lymph nodes. Three samples of lymph nodes were imaged (Fig 5.8A). The blue dyed sample is dog lymphoma. The other two samples are benign human nodes. Four restricted models were ranked highest in the majority of voxels. The single-component ADC and DTI models ranked lowest.

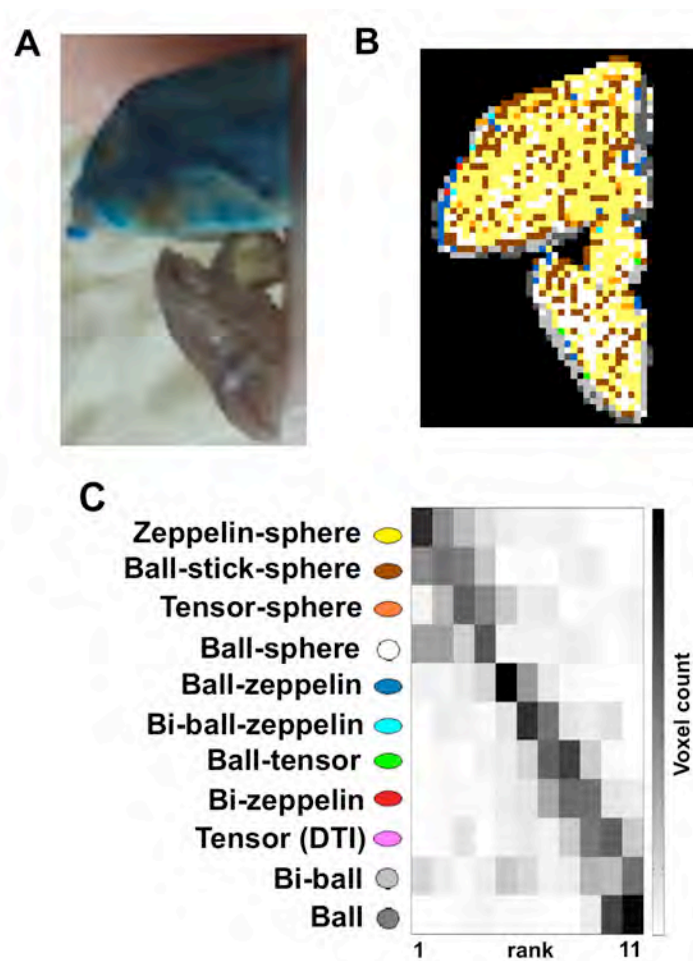


Figure 5.8 Variation of model rankings in lymph nodes.

A) 9.4T imaging setup for three lymph nodes. The blue dyed sample at the top is dog lymphoma. The round sample in the middle and the sample at the bottom are benign human lymph nodes. B) The anatomical distribution of the highest ranked model in a single slice of three lymph nodes. Voxel color indicates model according to the model symbol in 5.8C. C) Variation in model rank positions. The gray scale indicates the number of times each model ranked at each position. The model order is based on the

trends assessed subjectively. Data are from 1203 voxels in a single slice of lymph nodes.

5.4. Discussion

Restricted and hindered diffusion of water within a complex environment of biological tissue leads to a non-Gaussian water displacement probability, which is manifested as non-monoexponential DWI signal decay over a range of b -values. In addition, perfusion effects may significantly affect DWI measurements that include very low b -values (for example, $b < 100 - 150 \text{ s/mm}^2$) and cause non-monoexponential DWI signal attenuation. The biexponential-based IVIM model has been used to separate perfusion from true diffusion in breast and lymph nodes in vivo [146,147,189,191]. However, its description of diffusion in the non-vascular environment remains simple and does not account for tissue geometry. An in vivo pilot study of breast tumours utilized the VERDICT framework, which addressed the limitations of the IVIM model by modelling the non-vascular environment as a combination of a restricted diffusion component and an unrestricted Gaussian diffusion component [162].

This study provided further information about the non-vascular diffusion environment in breast tissue and lymph nodes by comparing eleven different compartment models, and about the diffusion environment in spheroids by comparing three compartment models. The results show that multi-component models that account for diffusion restriction provide more information-rich descriptions of multi- Δ , multi- b DWI measurements in all three types of tissue than ADC and other unrestricted models. This study also suggests that both anisotropic and restricted components are required to accurately describe DWI signals in breast gland lobule. In clinical DWI studies of breast tissue and lymph nodes, the ADC model has been the most commonly used approach for cancer detection. The relatively poor performance of the ADC model in this study suggests that more sophisticated DWI protocols and models may improve cancer imaging.

The restriction radius of $10.9 \mu\text{m}$ estimated by the Ball-sphere model is consistent with the known cell size in spheroids grown from epithelial cells. Many cancers are of epithelial origin. Cultured epithelial cell spheroids can mimic the tumour microenvironment and provide a well-controlled environment for studying numerous

tissue properties. Thus studies of water diffusion in cultured spheroids will enhance understanding of the tissue microstructure properties that affect diffusion contrast.

5.4.1. Breast Tissue

In Breast samples 1 and 3, the Ball-sphere model ranked highest in the majority of voxels from breast tissue including gland lobule, interlobular stroma, and fat. This finding is consistent with a recent study of breast tumour in vivo testing three versions of the VERDICT model (Ball-ball-sphere, Ball-stick-sphere, and Ball-zeppelin-sphere models) [162]. The in vivo VERDICT study shows that the Ball-ball-sphere model, which used ball and sphere components to describe the non-vascular diffusion environment, characterized the tumour structure the best and returned parameters in agreement with histological features. There is an important difference between this study and the in vivo breast VERDICT study. The VERDICT model fixed the pseudodiffusion coefficient of the vascular component and assumed intra- and extracellular diffusivities to be equal. These constraints are necessary to avoid overfitting of the relatively low SNR in vivo data. In contrast, this study allowed all diffusivities to float within biophysical limits. That is because this study used high SNR measurements with a wide range of b -values and diffusion times, which enable reliable fitting of highly parameterized models with few constraints on parameter values. The Ball-sphere model returned values of parameters (diffusivities, sphere radius, and signal fractions) that were less than the defined limits in the majority of voxels, suggesting that it was a biophysically plausible model. In all three breast samples, the multi-component restricted models were superior to unrestricted models, indicating the importance of accounting for restricted diffusion in any modelling of breast tissue.

Breast gland lobules (the ROIs in Fig 5.4A) are comprised of epithelium and intralobular fibrous stroma. A preliminary microimaging study of fixed breast tissue demonstrated lower diffusivity in the epithelium than that in the fibrous stroma [160]. The highest AIC ranking of multi-compartment restricted and anisotropic models (Fig 5.4B) is consistent with the presence of distinct diffusion microenvironments in breast gland lobules. A recent study of breast tissue ex vivo also demonstrated that two-component restricted and anisotropic models best characterized the signals in glandular breast tissue [163]. The range of the fitted Zeppelin-sphere parameters including signal fractions and diffusivities (see Figure C.1 in Appendix C) in this study is consistent with

that of the same model parameter estimates in [163]. In addition, anisotropic restricted models ranked higher than the isotropic restricted Ball-sphere model, indicating the presence of significant diffusion anisotropy in one population of water molecules at voxel volume = 0.78 mm^3 . This suggestion is supported by the observed high anisotropy in the fibrous stroma [160]. In Chapter 3, anisotropic restricted models were also found to have highest information in fixed prostate tissue and returned the sphere radius estimates consistent with the typical cell size. Similar to the finding in [160], lower diffusivity and low anisotropy in epithelium relative to fibromuscular stroma have been reported for prostate tissue [55,117,118]. The results obtained from both breast gland lobules and prostate tissue strongly suggest that the isotropic restricted and anisotropic unrestricted water pools identified in diffusion analyses correspond to epithelium and stroma respectively. This possibility requires further investigation.

5.4.2. Epithelial Cell Spheroids

This study shows that the two-component Ball-sphere model has highest information of three isotropic models in the majority of selected voxels. The Ball-sphere model uses isotropic restricted (sphere) and isotropic unrestricted (ball) components to describe the diffusion environment in spheroids. The ball component has higher diffusivity than the sphere component. Previous studies demonstrated the presence of fast and slow diffusing water pools in tumour cell spheroids [171,172]. It is worth noting that the study of Smouha et al. [171] used non-negative least square analysis instead of a two-component model to analyse diffusion and T_2 relaxation in C6 glioma and MLS human carcinoma spheroids. They found that the fast and slow diffusing water pools also differed in T_2 relaxation and the diffusivity of the slow diffusing water pool exhibited diffusion time dependence. The slow diffusing water pool described by Smouha et al. [171] probably corresponds to the sphere component, and the fast diffusing water pool to the ball component. The mean sphere radius of $10.9 \text{ }\mu\text{m}$ for fits to 24 voxels in spheroids is in good agreement with typical cell diameter ($\sim 20\text{-}25 \text{ }\mu\text{m}$) for DLD-1 spheroids [213], strongly suggesting that the restricted water pool primarily consists of intracellular water. This suggestion is supported by Smouha et al. [171] showing that the volume fraction of the slow diffusing water pool was consistent with the intracellular volume fraction. Taken together, these results suggest that the isotropic restricted sphere component and the isotropic unrestricted ball component correspond to intracellular water and extracellular water respectively. The low ball signal fraction

(extracellular volume fraction) in spheroids support the hypothesis that tight junctions between epithelial cells function as a barrier by minimizing any signal from fast diffusing paracellular water and thus cause the low diffusivity of epithelia observed in diffusion microimaging [118,160,170]. The sphere signal fraction of 0.68 is noteworthy, as the intracellular volume fraction of pelleted single cells, for example yeast [214] and erythrocyte [215], does not normally exceed 0.5.

5.4.3. Lymph Node Tissue

This study shows that multi-component restricted models extract more information from DWI measurements in lymphoma and benign lymph nodes than single-component (ADC and DTI) models and multi-component unrestricted models. In Chapter 3 and this Chapter, multi-component restricted models have also been found to have higher information than single-component (ADC and DTI) models and multi-component unrestricted models in prostate, breast, and spheroids. These results indicate the importance of accounting for restricted diffusion in modelling of diffusion in these four types of non-neural tissue.

Many previous studies have investigated the feasibility of DWI in differentiating benign from malignant lymph nodes using the ADC model. The ADC values of malignant lymph nodes were usually found to be lower than those of benign lymph nodes [34-36,181,182]. However, some studies observed higher ADC values in malignant than in benign lymph nodes [183-185]. Two studies found no significant differences in ADC between benign and malignant lymph nodes [186,187]. Inconsistent ADC values reported in previous DWI studies of lymph node highlight the limitation of ADC model. Two recent studies have used the IVIM model for discrimination between malignant and benign lymph nodes in rectal cancer [189,190]. Although both studies demonstrated its diagnostic value, they reported inconsistent differences between some IVIM model parameters (diffusion coefficient and perfusion fraction) of malignant and benign lymph nodes. Neither the ADC model nor the IVIM model accounts for restricted diffusion. The overall AIC ranking in lymph nodes shows that Ball (ADC), Bi-ball (biexponential) and DTI models rank lowest. This finding suggests that more sophisticated models such as VERDICT model that includes a restricted component may provide more accurate and reliable detection of malignant lymph nodes.

5.4.4. Limitations

This study has several limitations. The results were obtained from a small number of samples for each type of tissue. Future work will assess the performance of compartment models, in particular multi-component restricted models, in a large number of samples.

This study is based on diffusion imaging of formalin-fixed tissue. Ex vivo imaging has several advantages: (1) it can acquire high SNR and high spatial resolution measurement data; (2) it allows long scan time; (3) it is less expensive than in vivo imaging; (4) it is free from organ movement, perfusion, and susceptibility which are present in in vivo imaging. However, the absence of perfusion may lead to a decrease in the volume of extracellular-extravascular water. This decrease would be expected to affect the signal fractions for each compartment.

Formaldehyde fixation stabilizes the tissue against degradation by cross-linking proteins. However, tissue fixation results in a significant reduction in measured diffusivity [113,192]. Nevertheless, previous DWI studies of prostate and white matter suggest that formalin fixation is unlikely to affect the model ranking [39,198].

The eleven models tested in this study assume no water exchange between compartments. Previous experiments on cultured cells demonstrated that cell membrane permeability could have a significant impact on the model parameters depending on the applied diffusion time [62,201]. Future work will add permeability parameters to account for exchange between compartments.

In this study, DWI signals were normalized to the ' $b = 0$ ' signal before model fitting to minimize T_2 effects. A previous study of tumour cell spheroids demonstrated that the fast and slow diffusing water pools identified in diffusion analyses also differed in T_2 relaxation [171]. They found that T_2 for the slow diffusing water pool was significantly shorter than that for the fast diffusing water pool. Future work will explore the incorporation of T_2 effects into compartment models.

The differences between ex vivo and in vivo imaging include tissue perfusion, temperature, tissue fixation, the available range of diffusion times and gradient strength. Although the results presented in this ex vivo study cannot be directly related to in vivo imaging, they clearly describe some tissue structure features that can be detected by

DWI and provide basic science evidence to inform the further development of clinical imaging methods.

5.5. Conclusions

When DWI is performed in breast tissue, lymph nodes and spheroids over a wide range of b -values and multiple diffusion times, multi-component restricted models extract more information from DWI measurements than single-component models and multi-component models that do not account for diffusion restriction. These results highlight the importance of inclusion of a restricted diffusion compartment in modelling of diffusion in breast tissue, lymph nodes and spheroids.

The superior performance of restricted and anisotropic two-component models in gland ROIs is consistent with the presence of distinct diffusion microenvironment in breast gland lobules. Development of clinical DWI methods sensitive to changes in this microenvironment might increase accuracy of breast cancer detection. In cultured epithelial cell spheroids, the isotropic and restricted model returns the mean sphere radius consistent with known cell diameter. Many cancers are of epithelial origin. Cultured epithelial cell spheroids can mimic the tumour microenvironment and provide a well-controlled environment for studying tissue properties. Thus investigation of diffusion dynamics in spheroids will enhance understanding of the tissue microstructure properties that affect diffusion contrast in clinical imaging.

Chapter 6 Conclusions

DWI has become a popular clinical imaging method as it has the ability to probe the tissue microstructure. Its main clinical application has been the diagnosis of neurological disorders. It also becomes a standard imaging method for detection of cancer lesions in other organs such as prostate and breast. To infer tissue structure from DWI measurements, a variety of models have been proposed to characterize DWI signals in tissue. The recent trend is towards compartment models, which are based on assumptions about the underlying tissue structure. Compartment models have been mainly used in the brain. They can provide more insightful information on tissue features such as axon radius in white matter [17-21] or neurite orientation distribution [22]. However, compartment models are generally lacking for non-neural tissue. A three-component VERDICT model, which is based on vascular, extracellular-extravascular and intracellular compartments, has recently been used to characterize diffusion signals in colorectal cancer cell lines and prostate tissue, and produced promising results [41,42].

The work in this thesis has implemented predefined compartment models in prostate, breast, lymph nodes and spheroids, selected models that extract the most information from the given set of measurement data and identified compartments which are necessary for accurately describing DWI signals in these four types of non-neural tissue. As noted in Chapter 1, the ultimate goal of this work is to obtain specific microstructure features (ideally diagnostic features) for these four types of tissue using DWI measurements. There are three distinct, but not independent processes. The first step is defining a DWI scan protocol that can acquire appropriate tissue structure information. The second step is constructing models that can relate microstructural features to DWI signals. The third is extracting as much information as possible from the acquired data by selection of a model that has highest information. This thesis focuses on the second and third steps. The following section summarized the key findings and conclusions of each non-neural tissue experiment.

6.1. Non-neural Tissue

The first study presented in Chapter 3 investigated the theoretical information of single- and multi-compartment models of diffusion in prostate tissue and identified which model extracted the most information from the measurement data. Eleven models, including different combinations of isotropic, anisotropic and restricted components, were tested. Models were ranked using AIC [196]. This study used high SNR data obtained by imaging four whole formalin-fixed prostates on a 9.4T MRI system. A range of acquisition parameters including voxel size, b -value and diffusion time was used.

In all four prostates, multi-component anisotropic and restricted models extracted more information from the multi- b and multi- Δ measurement data than single-component (ADC and DTI) models and multi-component unrestricted models. The rankings of models are largely independent of maximum b -value, maximum diffusion time, and voxel volume over the range tested in this study. Multi-component models that included anisotropic components generally ranked higher than models that did not. In addition, multi-component models that included a restricted component generally ranked higher than unrestricted models. Taken together, these results suggest that both anisotropic and restricted components are necessary for accurately describing DWI signals in prostate tissue. These findings provide further information about the non-perfusion components of the VERDICT model previously used for prostate in vivo [42] and demonstrate that appropriate DWI measurements can probe multiple tissue structure features. This study also highlights the limitations of ADC and DTI models. Most of work described in this study was published in *NMR in Biomedicine*, title “Information-based ranking of 10 compartment models of diffusion-weighted signal attenuation in fixed prostate tissue” [216].

The first study shows that the highest three AIC-ranked models in four prostates are Ball-stick-sphere, Zeppelin-sphere and Tensor-sphere, all of which include both anisotropic and restricted components. Zeppelin-sphere model is less parameterized than the other two models. The second study reported in Chapter 4 used the Zeppelin-sphere model to predict the impact of diffusion time on MD and FA. Then this predicted impact was compared with the impact assessed from the measurement data. This experiment performed diffusion tensor imaging of three formalin-fixed prostates at 9.4T

with a wide range of diffusion times (10 – 120 ms). Measured MD and FA were calculated from DTI measurement data. The Zeppelin-sphere model was used to synthesize noise-free DTI data for each diffusion time. Predicted MD and FA were then calculated from the synthetic DTI data.

In all three prostates, the diffusion time dependence of measured MD and FA was observed for the 10 – 120 ms diffusion times. There was a general decrease in the mean voxel MD and a broad increase in the mean voxel FA as diffusion time increased. The Zeppelin-sphere model accurately predicted the impact of diffusion time on MD and FA. This accurate prediction validated the Zeppelin-sphere model, which described DWI signals in prostate tissue as a sum of two signals respectively from an anisotropic Gaussian component (zeppelin) and an isotropic restricted component (sphere). Diffusion time is an important parameter but is rarely reported explicitly in clinical DWI studies. The diffusion time dependence of MD and FA found in this experiment highlight the importance of considering and reporting diffusion time in clinical DWI studies and consensus methods.

The third experiment reported in Chapter 5 investigated compartment models of diffusion in breast, lymph node, and spheroids. The eleven models tested in Chapter 3 were used for modeling diffusion in breast tissue and lymph nodes. It was assumed that diffusivity of spheroids was the same in all directions. So three isotropic models (Ball, Bi-ball, and Ball-sphere) were used for modeling diffusion in spheroids. Models were ranked using AIC [196].

In breast, lymph nodes and spheroids, multi-component restricted models extract more information from multi- b and multi- Δ measurement data than single-component models and multi-component unrestricted models. These results highlight the importance of inclusion of a restricted diffusion compartment in modelling of diffusion in these three types of non-neural tissue. In breast gland lobules, multi-component restricted and anisotropic models had highest information. The high AIC ranking of these restricted and anisotropic models is consistent with the presence of distinct diffusion microenvironment in breast gland lobules. Development of clinical DWI methods sensitive to changes in these microenvironments may be the key to increased accuracy of breast cancer detection. In cultured epithelial spheroids, the two-component isotropic and restricted model returns the mean sphere radius consistent with known cell diameter.

Epithelia are important tissue structures as many cancers are of epithelial origin. Cultured epithelial cell spheroids demonstrate many of the physiological properties of glandular epithelia and provide a well-controlled environment for studying these tissue properties. Thus, investigation of diffusion dynamics in spheroids will enhance understanding of the tissue microstructure properties that may contribute to the reported low water mobility in prostate [118] and breast [160].

6.2. Advances in Knowledge

This study made the following main advances in knowledge:

- Multi-component models including both anisotropic and restricted components extracted more information from multi- Δ , multi- b DWI measurement data in prostate tissue ex vivo than single-component (ADC and DTI) models and multi-component models that did not account for restricted diffusion.
- Model ranking trends in prostate tissue were largely independent of voxel size, maximum b -value, and maximum diffusion time over the range tested in this study.
- A diffusion time dependence of MD and FA in prostate tissue ex vivo was observed. Two-component anisotropic and restricted (Zeppelin-sphere) model accurately predicted the impact of diffusion time on MD and FA over a range of 10 – 120 ms diffusion times.
- Multi-component models that accounted for restricted diffusion extracted the most information from multi- Δ , multi- b DWI measurement data in breast tissue ex vivo including gland lobule, interlobular stroma, and fat.
- In glandular breast tissue, multi-component restricted and anisotropic models extracted more information from multi- Δ , multi- b DWI measurement data than single-component models, the isotropic restricted model and multi-component models that did not account for restricted diffusion.
- Two-component isotropic and restricted model extracted more information from multi- Δ , multi- b DWI measurement data in formalin-fixed DLD-1 spheroids than ADC/Ball and biexponential/Bi-ball models.

- In spheroids, the mean sphere radius from the isotropic and restricted model was 10.9 μm which was consistent with the known cell size.
- Multi-component models that accounted for restricted diffusion extracted more information from multi- Δ , multi- b DWI measurement data in lymph nodes ex vivo than single-component (ADC and DTI) models and multi-component unrestricted models

Overall, this study provided further information about the diffusion (non-perfusion) environments of four types of non-neural tissue (prostate, breast, lymph nodes, and spheroids). Preliminary microimaging studies of fixed prostate and breast tissue have demonstrated that epithelium has lower diffusivity and lower anisotropy than the adjacent supporting stroma [55,117,118,160]. In both prostate and glandular breast tissue, multi-component models incorporating an isotropic restricted component and an anisotropic Gaussian component extracted the most information from multi- Δ , multi- b DWI measurement data. These results strongly suggest that the isotropic restricted and anisotropic unrestricted water pools identified in diffusion analyses correspond to epithelium and stroma respectively. This possibility needs further investigation. The zeppelin-sphere model accurately predicted the impact of diffusion time on MD and FA. This result provides an independent validation of two-component anisotropic and restricted models used for describing the diffusion environments in prostate tissue. The application of Zeppelin-sphere model for predicting the influence of diffusion time proposes a new way of using and validating compartment models. In cultured epithelial cell spheroids, two-component isotropic and restricted model had highest information in the majority of selected voxels and the mean sphere radius was consistent with known cell diameter. These findings support the possibility that an isotropic restricted water pool corresponds to the epithelium. The high AIC ranking of multi-component restricted models in lymph nodes suggests the presence of restricted diffusion in one water pool. In lymph node DWI, the biophysical basis for diffusion contrast in tissue is poorly understood. Diffusion microimaging studies of lymph nodes are required to develop a clear understanding of the tissue microstructure properties that affect diffusion contrast. The results presented in this study provide basic science evidence to guide future development of clinical imaging methods.

6.3. Future Work

A previous study of prostate tissue in vivo utilizing a three-component VERDICT model used only isotropic components [42]. The study of prostate tissue ex vivo in Chapter 3 addressed this limitation by including anisotropic components and demonstrated that multi-component models, incorporating an anisotropic Gaussian component and an isotropic restricted component, had the highest information. The VERDICT model that uses an anisotropic Gaussian component to characterize water diffusion in extracellular-extravascular space needs to be tested on prostate tissue in vivo.

The eleven models tested in this thesis assumed no water exchange between compartments. The multi-component restricted models have consistently had higher information in all four types of tissue than single-component model and multi-component unrestricted models. Future work will define multi-component restricted models that account for water exchange between compartments and test these new models on the four types of tissue.

Due to the small number of non-neural tissue samples included in this study, the quantitative assessment of models for cancer detection was not made. A large number of tissue samples are required to evaluate the diagnostic performance of the models tested in this study for cancer imaging.

In this study, DWI signals were normalized to the ' $b = 0$ ' signal before model fitting to minimize T_2 effects. Previous prostate studies [199,200] demonstrated that prostatic T_2 decay was biexponential, indicating the presence of two water pools with distinct T_2 values. The existence of different T_2 components in prostate tissue may have an effect on the distinct water pools identified in diffusion analyses. There is evidence that the fast and slow diffusing water pools identified in tumour cell spheroids have significantly different T_2 relaxation rates [171]. A recent study extended three-component models of diffusion in white matter to account for T_2 effects [24]. Future work will investigate compartment models that incorporate T_2 effects (probably in a similar way to [24]).

The candidate models tested in this study were selected using a high SNR information-rich measurement with multiple diffusion time and a wide range of b -values. However,

it remains unknown whether a noisier less rich clinical data set still broadly supports candidate models chosen using a high SNR information rich measurement. The influence of measurement richness on the AIC ranking of models needs to be investigated.

References

1. Moseley M, Kucharczyk J, Mintorovitch J, Cohen Y, Kurhanewicz J, Derugin N, Asgari H, Norman D. Diffusion-weighted MR imaging of acute stroke: correlation with T2-weighted and magnetic susceptibility-enhanced MR imaging in cats. *American Journal of Neuroradiology* 1990; 11(3): 423-429.
2. Mintorovitch J, Moseley M, Chileuitt L, Shimizu H, Cohen Y, Weinstein P. Comparison of diffusion-and T2-weighted MRI for the early detection of cerebral ischemia and reperfusion in rats. *Magnetic resonance in medicine* 1991; 18(1): 39-50.
3. Moseley M, Cohen Y, Mintorovitch J, Chileuitt L, Shimizu H, Kucharczyk J, Wendland M, Weinstein P. Early detection of regional cerebral ischemia in cats: comparison of diffusion-and T2-weighted MRI and spectroscopy. *Magnetic resonance in medicine* 1990; 14(2): 330-346.
4. Dickinson L, Ahmed HU, Allen C, Barentsz JO, Carey B, Futterer JJ, Heijmink SW, Hoskin PJ, Kirkham A, Padhani AR. Magnetic resonance imaging for the detection, localisation, and characterisation of prostate cancer: recommendations from a European consensus meeting. *European urology* 2011; 59(4): 477-494.
5. Kirkham A, Haslam P, Keanie J, McCafferty I, Padhani A, Punwani S, Richenberg J, Rottenberg G, Sohaib A, Thompson P. Prostate MRI: who, when, and how? Report from a UK consensus meeting. *Clinical radiology* 2013; 68(10): 1016-1023.
6. Kul S, Cansu A, Alhan E, Dinc H, Gunes G, Reis A. Contribution of diffusion-weighted imaging to dynamic contrast-enhanced MRI in the characterization of breast tumors. *American Journal of Roentgenology* 2011; 196(1): 210-217.
7. El Khouli RH, Jacobs MA, Mezban SD, Huang P, Kamel IR, Macura KJ, Bluemke DA. Diffusion-weighted Imaging Improves the Diagnostic Accuracy of Conventional 3.0-T Breast MR Imaging. *Radiology* 2010; 256(1): 64-73.

8. Le Bihan D, Iima M. Diffusion magnetic resonance imaging: what water tells us about biological tissues. *PLoS Biol* 2015; 13(7): e1002203.
9. Padhani AR, Liu G, Mu-Koh D, Chenevert TL, Thoeny HC, Takahara T, Dzik-Jurasz A, Ross BD, Van Cauteren M, Collins D. Diffusion-weighted magnetic resonance imaging as a cancer biomarker: consensus and recommendations. *Neoplasia* 2009; 11(2): 102-125.
10. Mulkern RV, Barnes AS, Haker SJ, Hung YP, Rybicki FJ, Maier SE, Tempany CM. Biexponential characterization of prostate tissue water diffusion decay curves over an extended b-factor range. *Magnetic resonance imaging* 2006; 24(5): 563-568.
11. Shinmoto H, Oshio K, Tanimoto A, Higuchi N, Okuda S, Kuribayashi S, Mulkern RV. Biexponential apparent diffusion coefficients in prostate cancer. *Magnetic resonance imaging* 2009; 27(3): 355-359.
12. Tamura T, Usui S, Murakami S, Arihiro K, AKIYAMA Y, Naito K, Akiyama M. Biexponential signal attenuation analysis of diffusion-weighted imaging of breast. *Magnetic Resonance in Medical Sciences* 2010; 9(4): 195-207.
13. Jensen J, Helpert J. MRI quantification of non-Gaussian water diffusion by kurtosis analysis. *NMR in Biomedicine* 2010; 23(7): 698-710.
14. Jensen J, Helpert J, Ramani A, Lu H, Kaczynski K. Diffusional kurtosis imaging: the quantification of non-Gaussian water diffusion by means of magnetic resonance imaging. *Magnetic Resonance in Medicine* 2005; 53(6): 1432–1440.
15. Bennett KM, Schmainda KM, Rowe DB, Lu H, Hyde JS. Characterization of continuously distributed cortical water diffusion rates with a stretched-exponential model. *Magnetic resonance in medicine* 2003; 50(4): 727-734.
16. Basser PJ, Mattiello J, LeBihan D. MR diffusion tensor spectroscopy and imaging. *Biophysical journal* 1994; 66(1): 259-267.

17. Alexander DC. A general framework for experiment design in diffusion MRI and its application in measuring direct tissue-microstructure features. *Magnetic Resonance in Medicine* 2008; 60(2): 439-448.
18. Assaf Y, Basser PJ. Composite hindered and restricted model of diffusion (CHARMED) MR imaging of the human brain. *Neuroimage* 2005; 27(1): 48-58.
19. Assaf Y, Blumenfeld-Katzir T, Yovel Y, Basser PJ. AxCaliber: a method for measuring axon diameter distribution from diffusion MRI. *Magnetic Resonance in Medicine* 2008; 59(6): 1347-1354.
20. Barazany D, Basser PJ, Assaf Y. In vivo measurement of axon diameter distribution in the corpus callosum of rat brain. *Brain* 2009; 132(5): 1210-1220.
21. Alexander DC, Hubbard PL, Hall MG, Moore EA, Ptito M, Parker GJ, Dyrby TB. Orientationally invariant indices of axon diameter and density from diffusion MRI. *Neuroimage* 2010; 52(4): 1374-1389.
22. Zhang H, Schneider T, Wheeler-Kingshott CA, Alexander DC. NODDI: practical in vivo neurite orientation dispersion and density imaging of the human brain. *Neuroimage* 2012; 61(4): 1000-1016.
23. Panagiotaki E, Schneider T, Siow B, Hall MG, Lythgoe MF, Alexander DC. Compartment models of the diffusion MR signal in brain white matter: a taxonomy and comparison. *Neuroimage* 2012; 59(3): 2241-2254.
24. Ferizi U, Schneider T, Witzel T, Wald LL, Zhang H, Wheeler-Kingshott CA, Alexander DC. White matter compartment models for in vivo diffusion MRI at 300mT/m. *NeuroImage* 2015; 118: 468-483.
25. Ferizi U, Schneider T, Panagiotaki E, Nedjati-Gilani G, Zhang H, Wheeler-Kingshott CA, Alexander DC. A ranking of diffusion MRI compartment models with in vivo human brain data. *Magnetic resonance in medicine* 2014; 72(6): 1785-1792.
26. Wang XZ, Wang B, Gao ZQ, Liu JG, Liu ZQ, Niu QL, Sun ZK, Yuan YX. Diffusion-weighted imaging of prostate cancer: Correlation between apparent

- diffusion coefficient values and tumor proliferation. *Journal of Magnetic Resonance Imaging* 2009; 29(6): 1360-1366.
27. Zelhof B, Pickles M, Liney G, Gibbs P, Rodrigues G, Kraus S, Turnbull L. Correlation of diffusion-weighted magnetic resonance data with cellularity in prostate cancer. *BJU international* 2009; 103(7): 883-888.
 28. Tamura C, Shinmoto H, Soga S, Okamura T, Sato H, Okuaki T, Pang Y, Kosuda S, Kaji T. Diffusion kurtosis imaging study of prostate cancer: preliminary findings. *Journal of Magnetic Resonance Imaging* 2014; 40(3): 723-729.
 29. Ueda Y, Takahashi S, Ohno N, Kyotani K, Kawamitsu H, Miyati T, Aoyama N, Ueno Y, Kitajima K, Kawakami F. Triexponential function analysis of diffusion-weighted MRI for diagnosing prostate cancer. *Journal of Magnetic Resonance Imaging* 2016; 43(1): 138-148.
 30. Liu X, Zhou L, Peng W, Wang H, Zhang Y. Comparison of stretched-exponential and monoexponential model diffusion-weighted imaging in prostate cancer and normal tissues. *Journal of Magnetic Resonance Imaging* 2015; 42(4): 1078-1085.
 31. Hatakenaka M, Soeda H, Yabuuchi H, Matsuo Y, Kamitani T, Oda Y, Tsuneyoshi M, Honda H. Apparent diffusion coefficients of breast tumors: clinical application. *Magnetic Resonance in Medical Sciences* 2008; 7(1): 23-29.
 32. Marini C, Iaconi C, Giannelli M, Cilotti A, Moretti M, Bartolozzi C. Quantitative diffusion-weighted MR imaging in the differential diagnosis of breast lesion. *European radiology* 2007; 17(10): 2646-2655.
 33. Partridge SC, Murthy RS, Ziadloo A, White SW, Allison KH, Lehman CD. Diffusion tensor magnetic resonance imaging of the normal breast. *Magnetic resonance imaging* 2010; 28(3): 320-328.
 34. Perrone A, Guerrisi P, Izzo L, D'Angeli I, Sassi S, Mele LL, Marini M, Mazza D, Marini M. Diffusion-weighted MRI in cervical lymph nodes: differentiation between benign and malignant lesions. *European journal of radiology* 2011; 77(2): 281-286.

35. Holzapfel K, Duetsch S, Fauser C, Eiber M, Rummeny EJ, Gaa J. Value of diffusion-weighted MR imaging in the differentiation between benign and malignant cervical lymph nodes. *European journal of radiology* 2009; 72(3): 381-387.
36. Xing H, Song C-l, Li W-j. Meta analysis of lymph node metastasis of breast cancer patients: Clinical value of DWI and ADC value. *European Journal of Radiology* 2016; 85(6): 1132-1137.
37. Liu X, Zhou L, Peng W, Wang C, Wang H. Differentiation of central gland prostate cancer from benign prostatic hyperplasia using monoexponential and biexponential diffusion-weighted imaging. *Magnetic Resonance Imaging* 2013; 31(8): 1318-1324.
38. Toivonen J, Merisaari H, Pesola M, Taimen P, Boström PJ, Pahikkala T, Aronen HJ, Jambor I. Mathematical models for diffusion-weighted imaging of prostate cancer using b values up to 2000 s/mm²: correlation with Gleason score and repeatability of region of interest analysis. *Magnetic Resonance in Medicine* 2015; 74(4): 1116-1124.
39. Bourne RM, Panagiotaki E, Bongers A, Sved P, Watson G, Alexander DC. Information theoretic ranking of four models of diffusion attenuation in fresh and fixed prostate tissue ex vivo. *Magnetic resonance in medicine* 2014; 72(5): 1418-1426.
40. Hall MG, Bongers A, Sved P, Watson G, Bourne RM. Assessment of non-Gaussian diffusion with singly and doubly stretched biexponential models of DWI signal attenuation in prostate tissue. *NMR in Biomedicine* 2015; 28(4): 486-495.
41. Panagiotaki E, Walker-Samuel S, Siow B, Johnson SP, Rajkumar V, Pedley RB, Lythgoe MF, Alexander DC. Noninvasive quantification of solid tumor microstructure using VERDICT MRI. *Cancer research* 2014; 74(7): 1902-1912.
42. Panagiotaki E, Chan RW, Dikaios N, Ahmed HU, O'Callaghan J, Freeman A, Atkinson D, Punwani S, Hawkes DJ, Alexander DC. Microstructural characterization of normal and malignant human prostate tissue with vascular,

- extracellular, and restricted diffusion for cytometry in tumours magnetic resonance imaging. *Investigative Radiology* 2015; 50(4): 218-227.
43. Panagiotaki E, Chan R, Johnston E, Ahmed H, Atkinson D. Optimised VERDICT MRI protocol for prostate cancer characterisation. Proceedings of the 23rd Annual Meeting ISMRM. Toronto, Canada; 2015. p 2872.
 44. Stejskal EO, Tanner JE. Spin diffusion measurements: spin echoes in the presence of a time-dependent field gradient. *The journal of chemical physics* 1965; 42(1): 288-292.
 45. Sánchez-González J, Lafuente-Martínez J. Diffusion-Weighted Imaging: Acquisition and Biophysical Basis. *Diffusion MRI Outside the Brain*: Springer; 2012. p 1-15.
 46. Alberts B, Bray D, Lewis J, Raff M, Roberts K, Watson JD. *Molecular Biology of the Cell* (3rd edition): Taylor&Francis Inc, US; 1994.
 47. Crick F. Diffusion in embryogenesis. *Nature* 1970; 225: 420-422.
 48. Finkelstein A. Water movement through lipid bilayer, pores and plasma membranes: Wiley-Interscience, US; 1987.
 49. Bihan DL. Molecular diffusion, tissue microdynamics and microstructure. *NMR in Biomedicine* 1995; 8(7): 375-386.
 50. Price WS. Pulsed-field gradient nuclear magnetic resonance as a tool for studying translational diffusion: Part 1. Basic theory. *Concepts in magnetic resonance* 1997; 9(5): 299-336.
 51. Le Bihan D. Magnetic resonance diffusion imaging: introduction and concepts. *Diffusion MRI: Theory, Methods, and Applications* University Press, Oxford 2011; 66-69.
 52. Syková E, Nicholson C. Diffusion in brain extracellular space. *Physiological reviews* 2008; 88(4): 1277-1340.

53. Chenevert TL, Brunberg JA, Pipe JG. Anisotropic diffusion in human white matter: demonstration with MR techniques in vivo. *Radiology* 1990; 177(2): 401-405.
54. Assaf Y, Pasternak O. Diffusion tensor imaging (DTI)-based white matter mapping in brain research: a review. *Journal of molecular neuroscience* 2008; 34(1): 51-61.
55. Bourne RM, Kurniawan N, Cowin G, Sved P, Watson G. Microscopic diffusion anisotropy in formalin fixed prostate tissue: preliminary findings. *Magnetic resonance in medicine* 2012; 68(6): 1943-1948.
56. Bourne RM, Bongers A, Chatterjee A, Sved P, Watson G. Diffusion anisotropy in fresh and fixed prostate tissue ex vivo. *Magnetic Resonance in Medicine* 2015; 76(2): 626-634.
57. Notohamiprodjo M, Glaser C, Herrmann KA, Dietrich O, Attenberger UI, Reiser MF, Schoenberg SO, Michaely HJ. Diffusion tensor imaging of the kidney with parallel imaging: initial clinical experience. *Investigative radiology* 2008; 43(10): 677-685.
58. Rohmer D, Sitek A, Gullberg GT. Reconstruction and visualization of fiber and laminar structure in the normal human heart from ex vivo diffusion tensor magnetic resonance imaging (DTMRI) data. *Investigative radiology* 2007; 42(11): 777-789.
59. Moseley ME. Anisotropic solvent translational diffusion in solutions of poly (γ -benzyl-L-glutamate). *The Journal of Physical Chemistry* 1983; 87(1): 18-20.
60. Bourne R. The trouble with apparent diffusion coefficient papers. *Journal of Medical Radiation Sciences* 2015; 62(2): 89-91.
61. Shepherd TM, Thelwall PE, Stanisz GJ, Blackband SJ. Aldehyde fixative solutions alter the water relaxation and diffusion properties of nervous tissue. *Magnetic resonance in medicine* 2009; 62(1): 26-34.
62. Thelwall PE, Grant SC, Stanisz GJ, Blackband SJ. Human erythrocyte ghosts: exploring the origins of multiexponential water diffusion in a model biological

- tissue with magnetic resonance. *Magnetic resonance in medicine* 2002; 48(4): 649-657.
63. Forder JR, Buckley DL, Blackband SJ, Bui JD. MR imaging measurement of compartmental water diffusion in perfused heart slices. *American Journal of Physiology - Heart and Circulatory Physiology* 2001; 281(3): H1280-H1285.
 64. Sehy JV, Ackerman JJ, Neil JJ. Evidence that both fast and slow water ADC components arise from intracellular space. *Magnetic resonance in medicine* 2002; 48(5): 765-770.
 65. Rosenkrantz AB, Sigmund EE, Johnson G, Babb JS, Mussi TC, Melamed J, Taneja SS, Lee VS, Jensen JH. Prostate cancer: feasibility and preliminary experience of a diffusional kurtosis model for detection and assessment of aggressiveness of peripheral zone cancer. *Radiology* 2012; 264(1): 126-135.
 66. Nogueira L, Brandão S, Matos E, Nunes RG, Loureiro J, Ramos I, Ferreira HA. Application of the diffusion kurtosis model for the study of breast lesions. *European radiology* 2014; 24(6): 1197-1203.
 67. Pfeuffer J, Provencher SW, Gruetter R. Water diffusion in rat brain in vivo as detected at very large b values is multicompartmental. *Magnetic Resonance Materials in Physics, Biology and Medicine* 1999; 8(2): 98-108.
 68. Assaf Y, Cohen Y. Non-mono-exponential attenuation of water and n-acetyl aspartate signals due to diffusion in brain tissue. *Journal of Magnetic Resonance* 1998; 131(1): 69-85.
 69. Behrens T, Woolrich M, Jenkinson M, Johansen-Berg H, Nunes R, Clare S, Matthews P, Brady J, Smith S. Characterization and propagation of uncertainty in diffusion-weighted MR imaging. *Magnetic resonance in medicine* 2003; 50(5): 1077-1088.
 70. Stanisz GJ, Wright GA, Henkelman RM, Szafer A. An analytical model of restricted diffusion in bovine optic nerve. *Magnetic Resonance in Medicine* 1997; 37(1): 103-111.

71. Sen PN, Basser PJ. A model for diffusion in white matter in the brain. *Biophys J* 2005; 89(5): 2927-2938.
72. Le Bihan D, Breton E, Lallemand D, Aubin M, Vignaud J, Laval-Jeantet M. Separation of diffusion and perfusion in intravoxel incoherent motion MR imaging. *Radiology* 1988; 168(2): 497-505.
73. Le Bihan D, Breton E, Lallemand D, Grenier P, Cabanis E, Laval-Jeantet M. MR imaging of intravoxel incoherent motions: application to diffusion and perfusion in neurologic disorders. *Radiology* 1986; 161(2): 401-407.
74. Shinmoto H, Tamura C, Soga S, Shiomi E, Yoshihara N, Kaji T, Mulkern RV. An intravoxel incoherent motion diffusion-weighted imaging study of prostate cancer. *American Journal of Roentgenology* 2012; 199(4): W496-W500.
75. Sigmund E, Cho G, Kim S, Finn M, Moccaldi M, Jensen J, Sodickson D, Goldberg J, Formenti S, Moy L. Intravoxel incoherent motion imaging of tumor microenvironment in locally advanced breast cancer. *Magnetic resonance in medicine* 2011; 65(5): 1437-1447.
76. Chandarana H, Kang SK, Wong S, Rusinek H, Zhang JL, Arizono S, Huang WC, Melamed J, Babb JS, Suan EF. Diffusion-weighted intravoxel incoherent motion imaging of renal tumors with histopathologic correlation. *Investigative radiology* 2012; 47(12): 688-696.
77. Shah RB, Zhou M. Anatomy and Normal Histology of the Prostate Pertinent to Biopsy Practice. *Prostate Biopsy Interpretation: An Illustrated Guide: Springer*; 2012. p 1-10.
78. Weinreb JC, Barentsz JO, Choyke PL, Cornud F, Haider MA, Macura KJ, Margolis D, Schnall MD, Shtern F, Tempany CM. PI-RADS prostate imaging-reporting and data system: 2015, version 2. *European urology* 2016; 69(1): 16-40.
79. Shah RB, Zhou M. *Prostate biopsy interpretation: An illustrated guide: Springer Science & Business Media, New York*; 2011.

80. El-Alfy M, Pelletier G, Hermo LS, Labrie F. Unique features of the basal cells of human prostate epithelium. *Microscopy research and technique* 2000; 51(5): 436-446.
81. Bostwick DG. The pathology of early prostate cancer. *CA: a cancer journal for clinicians* 1989; 39(6): 376-393.
82. Epstein JI, Allsbrook Jr WC, Amin MB, Egevad LL, Committee IG. The 2005 International Society of Urological Pathology (ISUP) consensus conference on Gleason grading of prostatic carcinoma. *The American journal of surgical pathology* 2005; 29(9): 1228-1242.
83. ACIM (Australian Cancer Incidence and Mortality) Books: Australian Institute of Health and Welfare 2015.
84. Ilic D, O'Connor D, Green S, Wilt TJ. Screening for prostate cancer: an updated Cochrane systematic review. *BJU international* 2011; 107(6): 882-891.
85. Ouzzane A, Puech P, Lemaitre L, Leroy X, Nevoux P, Betrouni N, Haber G-P, Villers A. Combined multiparametric MRI and targeted biopsies improve anterior prostate cancer detection, staging, and grading. *Urology* 2011; 78(6): 1356-1362.
86. Barentsz JO, Richenberg J, Clements R, Choyke P, Verma S, Villeirs G, Rouviere O, Logager V, Fütterer JJ. ESUR prostate MR guidelines 2012. *European radiology* 2012; 22(4): 746-757.
87. Riches S, Vanas N, Morgan V, Ashley S, Fisher C, Payne G, Parker C. Diffusion-weighted magnetic resonance imaging: a potential non-invasive marker of tumour aggressiveness in localized prostate cancer. *Clinical radiology* 2008; 63(7): 774-782.
88. Isebaert S, Van den Bergh L, Haustermans K, Joniau S, Lerut E, De Wever L, De Keyzer F, Budiharto T, Slagmolen P, Van Poppel H. Multiparametric MRI for prostate cancer localization in correlation to whole-mount histopathology. *Journal of Magnetic Resonance Imaging* 2013; 37(6): 1392-1401.

89. Tamada T, Sone T, Jo Y, Toshimitsu S, Yamashita T, Yamamoto A, Tanimoto D, Ito K. Apparent diffusion coefficient values in peripheral and transition zones of the prostate: comparison between normal and malignant prostatic tissues and correlation with histologic grade. *Journal of Magnetic Resonance Imaging* 2008; 28(3): 720-726.
90. Pickles MD, Gibbs P, Sreenivas M, Turnbull LW. Diffusion-weighted imaging of normal and malignant prostate tissue at 3.0 T. *Journal of magnetic resonance imaging* 2006; 23(2): 130-134.
91. Langer DL, van der Kwast TH, Evans AJ, Plotkin A, Trachtenberg J, Wilson BC, Haider MA. Prostate tissue composition and MR measurements: investigating the relationships between ADC, T2, K trans, ve, and corresponding histologic features 1. *Radiology* 2010; 255(2): 485-494.
92. Gibbs P, Liney GP, Pickles MD, Zelhof B, Rodrigues G, Turnbull LW. Correlation of ADC and T2 measurements with cell density in prostate cancer at 3.0 Tesla. *Investigative radiology* 2009; 44(9): 572-576.
93. Oto A, Yang C, Kayhan A, Tretiakova M, Antic T, Schmid-Tannwald C, Eggener S, Karczmar GS, Stadler WM. Diffusion-weighted and dynamic contrast-enhanced MRI of prostate cancer: correlation of quantitative MR parameters with Gleason score and tumor angiogenesis. *AJR American journal of roentgenology* 2011; 197(6): 1382-1390.
94. Hambrock T, Somford DM, Huisman HJ, van Oort IM, Witjes JA, Hulsbergen-van de Kaa CA, Scheenen T, Barentsz JO. Relationship between Apparent Diffusion Coefficients at 3.0-T MR Imaging and Gleason Grade in Peripheral Zone Prostate Cancer. *Radiology* 2011; 259(2): 453-461.
95. Riches S, Hawtin K, Charles-Edwards E, De Souza N. Diffusion-weighted imaging of the prostate and rectal wall: comparison of biexponential and monoexponential modelled diffusion and associated perfusion coefficients. *NMR in Biomedicine* 2009; 22(3): 318-325.

96. Kim CK, Park BK, Han JJ, Kang TW, Lee HM. Diffusion-weighted imaging of the prostate at 3 T for differentiation of malignant and benign tissue in transition and peripheral zones: preliminary results. *Journal of computer assisted tomography* 2007; 31(3): 449-454.
97. Kuru TH, Roethke MC, Stieltjes B, Maier-Hein K, Schlemmer H-P, Hadaschik BA, Fenchel M. Intravoxel incoherent motion (IVIM) diffusion imaging in prostate cancer-what does it add? *Journal of computer assisted tomography* 2014; 38(4): 558-564.
98. Döpfert J, Lemke A, Weidner A, Schad LR. Investigation of prostate cancer using diffusion-weighted intravoxel incoherent motion imaging. *Magnetic resonance imaging* 2011; 29(8): 1053-1058.
99. Valerio M, Zini C, Fierro D, Giura F, Colarieti A, Giuliani A, Laghi A, Catalano C, Panebianco V. 3T multiparametric MRI of the prostate: Does intravoxel incoherent motion diffusion imaging have a role in the detection and stratification of prostate cancer in the peripheral zone? *European journal of radiology* 2016; 85(4): 790-794.
100. Ocak I, Bernardo M, Metzger G, Barrett T, Pinto P, Albert PS, Choyke PL. Dynamic contrast-enhanced MRI of prostate cancer at 3 T: a study of pharmacokinetic parameters. *American Journal of Roentgenology* 2007; 189(4): W192-W201.
101. McDonald DM, Choyke PL. Imaging of angiogenesis: from microscope to clinic. *Nature medicine* 2003; 9(6): 713-725.
102. Pang Y, Turkbey B, Bernardo M, Kruecker J, Kadoury S, Merino MJ, Wood BJ, Pinto PA, Choyke PL. Intravoxel incoherent motion MR imaging for prostate cancer: An evaluation of perfusion fraction and diffusion coefficient derived from different b-value combinations. *Magnetic resonance in medicine* 2013; 69(2): 553-562.
103. Roethke MC, Kuder TA, Kuru TH, Fenchel M, Hadaschik BA, Laun FB, Schlemmer H-P, Stieltjes B. Evaluation of diffusion kurtosis imaging versus

- standard diffusion imaging for detection and grading of peripheral zone prostate cancer. *Investigative radiology* 2015; 50(8): 483-489.
104. Manenti G, Carlini M, Mancino S, Colangelo V, Di Roma M, Squillaci E, Simonetti G. Diffusion Tensor Magnetic Resonance Imaging of Prostate Cancer. *Investigative Radiology* 2007; 42(6): 412-419.
 105. Gibbs P, Pickles MD, Turnbull LW. Diffusion Imaging of the Prostate at 3.0 Tesla. *Investigative Radiology* 2006; 41(2): 185-188.
 106. Gürses B, Tasdelen N, Yencilek F, Kılıckesmez NO, Alp T, Fırat Z, Albayrak MS, Uluğ AM, Gürmen AN. Diagnostic utility of DTI in prostate cancer. *European Journal of Radiology* 2011; 79(2): 172-176.
 107. Moradi M, Salcudean SE, Chang SD, Jones EC, Buchan N, Casey RG, Goldenberg SL, Kozlowski P. Multiparametric MRI maps for detection and grading of dominant prostate tumors. *Journal of Magnetic Resonance Imaging* 2012; 35(6): 1403-1413.
 108. Haker SJ, Barnes AS, Maier SE, Tempany CM, Mulkern RV. Diffusion tensor imaging for prostate cancer detection: preliminary results from a biopsy-based assessment. *Proceedings of the 13th Annual Meeting of ISMRM. Miami Beach, Florida, USA; 2005. p 2126.*
 109. Gürses B, Kabakci N, Kovanlikaya A, Fırat Z, Bayram A, Uluğ AM, Kovanlikaya İ. Diffusion tensor imaging of the normal prostate at 3 Tesla. *European Radiology* 2008; 18(4): 716-721.
 110. Quentin M, Pentang G, Schimmöller L, Kott O, Müller-Lutz A, Blondin D, Arsov C, Hiester A, Rabenalt R, Wittsack H-J. Feasibility of diffusional kurtosis tensor imaging in prostate MRI for the assessment of prostate cancer: preliminary results. *Magnetic resonance imaging* 2014; 32(7): 880-885.
 111. Uribe CF, Jones EC, Chang SD, Goldenberg SL, Reinsberg SA, Kozlowski P. In vivo 3T and ex vivo 7T diffusion tensor imaging of prostate cancer: correlation with histology. *Magnetic Resonance Imaging* 2015; 33(5): 577-583.

112. Reinsberg S, Brewster J, Payne G, Leach M, deSouza N. Anisotropic diffusion in prostate cancer: fact or artifact? Proceedings of the 13th Annual Meeting ISMRM. Miami, Florida, USA; 2005. p 269.
113. Xu JQ, Humphrey PA, Kibel AS, Snyder AZ, Narra VR, Ackerman JJH, Song SK. Magnetic Resonance Diffusion Characteristics of Histologically Defined Prostate Cancer in Humans. *Magnetic Resonance in Medicine* 2009; 61(4): 842-850.
114. Quentin M, Blondin D, Klasen J, Lanzman RS, Miese F-R, Arsov C, Albers P, Antoch G, Wittsack H-J. Comparison of different mathematical models of diffusion-weighted prostate MR imaging. *Magnetic resonance imaging* 2012; 30(10): 1468-1474.
115. Jambor I, Merisaari H, Taimen P, Boström P, Minn H, Pesola M, Aronen HJ. Evaluation of different mathematical models for diffusion-weighted imaging of normal prostate and prostate cancer using high b-values: A repeatability study. *Magnetic Resonance in Medicine* 2015; 73(5): 1988-1998.
116. Chatterjee A, Watson G, Myint E, Sved P, McEntee M, Bourne R. Changes in epithelium, stroma, and lumen space correlate more strongly with gleason pattern and are stronger predictors of prostate ADC changes than cellularity metrics. *Radiology* 2015; 277(3): 751-762.
117. Bourne RM, Kurniawan N, Cowin G, Stait-Gardner T, Sved P, Watson G, Price WS. Microscopic diffusivity compartmentation in formalin-fixed prostate tissue. *Magnetic resonance in medicine* 2012; 68(2): 614-620.
118. Bourne R, Kurniawan N, Cowin G, Sved P, Watson G. 16 T diffusion microimaging of fixed prostate tissue: preliminary findings. *Magnetic resonance in medicine* 2011; 66(1): 244-247.
119. Panagiotaki E, Alexander DC, Bourne R. Comparison of single and multi-compartment models of diffusion in fixed prostate tissue. Proceedings of the 21st Annual Meeting ISMRM. Salt Lake City, UT, USA; 2013. p 1798.
120. Aydiner A, Igci A, Soran A. Breast disease: Springer International Publishing, Switzerland; 2016.

121. Kuijper A, Mommers EC, van der Wall E, van Diest PJ. Histopathology of fibroadenoma of the breast. *American journal of clinical pathology* 2001; 115(5): 736-742.
122. Groh O, in't Hof K. Giant lipoma of the male breast: case report and review of literature. *European journal of plastic surgery* 2012; 35(5): 407-409.
123. Carney PA, Miglioretti DL, Yankaskas BC, Kerlikowske K, Rosenberg R, Rutter CM, Geller BM, Abraham LA, Taplin SH, Dignan M. Individual and combined effects of age, breast density, and hormone replacement therapy use on the accuracy of screening mammography. *Annals of internal medicine* 2003; 138(3): 168-175.
124. Barlow WE, Lehman CD, Zheng Y, Ballard-Barbash R, Yankaskas BC, Cutter GR, Carney PA, Geller BM, Rosenberg R, Kerlikowske K. Performance of diagnostic mammography for women with signs or symptoms of breast cancer. *Journal of the National Cancer Institute* 2002; 94(15): 1151-1159.
125. Riedl CC, Luft N, Bernhart C, Weber M, Bernathova M, Tea M-KM, Rudas M, Singer CF, Helbich TH. Triple-modality screening trial for familial breast cancer underlines the importance of magnetic resonance imaging and questions the role of mammography and ultrasound regardless of patient mutation status, age, and breast density. *Journal of Clinical Oncology* 2015; 33(10): 1128-1135.
126. Sardanelli F, Podo F, Santoro F, Manoukian S, Bergonzi S, Trecate G, Vergnaghi D, Federico M, Cortesi L, Corcione S. Multicenter surveillance of women at high genetic breast cancer risk using mammography, ultrasonography, and contrast-enhanced magnetic resonance imaging (the high breast cancer risk italian 1 study): final results. *Investigative radiology* 2011; 46(2): 94-105.
127. Pediconi F, Miglio E, Telesca M, Luciani ML, Kirchin MA, Passariello R, Catalano C. Effect of preoperative breast magnetic resonance imaging on surgical decision making and cancer recurrence rates. *Investigative radiology* 2012; 47(2): 128-135.

128. Sardanelli F, Boetes C, Borisch B, Decker T, Federico M, Gilbert FJ, Helbich T, Heywang-Köbrunner SH, Kaiser WA, Kerin MJ. Magnetic resonance imaging of the breast: recommendations from the EUSOMA working group. *European journal of cancer* 2010; 46(8): 1296-1316.
129. Pinker-Domenig K, Bogner W, Gruber S, Bickel H, Duffy S, Schernthaner M, Dubsy P, Pluschnig U, Rudas M, Trattnig S. High resolution MRI of the breast at 3 T: which BI-RADS® descriptors are most strongly associated with the diagnosis of breast cancer? *European radiology* 2012; 22(2): 322-330.
130. Kuhl CK, Schild HH, Morakkabati N. Dynamic Bilateral Contrast-enhanced MR Imaging of the Breast: Trade-off between Spatial and Temporal Resolution 1. *Radiology* 2005; 236(3): 789-800.
131. Yabuuchi H, Matsuo Y, Kamitani T, Setoguchi T, Okafuji T, Soeda H, Sakai S, Hatakenaka M, Kubo M, Tokunaga E. Non-mass-like enhancement on contrast-enhanced breast MR imaging: lesion characterization using combination of dynamic contrast-enhanced and diffusion-weighted MR images. *European journal of radiology* 2010; 75(1): e126-e132.
132. D'Orsi CJ SE, Mendelson EB, Morris EA, et al. ACR BI-RADS® Atlas, Breast Imaging Reporting and Data System. Reston, VA: American College of Radiology; 2013.
133. Dorrius MD, Dijkstra H, Oudkerk M, Sijens PE. Effect of b value and pre-admission of contrast on diagnostic accuracy of 1.5-T breast DWI: a systematic review and meta-analysis. *European radiology* 2014; 24(11): 2835-2847.
134. Partridge S, Rahbar H, Murthy R, Chai X, Kurland B, DeMartini W, Lehman C. Improved diagnostic accuracy of breast MRI through combined apparent diffusion coefficients and dynamic contrast-enhanced kinetics. *Magnetic resonance in medicine* 2011; 65(6): 1759-1767.
135. Pinker K, Bogner W, Baltzer P, Gruber S, Bickel H, Brueck B, Trattnig S, Weber M, Dubsy P, Bago-Horvath Z. Improved diagnostic accuracy with multiparametric magnetic resonance imaging of the breast using dynamic contrast-

- enhanced magnetic resonance imaging, diffusion-weighted imaging, and 3-dimensional proton magnetic resonance spectroscopic imaging. *Investigative radiology* 2014; 49(6): 421-430.
136. Pinker K, Baltzer P, Bogner W, Leithner D, Trattnig S, Zaric O, Dubsky P, Bago-Horvath Z, Rudas M, Gruber S. Multiparametric MR imaging with high-resolution dynamic contrast-enhanced and diffusion-weighted imaging at 7 T improves the assessment of Breast tumors: a feasibility study. *Radiology* 2015; 276(2): 360-370.
137. Bogner W, Pinker K, Zaric O, Baltzer P, Minarikova L, Porter D, Bago-Horvath Z, Dubsky P, Helbich TH, Trattnig S. Bilateral diffusion-weighted MR imaging of breast tumors with submillimeter resolution using readout-segmented echo-planar imaging at 7 T. *Radiology* 2014; 274(1): 74-84.
138. Baltzer A, Dietzel M, Kaiser CG, Baltzer PA. Combined reading of contrast enhanced and diffusion weighted magnetic resonance imaging by using a simple sum score. *European radiology* 2016; 26(3): 884-891.
139. Bickel H, Pinker-Domenig K, Bogner W, Spick C, Bagó-Horváth Z, Weber M, Helbich T, Baltzer P. Quantitative apparent diffusion coefficient as a noninvasive imaging biomarker for the differentiation of invasive breast cancer and ductal carcinoma in situ. *Investigative radiology* 2015; 50(2): 95-100.
140. Spick C, Bickel H, Pinker K, Bernathova M, Kapetas P, Woitek R, Clauser P, Polanec SH, Rudas M, Bartsch R. Diffusion-weighted MRI of breast lesions: a prospective clinical investigation of the quantitative imaging biomarker characteristics of reproducibility, repeatability, and diagnostic accuracy. *NMR in Biomedicine* 2016; 29(10): 1445-1453.
141. Dorrius MD, de Vries EF, Slart RH, Glaudemans AW. Breast cancer: a new imaging approach as an addition to existing guidelines. Springer; 2015.
142. Liu C, Liang C, Liu Z, Zhang S, Huang B. Intravoxel incoherent motion (IVIM) in evaluation of breast lesions: comparison with conventional DWI. *European journal of radiology* 2013; 82(12): e782-e789.

143. Cho GY, Moy L, Kim SG, Baete SH, Moccaldi M, Babb JS, Sodickson DK, Sigmund EE. Evaluation of breast cancer using intravoxel incoherent motion (IVIM) histogram analysis: comparison with malignant status, histological subtype, and molecular prognostic factors. *European radiology* 2015; 1-12.
144. Kim Y, Ko K, Kim D, Min C, Kim SG, Joo J, Park B. Intravoxel incoherent motion diffusion-weighted MR imaging of breast cancer: association with histopathological features and subtypes. *The British journal of radiology* 2016; 89(1063): 20160140.
145. Dijkstra H, Dorrius MD, Wielema M, Jaspers K, Pijnappel RM, Oudkerk M, Sijens PE. Semi-automated quantitative intravoxel incoherent motion analysis and its implementation in breast diffusion-weighted imaging. *Journal of Magnetic Resonance Imaging* 2016; 43(5): 1122-1131.
146. Bokacheva L, Kaplan JB, Giri DD, Patil S, Gnanasigamani M, Nyman CG, Deasy JO, Morris EA, Thakur SB. Intravoxel incoherent motion diffusion-weighted MRI at 3.0 T differentiates malignant breast lesions from benign lesions and breast parenchyma. *Journal of Magnetic Resonance Imaging* 2014; 40(4): 813-823.
147. Sigmund EE, Cho GY, Kim S, Finn M, Moccaldi M, Jensen JH, Sodickson DK, Goldberg JD, Formenti S, Moy L. Intravoxel incoherent motion imaging of tumor microenvironment in locally advanced breast cancer. *Magnetic Resonance in Medicine* 2011; 65(5): 1437-1447.
148. Sun K, Chen X, Chai W, Fei X, Fu C, Yan X, Zhan Y, Chen K, Shen K, Yan F. Breast cancer: diffusion kurtosis mr imaging—diagnostic accuracy and correlation with clinical-pathologic factors. *Radiology* 2015; 277(1): 46-55.
149. Wu D, Li G, Zhang J, Chang S, Hu J, Dai Y. Characterization of breast tumors using diffusion kurtosis imaging (DKI). *PloS one* 2014; 9(11): e113240.
150. Iima M, Yano K, Kataoka M, Umehana M, Murata K, Kanao S, Togashi K, Le Bihan D. Quantitative non-gaussian diffusion and intravoxel incoherent motion magnetic resonance imaging: differentiation of malignant and benign breast lesions. *Investigative radiology* 2015; 50(4): 205-211.

151. Tagliafico A, Rescinito G, Monetti F, Villa A, Chiesa F, Fisci E, Pace D, Calabrese M. Diffusion tensor magnetic resonance imaging of the normal breast: reproducibility of DTI-derived fractional anisotropy and apparent diffusion coefficient at 3.0 T. *La radiologia medica* 2012; 117(6): 992-1003.
152. Teruel JR, Goa PE, Sjøbakk TE, Østlie A, Fjøsne HE, Bathen TF. Diffusion weighted imaging for the differentiation of breast tumors: From apparent diffusion coefficient to high order diffusion tensor imaging. *Journal of Magnetic Resonance Imaging* 2016; 43(5): 1111-1121.
153. Cakir O, Arslan A, Inan N, Anik Y, Sarısoy T, Gumustas S, Akansel G. Comparison of the diagnostic performances of diffusion parameters in diffusion weighted imaging and diffusion tensor imaging of breast lesions. *European journal of radiology* 2013; 82(12): e801-e806.
154. Jiang R, Ma Z, Dong H, Sun S, Zeng X, Li X. Diffusion tensor imaging of breast lesions: evaluation of apparent diffusion coefficient and fractional anisotropy and tissue cellularity. *The British Journal of Radiology* 2016; 89(1064): 20160076.
155. Baltzer PA, Schäfer A, Dietzel M, Grässel D, Gajda M, Camara O, Kaiser WA. Diffusion tensor magnetic resonance imaging of the breast: a pilot study. *European radiology* 2011; 21(1): 1-10.
156. Partridge SC, Ziadloo A, Murthy R, White SW, Peacock S, Eby PR, DeMartini WB, Lehman CD. Diffusion tensor MRI: preliminary anisotropy measures and mapping of breast tumors. *Journal of Magnetic Resonance Imaging* 2010; 31(2): 339-347.
157. Eyal E, Shapiro-Feinberg M, Furman-Haran E, Grobgeld D, Golan T, Itzchak Y, Catane R, Papa M, Degani H. Parametric diffusion tensor imaging of the breast. *Investigative Radiology* 2012; 47(5): 284-291.
158. Tamura T, Usui S, Murakami S, Arihiro K, Fujimoto T, Yamada T, Naito K, Akiyama M. Comparisons of multi b-value DWI signal analysis with pathological specimen of breast cancer. *Magnetic resonance in medicine* 2012; 68(3): 890-897.

159. Panek R, Borri M, Orton M, O'Flynn E, Morgan V, Giles SL, Leach MO, Schmidt MA. Evaluation of diffusion models in breast cancer. *Medical physics* 2015; 42(8): 4833-4839.
160. Norddin N, Power C, Watson G, Cowin G, Kurniawan ND, Gluch L, Bourne RM. Microscopic diffusion properties of fixed breast tissue: Preliminary findings. *Magnetic resonance in medicine* 2015; 74(6): 1733-1739.
161. Yamada I, Hikishima K, Miyasaka N, Tokairin Y, Kawano T, Ito E, Kobayashi D, Eishi Y, Okano H, Shibuya H. Diffusion-tensor MRI and tractography of the esophageal wall ex vivo. *Journal of Magnetic Resonance Imaging* 2014; 40(3): 567-576.
162. Bailey C, Vinnicombe S, Panagiotaki E, Waugh SA, Hipwell JH, Whelehan P, Pinder SE, Evans AJ, Alexander DC, Hawkes DJ. Modelling vasculature and cellular restriction in breast tumours using diffusion MRI. *Proceedings of the 23rd Annual Meeting ISMRM*. Toronto, Canada; 2015. p 1082.
163. Bailey C, Siow B, Panagiotaki E, Hipwell JH, Pinder SE, Alexander DC, Hawkes DJ. Microstructure models for diffusion MRI in breast cancer and surrounding stroma: an ex vivo study. *Proceedings of the 24th Annual Meeting ISMRM*. Singapore; 2016. p 927.
164. Curcio E, Salerno S, Barbieri G, De Bartolo L, Drioli E, Bader A. Mass transfer and metabolic reactions in hepatocyte spheroids cultured in rotating wall gas-permeable membrane system. *Biomaterials* 2007; 28(36): 5487-5497.
165. Kim BJ. *Development of Multiple Fluorescent Tumour Spheroid Models To Investigate the use of Transition Metal Complexes as Hypoxia-Activated Prodrugs*. Sydney: The University of Sydney; 2014.
166. Lin RZ, Chang HY. Recent advances in three-dimensional multicellular spheroid culture for biomedical research. *Biotechnology journal* 2008; 3(9-10): 1172-1184.
167. Baal N, Widmer-Teske R, McKinnon T, Preissner KT, Zygmunt MT. In vitro spheroid model of placental vasculogenesis: does it work? *Laboratory Investigation* 2009; 89(2): 152-163.

168. Ma H-l, Jiang Q, Han S, Wu Y, Cui Tomshine J, Wang D, Gan Y, Zou G, Liang X-J. Multicellular tumor spheroids as an in vivo-like tumor model for three-dimensional imaging of chemotherapeutic and nano material cellular penetration. *Molecular imaging* 2012; 11(6): 487-498.
169. Härmä V, Virtanen J, Mäkelä R, Happonen A, Mpindi J-P, Knuuttila M, Kohonen P, Lötjönen J, Kallioniemi O, Nees M. A comprehensive panel of three-dimensional models for studies of prostate cancer growth, invasion and drug responses. *PloS one* 2010; 5(5): e10431.
170. Yamada I, Hikishima K, Miyasaka N, Kawano T, Tokairin Y, Ito E, Kobayashi D, Eishi Y, Okano H. Esophageal Carcinoma: Ex Vivo Evaluation with Diffusion-Tensor MR Imaging and Tractography at 7 T. *Radiology* 2014; 272(1): 164-173.
171. Smouha E, Neeman M. Compartmentation of intracellular water in multicellular tumor spheroids: diffusion and relaxation NMR. *Magnetic resonance in medicine* 2001; 46(1): 68-77.
172. Neeman M, Jarrett KA, Sillerud LO, Freyer JP. Self-diffusion of water in multicellular spheroids measured by magnetic resonance microimaging. *Cancer research* 1991; 51(15): 4072-4079.
173. Momot KI, Bas O, Holzapfel NP, Loessner D. Magnetic resonance microimaging of cancer cell spheroid constructs. *Biomedical Spectroscopy and Imaging* 2016; 5(1): 41-54.
174. Singh V. *Lymphatic system*: Elsevier India; 2014.
175. Blausen.com staff. *Medical gallery of Blausen Medical* 2014. *WikiJournal of Medicine* 2014; 1(2): 21.
176. Cancer Research UK. *Diagram of a lymph node*. 2014. Available at https://commons.wikimedia.org/wiki/File:Diagram_of_a_lymph_node_CRUK_022.svg
177. Olteanu H, Harrington AMD, Kroft SH. *Lymph nodes*: Demos Medical Publishing, New York; 2013.

178. Miranda RN, Khoury JD, Medeiros LJ. Atlas of lymph node pathology: Springer Science & Business Media, New York; 2013.
179. Briganti A. How to improve the ability to detect pelvic lymph node metastases of urologic malignancies. *European Urology* 2009; 55(4): 770-772.
180. Gong Y, Wang Q, Dong L, Jia Y, Hua C, Mi F, Li C. Different imaging techniques for the detection of pelvic lymph nodes metastasis from gynecological malignancies: a systematic review and meta-analysis. *Oncotarget* 2016. doi: 10.18632/oncotarget.12959
181. De Bondt R, Hoerberigs M, Nelemans P, Deserno W, Peutz-Kootstra C, Kremer B, Beets-Tan R. Diagnostic accuracy and additional value of diffusion-weighted imaging for discrimination of malignant cervical lymph nodes in head and neck squamous cell carcinoma. *Neuroradiology* 2009; 51(3): 183-192.
182. Lin G, Ho KC, Wang JJ, Ng KK, Wai YY, Chen YT, Chang CJ, Ng SH, Lai CH, Yen TC. Detection of lymph node metastasis in cervical and uterine cancers by diffusion-weighted magnetic resonance imaging at 3T. *Journal of Magnetic Resonance Imaging* 2008; 28(1): 128-135.
183. Sumi M, Sakihama N, Sumi T, Morikawa M, Uetani M, Kabasawa H, Shigeno K, Hayashi K, Takahashi H, Nakamura T. Discrimination of metastatic cervical lymph nodes with diffusion-weighted MR imaging in patients with head and neck cancer. *American Journal of Neuroradiology* 2003; 24(8): 1627-1634.
184. Kamitani T, Hatakenaka M, Yabuuchi H, Matsuo Y, Fujita N, Jinnouchi M, Nagao M, Shirahane K, Tokunaga E, Honda H. Detection of axillary node metastasis using diffusion-weighted MRI in breast cancer. *Clinical Imaging* 2013; 37(1): 56-61.
185. Sakurada A, Takahara T, Kwee TC, Yamashita T, Nasu S, Horie T, Van Cauteren M, Imai Y. Diagnostic performance of diffusion-weighted magnetic resonance imaging in esophageal cancer. *European Radiology* 2009; 19(6): 1461-1469.
186. Heijnen LA, Lambregts DM, Mondal D, Martens MH, Riedl RG, Beets GL, Beets-Tan RG. Diffusion-weighted MR imaging in primary rectal cancer staging

- demonstrates but does not characterise lymph nodes. *European radiology* 2013; 23(12): 3354-3360.
187. Nakai G, Matsuki M, Harada T, Tanigawa N, Yamada T, Barentsz J, Narumi Y. Evaluation of axillary lymph nodes by diffusion-weighted MRI using ultrasmall superparamagnetic iron oxide in patients with breast cancer: Initial clinical experience. *Journal of Magnetic Resonance Imaging* 2011; 34(3): 557-562.
188. Kwee TC, Takahara T, Luijten PR, Nievelstein RAJ. ADC measurements of lymph nodes: Inter- and intra-observer reproducibility study and an overview of the literature. *European Journal of Radiology* 2010; 75(2): 215-220.
189. Yu X-p, Wen L, Hou J, Bi F, Hu P, Wang H, Wang W. Discrimination between metastatic and nonmetastatic mesorectal lymph nodes in rectal cancer using intravoxel incoherent motion diffusion-weighted magnetic resonance imaging. *Academic radiology* 2016; 23(4): 479-485.
190. Qiu L, Liu XL, Liu SR, Weng ZP, Chen XQ, Feng YZ, Cai XR, Guo CY. Role of quantitative intravoxel incoherent motion parameters in the preoperative diagnosis of nodal metastasis in patients with rectal carcinoma. *Journal of Magnetic Resonance Imaging* 2016; 44(4): 1031-1039.
191. Hauser T, Essig M, Jensen A, Laun FB, Münter M, Maier-Hein KH, Stieltjes B. Prediction of treatment response in head and neck carcinomas using IVIM-DWI: Evaluation of lymph node metastasis. *European journal of radiology* 2014; 83(5): 783-787.
192. Bourne R, Bongers A, Charles N, Power C, Sved P, Watson G. Effect of formalin fixation on biexponential modeling of diffusion decay in prostate tissue. *Magnetic Resonance in Medicine* 2013; 70(4): 1160-1166.
193. Basser PJ. Inferring microstructural features and the physiological state of tissues from diffusion-weighted images. *NMR in Biomedicine* 1995; 8(7): 333-344.
194. Cook PA, Bai S, Nedjati-Gilani S, Seunarine KK, Hall MG, Parker GJ, Alexander DA. Camino: Open-Source Diffusion-MRI Reconstruction and Processing.

- Proceedings of the 14th Annual Meeting ISMRM. Seattle, WA, USA; 2006. p 2759.
195. Weingärtner H. Self diffusion in liquid water. A reassessment. *Zeitschrift für Physikalische Chemie* 1982; 132(2): 129-149.
 196. Burnham KP, Anderson DR. Model selection and inference. A practical information theoretical approach.: Springer-Verlag, New York; 1998.
 197. Holz M, Heil SR, Sacco A. Temperature-dependent self-diffusion coefficients of water and six selected molecular liquids for calibration in accurate ¹H NMR PFG measurements. *Physical Chemistry Chemical Physics* 2000; 2(20): 4740-4742.
 198. Richardson S, Siow B, Panagiotaki E, Schneider T, Lythgoe MF, Alexander DC. Viable and fixed white matter: Diffusion magnetic resonance comparisons and contrasts at physiological temperature. *Magnetic Resonance in Medicine* 2014; 72(4): 1151-1161.
 199. Storas T, Bongers A, Power C, Bourne R. Effect of Formalin Fixation on Biexponential Modeling of T1 and T2 Decay in Prostate Tissue. *Proceedings of the 21st Annual Meeting ISMRM. Salt Lake City, UT, USA: International Society for Magnetic Resonance in Medicine; 2013. p 1792.*
 200. Storas TH, Gjesdal KI, Gadmar OB, Geitung JT, Klow NE. Prostate Magnetic Resonance Imaging: Multiexponential T2 Decay in Prostate Tissue. *Journal of Magnetic Resonance Imaging* 2008; 28(5): 1166-1172.
 201. Li H, Jiang X, Xie J, McIntyre JO, Gore JC, Xu J. Time-dependent influence of cell membrane permeability on MR diffusion measurements: Effect of Permeability on Diffusion MR. *Magnetic Resonance in Medicine* 2015; 75(5): 1927-1934.
 202. Kärger J. Principles and applications of self-diffusion measurements by nuclear magnetic resonance. *Adv Magn Reson* 1988; 12: 1-89.
 203. Bourne R, Kurniawan N, Cowin G, Chowdhury S, Sved P, Watson G, Stait-Gardner T, Price W. Biexponential Diffusion Decay in Formalin Fixed Prostate

- Tissue: Preliminary Findings. *Magnetic Resonance in Medicine* 2012; 68(3): 954-959.
204. Tanner JE. Restricted Self-Diffusion of Protons in Colloidal Systems by the Pulsed-Gradient, Spin-Echo Method. *The Journal of Chemical Physics* 1968; 49(4): 1768-1777.
205. Li L, Margolis DJA, Deng M, Cai J, Yuan L, Feng Z, Min X, Hu Z, Hu D, Liu J, Wang L. Correlation of gleason scores with magnetic resonance diffusion tensor imaging in peripheral zone prostate cancer. *Journal of Magnetic Resonance Imaging* 2015; 42(2): 460-467.
206. Nezzo M, Di Trani MG, Caporale A, Miano R, Mauriello A, Bove P, Capuani S, Manenti G. Mean diffusivity discriminates between prostate cancer with grade group 1&2 and grade groups equal to or greater than 3. *European Journal of Radiology* 2016; 85(10): 1794-1801.
207. Carlo P, Peter J B. Toward a quantitative assessment of diffusion anisotropy. *Magnetic Resonance in Medicine* 1996; 36(6): 893-906.
208. Bastin ME, Armitage PA, Marshall I. A theoretical study of the effect of experimental noise on the measurement of anisotropy in diffusion imaging. *Magnetic Resonance Imaging* 1998; 16(7): 773-785.
209. Sinha S, Sinha U. In vivo diffusion tensor imaging of the human prostate. *Magnetic Resonance in Medicine* 2004; 52(3): 530-537.
210. Rubesova E, Grell AS, De Maertelaer V, Metens T, Chao SL, Lemort M. Quantitative diffusion imaging in breast cancer: a clinical prospective study. *Journal of magnetic resonance imaging* 2006; 24(2): 319-324.
211. Sinha S, Lucas-Quesada FA, Sinha U, DeBruhl N, Bassett LW. In vivo diffusion-weighted MRI of the breast: Potential for lesion characterization. *Journal of magnetic resonance imaging* 2002; 15(6): 693-704.
212. Cukierman E, Pankov R, Stevens DR, Yamada KM. Taking Cell-Matrix Adhesions to the Third Dimension. *Science* 2001; 294(5547): 1708-1712.

213. Sadowska A, Krętowski R, Szynaka B, Cechowska-Pasko M, Car H. Metronidazole decreases viability of DLD-1 colorectal cancer cell line. *Cancer Biotherapy and Radiopharmaceuticals* 2013; 28(8): 615-622.
214. Malmborg C, Sjöbeck M, Brockstedt S, Englund E, Söderman O, Topgaard D. Mapping the intracellular fraction of water by varying the gradient pulse length in q-space diffusion MRI. *Journal of Magnetic Resonance* 2006; 180(2): 280-285.
215. Thelwall PE, Shepherd TM, Stanisz GJ, Blackband SJ. Effects of temperature and aldehyde fixation on tissue water diffusion properties, studied in an erythrocyte ghost tissue model. *Magnetic Resonance in Medicine* 2006; 56(2): 282-289.
216. Liang S, Panagiotaki E, Bongers A, Shi P, Sved P, Watson G, Bourne R. Information-based ranking of 10 compartment models of diffusion-weighted signal attenuation in fixed prostate tissue. *NMR in Biomedicine* 2016; 29(5): 660-671.

Appendices

Appendix A Supporting Information for Chapter 3

Table A.1 P-values from Mann-Whitney U-test.

Insignificant differences ($P > 0.05$) between models are shown in bold type. 1 – Ball, 2 – Bi-ball, 3 – Ball-zeppelin, 4 – Bi-ball-zeppelin, 5 – Zeppelin-sphere, 6 – Bi-zeppelin, 7 – Tensor-sphere, 8 – Ball-sphere, 9 – Ball-tensor, 10 – DTI, 11 – Ball-stick-sphere

Prostate 1

	2	3	4	5	6	7	8	9	10	11
1	4×10^{-21}	2×10^{-45}	6×10^{-46}	2×10^{-75}	8×10^{-46}	3×10^{-74}	2×10^{-49}	7×10^{-45}	5×10^{-16}	2×10^{-75}
2		6×10^{-12}	3×10^{-13}	2×10^{-56}	5×10^{-13}	1×10^{-55}	2×10^{-13}	1×10^{-11}	7×10^{-8}	2×10^{-60}
3			0.48	2×10^{-33}	0.54	1×10^{-32}	0.78	0.89	4×10^{-33}	2×10^{-41}
4				6×10^{-29}	0.89	3×10^{-28}	0.7	0.39	7×10^{-34}	3×10^{-37}
5					2×10^{-29}	0.9	3×10^{-33}	7×10^{-34}	3×10^{-70}	3×10^{-4}
6						6×10^{-29}	0.78	0.45	9×10^{-34}	5×10^{-38}
7							1×10^{-32}	3×10^{-33}	1×10^{-68}	2×10^{-4}
8								0.68	2×10^{-35}	5×10^{-41}
9									1×10^{-32}	7×10^{-42}
10										9×10^{-71}

Prostate 2

	2	3	4	5	6	7	8	9	10	11
1	0.01	3×10^{-11}	2×10^{-11}	2×10^{-35}	1×10^{-5}	2×10^{-19}	7×10^{-17}	3×10^{-11}	0.38	8×10^{-18}
2		9×10^{-5}	7×10^{-5}	1×10^{-23}	0.06	5×10^{-10}	3×10^{-8}	9×10^{-5}	4×10^{-4}	3×10^{-9}
3			0.95	2×10^{-11}	0.06	0.02	0.11	0.93	4×10^{-14}	0.03
4				3×10^{-11}	0.05	0.02	0.13	0.89	3×10^{-14}	0.03
5					8×10^{-16}	3×10^{-6}	7×10^{-8}	1×10^{-11}	1×10^{-39}	4×10^{-6}
6						4×10^{-5}	7×10^{-4}	0.07	1×10^{-7}	1×10^{-4}
7							0.41	0.01	2×10^{-23}	0.9
8								0.1	1×10^{-20}	0.51
9									4×10^{-14}	0.02
10										1×10^{-21}

Prostate 3

	2	3	4	5	6	7	8	9	10	11
1	1×10^{-87}	1×10^{-95}	5×10^{-97}	4×10^{-112}	7×10^{-97}	1×10^{-111}	1×10^{-107}	1×10^{-95}	1×10^{-4}	2×10^{-112}
2		4×10^{-7}	6×10^{-11}	4×10^{-80}	3×10^{-10}	3×10^{-76}	1×10^{-40}	4×10^{-7}	2×10^{-80}	5×10^{-94}
3			0.99	4×10^{-60}	0.14	1×10^{-56}	8×10^{-21}	0.99	2×10^{-89}	3×10^{-78}
4				1×10^{-48}	0.71	1×10^{-45}	8×10^{-14}	0.08	2×10^{-91}	1×10^{-68}
5					3×10^{-51}	0.69	5×10^{-22}	5×10^{-60}	3×10^{-111}	2×10^{-18}
6						5×10^{-48}	4×10^{-15}	0.15	4×10^{-91}	2×10^{-71}
7							4×10^{-20}	1×10^{-56}	1×10^{-110}	2×10^{-19}
8								9×10^{-21}	4×10^{-104}	2×10^{-54}
9									2×10^{-89}	2×10^{-78}
10										5×10^{-112}

Prostate 4

	2	3	4	5	6	7	8	9	10	11
1	4×10^{-22}	4×10^{-23}	3×10^{-23}	6×10^{-40}	4×10^{-23}	4×10^{-39}	1×10^{-39}	4×10^{-23}	0.21	2×10^{-39}
2		0.55	0.47	3×10^{-17}	0.51	3×10^{-15}	5×10^{-15}	0.59	2×10^{-20}	2×10^{-20}
3			0.85	2×10^{-15}	0.92	1×10^{-13}	3×10^{-13}	0.99	1×10^{-21}	9×10^{-19}
4				1×10^{-14}	0.91	5×10^{-13}	1×10^{-12}	0.82	1×10^{-21}	5×10^{-18}
5					4×10^{-15}	0.52	0.25	1×10^{-15}	2×10^{-39}	0.01
6						2×10^{-13}	6×10^{-13}	0.9	1×10^{-21}	2×10^{-18}
7							0.63	7×10^{-14}	2×10^{-38}	0.003
8								2×10^{-13}	5×10^{-39}	7×10^{-4}
9									1×10^{-21}	7×10^{-19}
10										1×10^{-38}

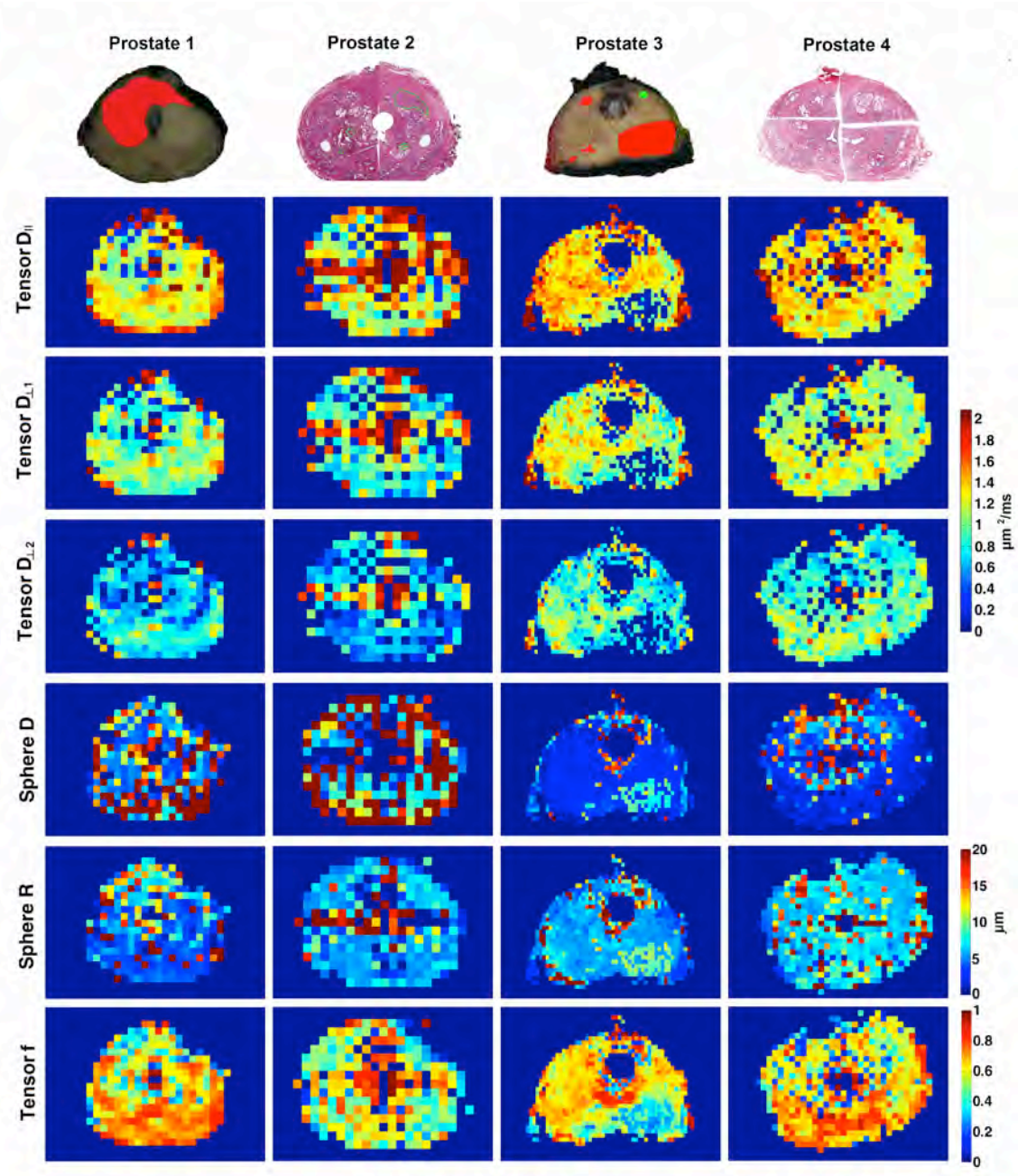


Figure A.1 Tensor-sphere model parameter maps.

Slice positions as for Fig. 3.1.

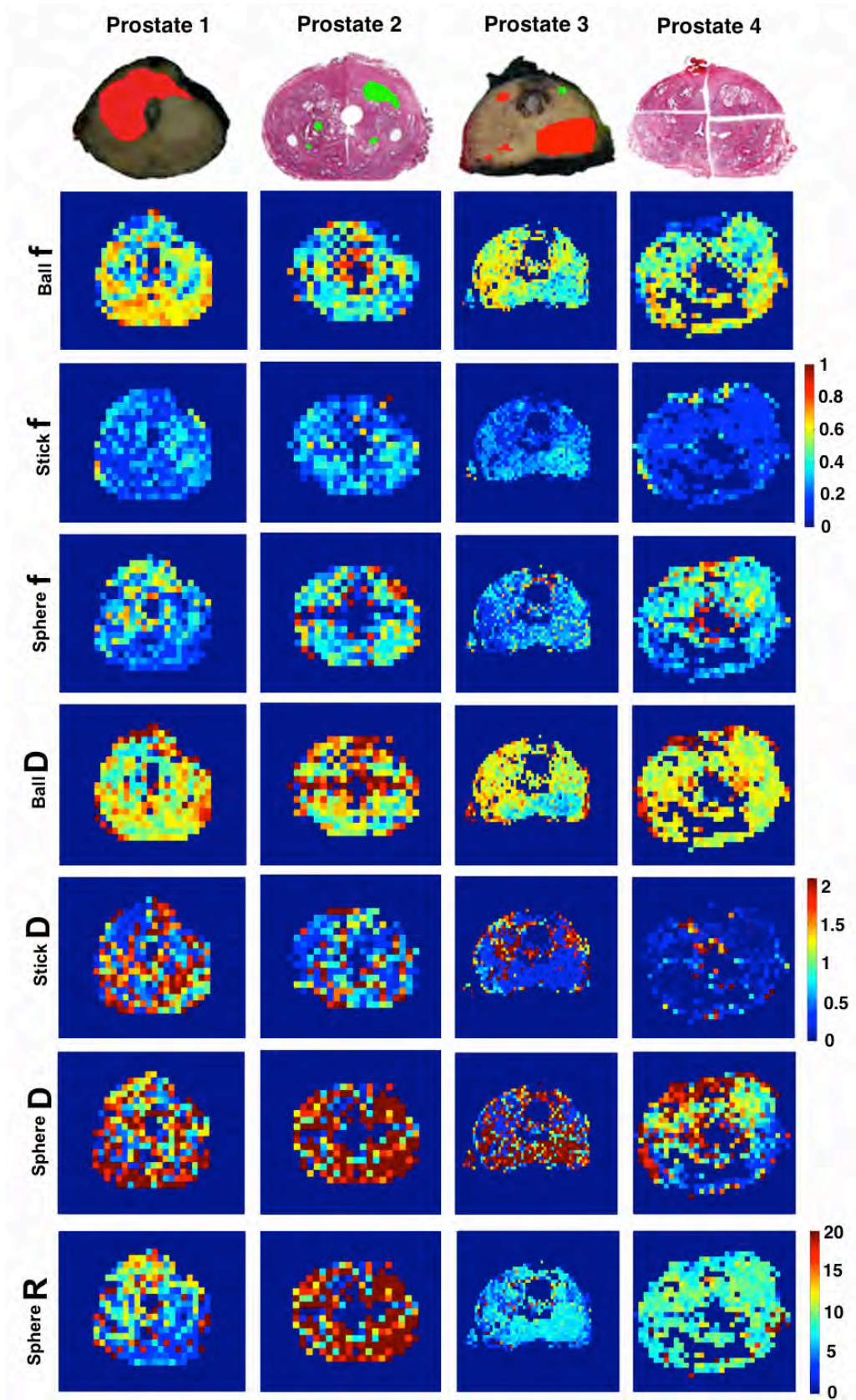


Figure A.2 Ball-stick-sphere model parameter maps.

Slice positions as for Fig. 3.1.

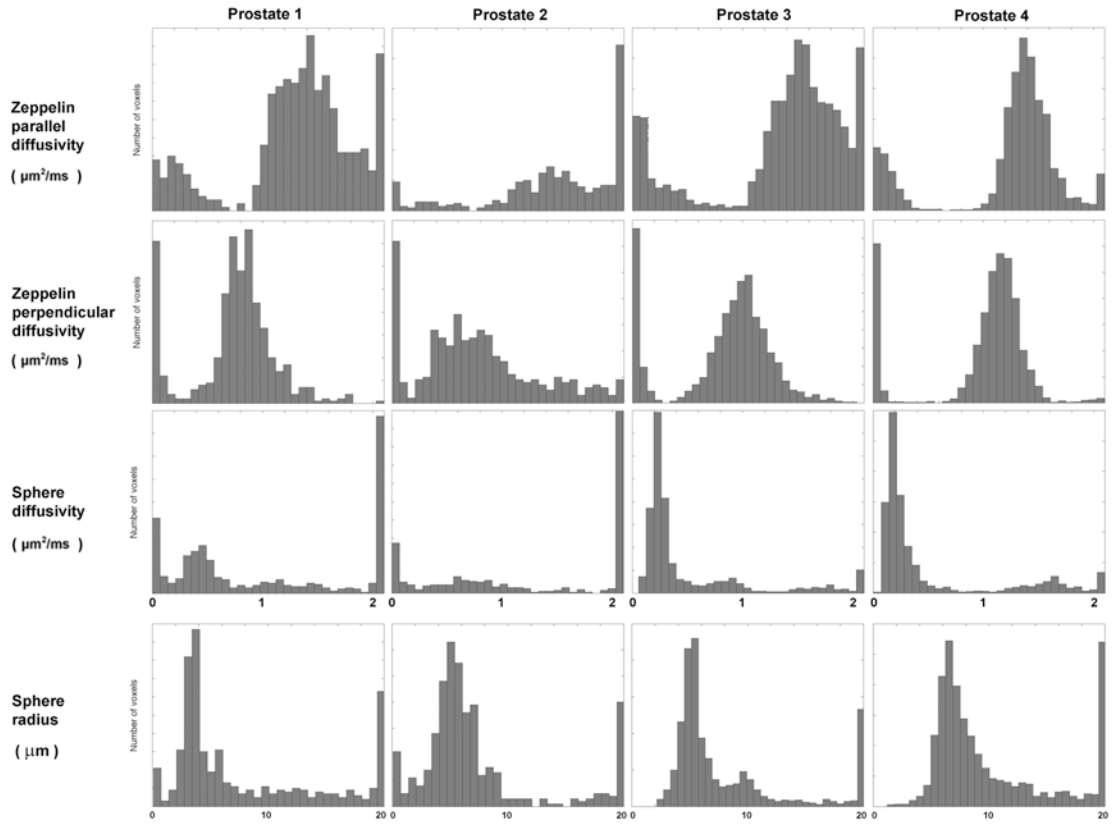


Figure A.3 One-way parameter histograms fro Zeppelin-sphere model

Appendix B Supporting Information for Chapter 4

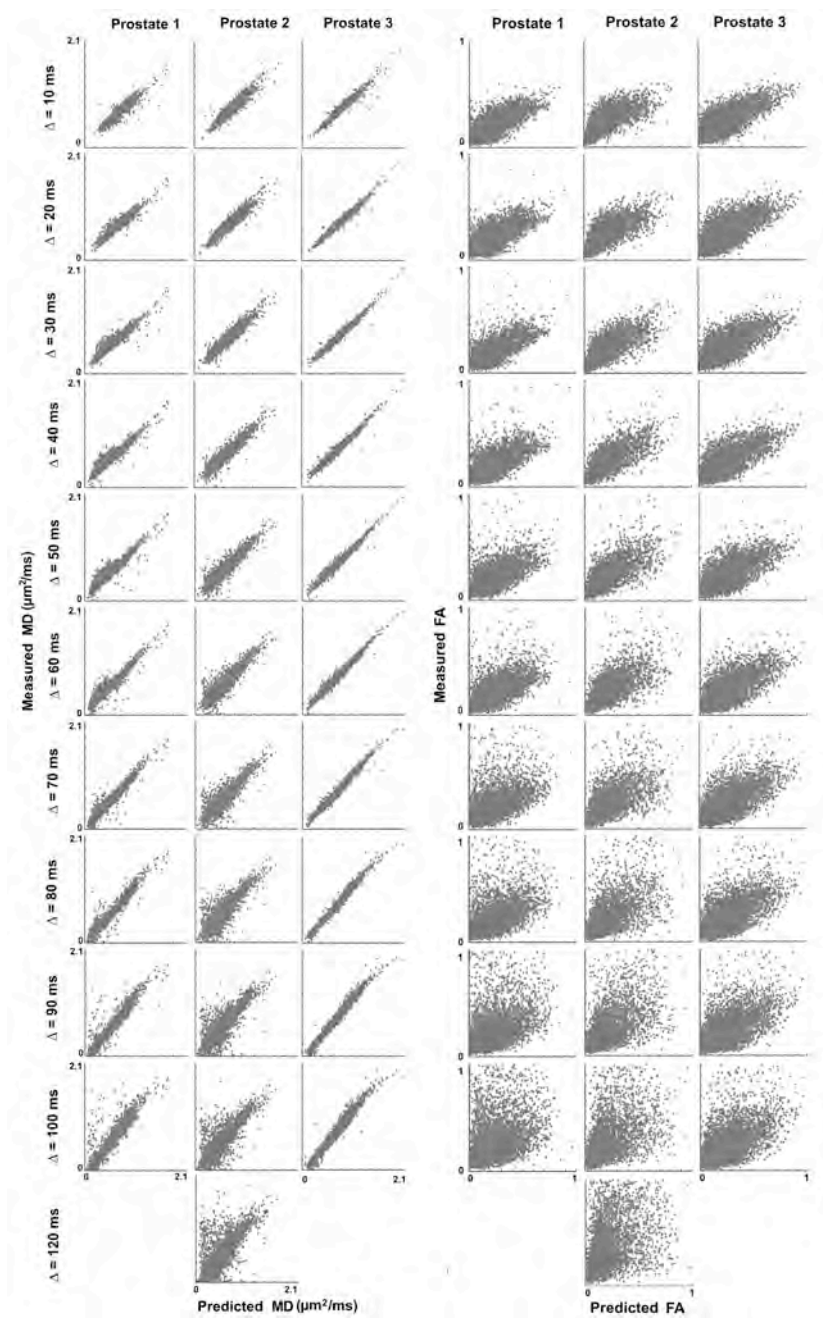


Figure B.1 Scatter plots of measured MD and FA versus MD and FA predicted by the zeppelin-sphere model for $b = 1600 \text{ s/mm}^2$.

Data are from 3957 voxels in Prostate 1, 3510 voxels in Prostate 2, and 4680 voxels in Prostate 3

Appendix C Supporting Information for Chapter 5

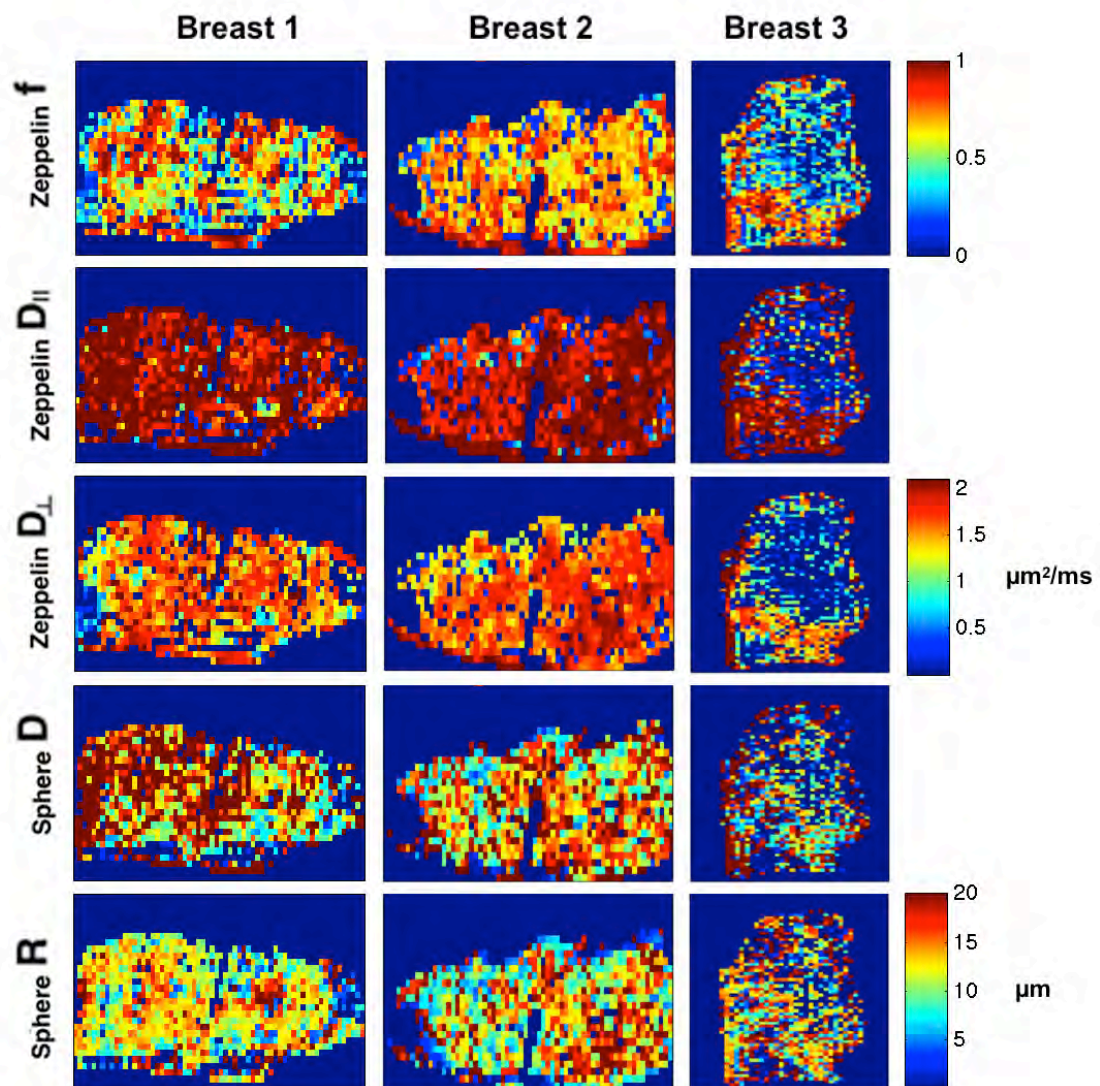


Figure C.1 Zeppelin-sphere model parameter maps.

Slice positions as for Fig 5.1.